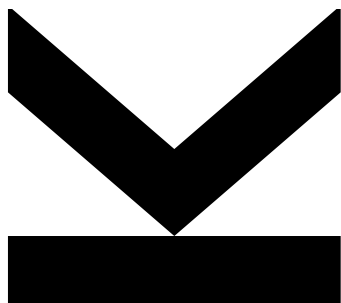


# **Comparison of different evaluation strategies for single-molecule force spectroscopy of antibody/antigen interactions**



Master Thesis  
to obtain the academic degree of  
Diplom-Ingenieurin  
in the Master's Program  
Biophysik

Submitted by  
**Sabrina Meindlhumer,**  
**B.Sc.**

Submitted at  
**Institute of Biophysics**

Supervisor  
**Assoc. Univ. Prof. Dr.**  
**Andreas Ebner**

September 2019



---

## **Eidesstattliche Erklärung**

Ich erkläre an Eides statt, dass ich die vorliegende Masterarbeit selbstständig und ohne fremde Hilfe verfasst, andere als die angegebenen Quellen und Hilfsmittel nicht benutzt bzw. die wörtlich oder sinngemäß entnommenen Stellen als solche kenntlich gemacht habe. Die vorliegende Masterarbeit ist mit dem elektronisch übermittelten Textdokument identisch.

---

Datum

---

Unterschrift



# Acknowledgement

An incomplete list of all the people towards which I would like to express my gratitude:<sup>1</sup>

First of all, I wish to thank my supervisor Andreas Ebner for giving me the chance to work on this master's thesis and for all of his support and encouragement.

I would also like to thank Johannes Preiner as well as his colleagues Andreas Karner and Jürgen Strasser from Fachhochschule Oberösterreich, who guided me in performing my data analysis and were always ready to answer my numerous questions.

Next, I would like to thank Joanna Niedziółka-Jönsson and Marta Janczuk-Richter from the Institute of Physical Chemistry of the Polish Academy of Sciences in Warsaw, who provided us with the sample and always showed a keen interest in our results.

Further, I wish to thank the whole Applied Experimental Biophysics group, which offered a lot of support throughout my master's project and made me feel welcome from the very first day on.

Here, I would particularly like to mention Hanna Seferovic, but also Begüm Dikecoglu and Sarah Stainer, from whom I always received help and useful input.

Equally, thank goes to Philipp Vogl, who could only be here for too short a time, but who was always supportive and kindly helped me in the chemistry lab.

Also, I thank my co-master-student Sarah Rautnig for letting me use her data to test out my program (and her moral support, as we were sitting in the same boat).

Last but not least, my thanks goes to my family and of course Julian for more reasons than I could ever possibly list.

---

<sup>1</sup>This document is set in Palatino, compiled with pdflatex2e and Biber.

The L<sup>A</sup>T<sub>E</sub>X template from Karl Voit is based on KOMA script and can be found online:  
<https://github.com/novoid/LaTeX-KOMA-template>



# Zusammenfassung

Ziel dieser Masterarbeit war es, ein Framework zu entwickeln, das die bisher etablierten Methoden zur Datenauswertung in der dynamischen Kraftspektroskopie (DFS) ergänzt. Um einen Datensatz zur Verfügung zu haben, an dem dieses Framework getestet werden kann, wurde eine Interaktionsstudie an C-aktivem Protein (CRP) und einem monoklonalem Antikörper (anti-CRP) mithilfe eines Atomkraftmikroskops (AFM) durchgeführt.

Die gesammelten Abrisskräfte wurden hinsichtlich ihrer Abhängigkeit von der *loading rate* mittels diverser Methoden und theoretischer Modelle analysiert, insbesondere der Modelle von Friddle und Bell-Evans. Das Ziel dieser Analyse ist, charakteristische Parameter der Interaktion zu ermitteln, wie die kinetische Dissoziationsrate  $k_{off}$ .

Der wichtigste Ansatz basierte auf dem Binnen der Daten in eine gewisse Anzahl an Bins pro Zehnerpotenz im Bezug auf die *loading rate*. Dies erlaubt eine Analyse der Kraft-Verteilungsfunktionen, errechnet für die Datenpunkte in den jeweiligen Bins. Diese Kraft-Verteilungsfunktionen ermöglichen es, individuelle Populationen innerhalb der Daten zu identifizieren, welche dann von multiplen Bindungen oder anderen Interaktionstypen stammen können. Zu diesem Zweck wurden die binweisen Kraft-Verteilungen mit Gauß-Funktionen gefittet, wobei jede Gauß-Funktion als eine Population interpretiert wurde.

Die vollständige Analyse umfasst Least-Squares-Fits der ursprünglichen Daten, der mittleren Kräfte berechnet für die gebinnten Daten und der mittleren Kräfte, die man aus den isolierten Populationen erhalten hat.

Die Methodik wurde in einem MATLAB-basierten Framework implementiert, mit dem zukünftig ähnliche Analysen vorgenommen werden können. Das Framework wurde auch an den Daten eines anderen Systems (mesenchymale Stammzellen und ein spezifischer Antikörper) getestet.



# Abstract

The goal of this master's thesis was to develop a framework that would complement formerly established methods in dynamic force spectroscopy (DFS) data evaluation. To have a dataset on which this evaluation framework could be put to the test, an interaction study on C-reactive protein (CRP) and a monoclonal antibody (anti-CRP) was performed using an atomic force microscope (AFM).

The collected unbinding force data were analyzed with respect to their dependence on the loading rate with a few methods and theoretical models, most prominently Friddle and Bell-Evans model. The goal of this analysis is to extract characteristic parameters of the interaction, like the kinetic off-rate  $k_{off}$ .

The most important approach was based on binning of the data into a certain number of bins per logarithmic decade with respect to the loading rate. Doing so allows to perform an analysis of the force distribution functions calculated for the datapoints in the respective bins. These force distributions make it possible to identify individual populations within the data, which may correspond to multi-bonds or other types of interactions occurring within the system. For this purpose, Gaussian functions were fitted onto the bin-wise force distributions and interpreted as representing one population each. The whole analysis comprises least-squares fitting of the original data, of the mean forces calculated for the bins and of the mean forces obtained for the isolated populations.

This method was implemented in a MATLAB-based framework that allows to perform similar analyses on other systems in the future. The framework was also tested on data recorded on another biological system (mesenchymal stem cells and a specific monoclonal antibody).



# Contents

## Zusammenfassung

## Abstract

<b>1. Introduction</b>	<b>1</b>
1.1. Motivation . . . . .	1
1.2. Atomic Force Microscopy . . . . .	2
1.2.1. Overview . . . . .	2
1.2.2. Force measurement . . . . .	2
1.2.3. Scanning modes . . . . .	4
1.3. AFM-based single-molecule force spectroscopy . . . . .	5
1.3.1. Basics of single-molecule force spectroscopy . . . . .	5
1.3.2. Cantilever tip functionalization . . . . .	5
1.3.3. Force-distance cycle . . . . .	7
1.3.4. Worm-like chain model and effective spring constant . . . . .	8
1.3.5. Unbinding force distributions . . . . .	10
1.3.6. Spring constant determination . . . . .	10
1.3.7. Energy surface of a receptor-ligand interaction . . . . .	12
1.3.8. Dynamic force spectroscopy . . . . .	13
1.4. Models in dynamic force spectroscopy . . . . .	14
1.4.1. Bell-Evans model . . . . .	14
1.4.2. Humer-Szabo model and Dudko model . . . . .	16
1.4.3. Friddle model . . . . .	17
1.4.4. Friddle model for multiple bonds . . . . .	20
1.5. Extracting information from force distributions . . . . .	20
1.6. C-reactive protein . . . . .	21
1.7. Mesenchymal stem cells and RAGE receptors . . . . .	23

<b>2. Materials and Methods</b>	<b>24</b>
2.1. AFM and cantilever specifications . . . . .	24
2.2. Cantilever tip and sample functionalization . . . . .	25
2.2.1. Aminofunctionalization with APTES . . . . .	25
2.2.2. Sample preparation . . . . .	25
2.2.3. Antibody-coupling via acetal-PEG-NHS linker . . . . .	26
2.2.4. MSC and anti-RAGE . . . . .	27
2.3. Experimental approach . . . . .	28
2.3.1. SMFS measurements . . . . .	28
2.3.2. Specificity proof . . . . .	29
2.3.3. Imaging and scratch experiments . . . . .	30
2.3.4. Spring constant determination . . . . .	30
2.4. Data evaluation . . . . .	31
2.4.1. Evaluation of force-distance cycles . . . . .	31
2.4.2. Distribution of curve parameters . . . . .	32
2.4.3. Pulling-rate-grouped and most-likelihood fitting . . . . .	33
2.4.4. Loading-rate binning and population-wise fitting . . . . .	33
2.4.5. Weighting of individual datapoints, bins and populations . . . . .	34
2.4.6. Mean rupture force fitting . . . . .	36
2.4.7. Fitting specifications and quality assessment . . . . .	37
<b>3. Results and Discussion</b>	<b>38</b>
3.1. Imaging and scratch experiments . . . . .	38
3.2. SMFS measurements . . . . .	43
3.2.1. Binding probabilities . . . . .	43
3.2.2. Distributions . . . . .	43
3.2.3. Block experiments . . . . .	44
3.3. CRP and anti-CRP interaction study evaluation . . . . .	48
3.3.1. Collected DFS results . . . . .	48
3.3.2. Grouping by pulling rate . . . . .	48
3.3.3. Maximum-likelihood fit . . . . .	49
3.3.4. Loading rate binning . . . . .	50
3.3.5. Analysis of the higher loading rate regime . . . . .	57
3.3.6. Population analysis . . . . .	58

## Contents

---

3.3.7. Comparison and discussion of evaluation strategies . . . . .	64
3.4. MSC and RAGE-antibody interaction study evaluation . . . . .	66
3.4.1. Collected DFS results . . . . .	66
3.4.2. Loading rate binning . . . . .	66
3.4.3. Population analysis . . . . .	66
3.4.4. Comparison and discussion of evaluation strategies . . . . .	72
3.5. Conclusion and outlook . . . . .	74
<b>A. SMFS results for CRP and anti-CRP</b>	<b>78</b>
<b>B. Bin-wise rupture force distributions for CRP and anti-CRP</b>	<b>84</b>
<b>C. Bin-wise rupture force distributions for MSC and anti-RAGE</b>	<b>88</b>
<b>D. Gaussian functions fitted onto bin-wise force PDFs for MSC and anti-RAGE</b>	<b>92</b>
<b>Bibliography</b>	<b>96</b>



# List of Figures

1.1.	Optical readout-system for cantilever deflection. From Bhushan et al. [2] . . . . .	3
1.2.	Scheme of a protein coupled to an AFM-tip via an acetal-PEG-NHS linker. Wildling et al. (2011). [6]. . . . .	6
1.3.	Methods for aminofunctionalization of silicon / silicon nitride surfaces. From Ebner et al. (2007) [7]. . . . .	7
1.4.	Force-distance cycle in AFM-based SMFS. From Bhushan et al. [2] . . . . .	8
1.5.	Relationship between cantilever deflection $z$ , tip-sample distance $z^*$ and piezo movement $x$ . . . . .	9
1.6.	The influence of force exertion on the energy barrier of a receptor-ligand complex. From Bhushan et al. [2] . . . . .	13
1.7.	Potential profiles and kinetic rates in Friddle's model. From Friddle et al. [16] . . . .	18
1.8.	Numerically calculated rupture force distributions assuming a harmonic probe potential for increasing loading rate. From Friddle et al. (2008) [17] . . . . .	19
1.9.	Crystal structure of CRP [24] . . . . .	22
2.1.	Microscope image of an MSCT chip by BRUKER, cantilevers B C D E F visible, laser focused on cantilever C . . . . .	24
2.2.	Protein coupling to an AFM tip via acetal-PEG-NHS linker. From Wildling et al., Supplementary. (2011). [6] . . . . .	26
2.3.	Information extracted from a force-distance curve . . . . .	32
2.4.	Example for fitting two Gaussians onto a force PDF. . . . .	35
3.1.	Mica in $H_2O$ , imaged in contact mode . . . . .	38
3.2.	APTES-coated mica in PBS, imaged in contact mode . . . . .	39
3.3.	APTES-coated mica, suspended in PBS, scratch experiment, imaged in contact mode .	39
3.4.	APTES-coated mica functionalized with EGS, suspended in PBS, imaged in contact mode	40
3.5.	APTES-coated mica functionalized with EGS, suspended in PBS, imaged in contact mode	40

---

3.6. Mica functionalized with CRP, suspended in PBS, imaged in contact mode . . . . .	41
3.7. Mica functionalized with CRP, scratch experiment, suspended in PBS, imaged in contact mode . . . . .	41
3.8. Height profile of the line highlighted in figure 3.7 . . . . .	42
3.9. Unbinding force distribution, effective spring constant distribution, unbinding length distribution and comparison of unbinding force and unbinding length, acquired for a pulling rate of 0.6 $\mu\text{m}/\text{s}$ and a maximum hold time of 0.3 s, total number of curves: 4965, binding probability: 6.89 % . . . . .	44
3.10. 1 $\mu\text{m}/\text{s}$ comparison of original and block . . . . .	46
3.11. 1 $\mu\text{m}/\text{s}$ comparison of block and recovery . . . . .	46
3.12. 1 $\mu\text{m}/\text{s}$ comparison of original and block . . . . .	47
3.13. Rupture force data recorded for studying the interaction of CRP and anti-CRP. . . . .	48
3.14. Green: DFS data grouped by pulling rate, most-likely force and standard deviations in both coordinates indicated by the ovals. Blue: Bell-Evans fit of most-likely rupture force. Fit results: $x_\beta = (2.91 \pm 0.78) \text{ \AA}$ , $k_{off} = (0.04 \pm 0.08) \text{ s}^{-1}$ . . . . .	49
3.15. Green: DFS data for the interaction study on CRP and anti-CRP. Blue thick solid line: Maximum-likelihood Bell-Evans fit of most-likely rupture force. Fit results: $x_\beta = (0.719 \pm 0.015) \text{ \AA}$ , $k_{off} = (4.36 \pm 0.25) \text{ s}^{-1}$ , BIC=9816.4 . . . . .	50
3.16. Force PDF for 199.53 pN/s (31 datapoints) and 316.23 pN/s (63 datapoints) . . . . .	51
3.17. Force PDF for 501.19 pN/s (64 datapoints) and 794.33 pN/s (72 datapoints) . . . . .	52
3.18. Force PDF for 1258.93 pN/s (103 datapoints) and 1995.26 pN/s (101 datapoints) . . . . .	52
3.19. Force PDF for 3162.28 pN/s (112 datapoints) and 5011.87 pN/s (118 datapoints) . . . . .	52
3.20. Force PDF for 7943.28 pN/s (111 datapoints) and 12 589.25 pN/s (109 datapoints) . . . . .	53
3.21. Force PDF for 19 952.62 pN/s (69 datapoints) and 31 622.78 pN/s (47 datapoints) . . . . .	53
3.22. Force PDF for 50 118.72 pN/s (22 datapoints) . . . . .	53
3.23. Force distribution development for increasing loading rates . . . . .	54
3.24. Binning of the collected data recorded for CRP and anti-CRP into 5 bins per decade with a minimum of 20 datapoints per bin. . . . .	55
3.25. Friddle fit of mean rupture forces calculated for the individual bins shown in figure 3.24. . . . .	56
3.26. Friddle fit for mean rupture forces of CRP and anti-CRP performed for 1038 individual datapoints. . . . .	56
3.27. Bell-Evans fit for mean rupture forces of CRP and anti-CRP performed for 381 individual datapoints for loading rates starting from 6000 pN/s. . . . .	57

## List of Figures

---

3.28. Bell-Evans fit of mean rupture forces calculated for the individual bins shown in figure 3.24 for loading rates starting from 6000 pN/s. . . . .	58
3.29. Force PDFs and fitted Gaussian functions for 199.53 pN/s and 316.23 pN/s . . . . .	59
3.30. Force PDFs and fitted Gaussian functions for 501.19 pN/s and 794.33 pN/s . . . . .	59
3.31. Force PDFs and fitted Gaussian functions for 1258.93 pN/s and 1995.26 pN/s . . . . .	59
3.32. FForce PDFs and fitted Gaussian functions for 3162.28 pN/s and 5011.87 pN/s . . . . .	60
3.33. Force PDFs and fitted Gaussian functions for 7943.28 pN/s and 12 589.25 pN/s . . . . .	60
3.34. Force PDFs and fitted Gaussian functions for 19 952.62 pN/s and 31 622.78 pN/s . . . . .	60
3.35. Force PDFs and fitted Gaussian functions for 50 118.72 pN/s . . . . .	61
3.36. Splitting up of the data collected for CRP and anti-CRP in two populations via fitting with Gaussian functions. . . . .	62
3.37. Friddle fit of first population identified for CRP and anti-CRP via Gaussian fitting. . .	62
3.38. Friddle fit of first population identified for CRP and anti-CRP via Gaussian fitting. . .	63
3.39. Friddle multibond fit of the second population identified for CRP and anti-CRP via Gaussian fitting based on the first population. . . . .	63
3.40. Rupture force data recorded for studying the interaction of MSC and anti-RAGE. . . . .	67
3.41. Friddle fit for mean rupture forces of MSC and anti-RAGE performed for 5977 individual datapoints. . . . .	67
3.42. Binning of the collected data recorded for MSC and anti-RAGE into 5 bins per decade with a minimum of 20 datapoints per bin. . . . .	68
3.43. Friddle fit for mean rupture forces of MSC and anti-RAGE performed for the mean rupture forces calculated for the individual bins shown in figure 3.42. . . . .	68
3.44. Force distribution development of MSC and anti-RAGE for increasing loading rates . .	69
3.45. Splitting up of the data collected for MSC and anti-RAGE in two populations via fitting with Gaussian functions. . . . .	70
3.46. Friddle fit of first population identified for MSC and anti-RAGE via Gaussian fitting. .	70
3.47. Friddle fit of second population identified for MSC and anti-RAGE via Gaussian fitting. .	71
3.48. Friddle fit of second population identified for MSC and anti-RAGE via Gaussian fitting based on the first population. . . . .	71
A.1. Pulling rate 0.04 $\mu\text{m}/\text{s}$ , maximum hold time 0 s . . . . .	79
A.2. Pulling rate 0.08 $\mu\text{m}/\text{s}$ , maximum hold time 0 s . . . . .	79
A.3. Pulling rate 0.2 $\mu\text{m}/\text{s}$ , maximum hold time 0.3 s . . . . .	80
A.4. Pulling rate 0.2 $\mu\text{m}/\text{s}$ , maximum hold time 0.3 s, blocked with 1.33 $\mu\text{g}/\text{ml}$ CRP . . . . .	80

---

A.5. Pulling rate 0.3 $\mu\text{m}/\text{s}$ , maximum hold time 0.3 s . . . . .	81
A.6. Pulling rate 1 $\mu\text{m}/\text{s}$ , maximum hold time 0.3 s . . . . .	81
A.7. Pulling rate 1 $\mu\text{m}/\text{s}$ , maximum hold time 0.3 s, blocked with 1.16 $\mu\text{g}/\text{ml}$ CRP . . . . .	82
A.8. Pulling rate 1 $\mu\text{m}/\text{s}$ , maximum hold time 0.3 s, recovered after blocking with 1.16 $\mu\text{g}/\text{ml}$ CRP . . . . .	82
A.9. Pulling rate 1.2 $\mu\text{m}/\text{s}$ , maximum hold time 0.3 s . . . . .	83
A.10. Pulling rate 2.5 $\mu\text{m}/\text{s}$ , maximum hold time 0.5 s . . . . .	83
B.1. Force PDFs for 199.53 pN/s (31 datapoints) and 316.23 pN/s (63 datapoints) . . . . .	84
B.2. Force PDFs for 501.19 pN/s (64 datapoints) and 794.33 pN/s (72 datapoints) . . . . .	85
B.3. Force PDFs for 1258.93 pN/s (103 datapoints) and 1995.26 pN/s (101 datapoints) . . . . .	85
B.4. Force PDFs for 3162.28 pN/s (112 datapoints) and 5011.87 pN/s (118 datapoints) . . . . .	85
B.5. Force PDFs for 7943.28 pN/s (111 datapoints) and 12 589.25 pN/s (109 datapoints) . . . . .	86
B.6. Force PDFs for 19 952.62 pN/s (69 datapoints) and 31 622.78 pN/s (47 datapoints) . . . . .	86
B.7. Force PDFs for 50 118.72 pN/s (22 datapoints) . . . . .	86
C.1. Force PDFs for 79.43 pN/s (22 datapoints) and 125.89 pN/s (23 datapoints) . . . . .	88
C.2. Force PDFs for 199.53 pN/s (56 datapoints) and 316.23 pN/s (94 datapoints) . . . . .	89
C.3. Force PDFs for 501.19 pN/s (165 datapoints) and 794.33 pN/s (251 datapoints) . . . . .	89
C.4. Force PDFs for 1258.93 pN/s (419 datapoints) and 1995.26 pN/s (633 datapoints) . . . . .	89
C.5. Force PDFs for 3162.28 pN/s (767 datapoints) and 5011.87 pN/s (865 datapoints) . . . . .	90
C.6. Force PDFs for 7943.28 pN/s (939 datapoints) and 12 589.25 pN/s (792 datapoints) . . . . .	90
C.7. Force PDFs for 19 952.62 pN/s (398 datapoints) and 31 622.78 pN/s (279 datapoints) . . . . .	90
C.8. Force PDFs for 50 118.72 pN/s (185 datapoints) and 79 432.82 pN/s (65 datapoints) . . . . .	91
D.1. Force PDFs and fitted Gaussian functions for 79.43 pN/s (22 datapoints) and 125.89 pN/s (23 datapoints) . . . . .	92
D.2. Force PDFs and fitted Gaussian functions for 199.53 pN/s (56 datapoints) and 316.23 pN/s (94 datapoints) . . . . .	93
D.3. Force PDFs and fitted Gaussian functions for 501.19 pN/s (165 datapoints) and 794.33 pN/s (251 datapoints) . . . . .	93
D.4. Force PDFs and fitted Gaussian functions for 1258.93 pN/s (419 datapoints) and 1995.26 pN/s (633 datapoints) . . . . .	93
D.5. Force PDFs and fitted Gaussian functions for 3162.28 pN/s (767 datapoints) and 5011.87 pN/s (865 datapoints) . . . . .	94

## List of Figures

---

D.6. Force PDFs and fitted Gaussian functions for 7943.28 pN/s (939 datapoints) and 12 589.25 pN/s (792 datapoints) . . . . .	94
D.7. Force PDFs and fitted Gaussian functions for 19 952.62 pN/s (398 datapoints) and 31 622.78 pN/s (279 datapoints) . . . . .	94
D.8. Force PDFs and fitted Gaussian functions for 50 118.72 pN/s (185 datapoints) and 79 432.82 pN/s (65 datapoints) . . . . .	95



# **Abbreviations**

- AGE** - advanced glycation end-products  
**AFM** - atomic force microscopy / microscope  
**anti-CRP** - specific antibody for CRP  
**anti-RAGE** - specific antibody for RAGE  
**APTES** - (3-aminopropyl)triethoxysilane  
**CRP** - C-reactive protein  
**DFS** - dynamic force spectroscopy  
**EGS** - ethylene glycol bis(succinimidyl succinate)  
**GUI** - graphic user interface  
**MSC** - mesenchymal stem cells  
**NHS** - N-hydroxysuccinimide  
**PBS** - phosphate buffered saline  
**PDF** - probability density function  
**PEG** - polyethylene glycol  
**RAGE** - receptor for AGE  
**SDS** - sodium dodecyl sulfate  
**SMFS** - single-molecule force spectroscopy  
**SPM** - scanning probe microscopy / microscope  
**STM** - scanning tunneling microscopy / microscope  
**TEA** - triethylamine

# 1. Introduction

## 1.1. Motivation

The goal of this master's thesis was to develop a framework for dynamic force spectroscopy (DFS) data evaluation. This framework should serve as a complement and provide additional information to data evaluation as performed by the methods formerly established at the Institute of Biophysics of Johannes Kepler University.

It was decided to implement a method based upon the binning of unbinding force data with respect to the loading rate. An analysis of the bin-wise rupture force distributions would allow the identification of individual populations occurring within the data collected from a series of DFS experiments.

To have a dataset on which this framework could be put to the test, the interaction between C-reactive protein (CRP) and a commercially available monoclonal antibody was studied by single-molecule force spectroscopy (SMFS). This biological system was chosen as it stands in the center of an ongoing collaboration with the Surface Nanoengineering Group from the Institute of Physical Chemistry of the Polish Academy of Sciences.

Therefore, this was the first of a planned series of measurements within this project that aims to study the interaction of CRP with antibodies and later, with peptides.

Additionally, the evaluation strategy was applied to data of an additional system, mesenchymal stem cells and a monoclonal antibody for RAGE (receptor for advanced glycation end-products), recorded by Sarah Rautnig for her master's thesis (2019).

## 1.2. Atomic Force Microscopy

### 1.2.1. Overview

Atomic force microscopy (AFM) was developed in the 1980s based upon achievements in scanning tunneling microscopy (STM). [1] Like in STM, in AFM a probe is raster-scanned over a sample surface. The probe-sample interaction is monitored by measuring a signal which is processed and then mapped to the probe's position over the sample, yielding topographical information. Both microscopy techniques are categorized as variants of scanning probe microscopy (SPM).

In STM, the measured signal is the tunneling current between the probe's tip and the sample. This means that the sample needs to be electrically conductive, restricting the applicability of the technique. In contrast, AFM relies on the measurement of intermolecular forces (typically smaller than 1 nN) and can therefore be used to investigate insulating samples as well. Further, AFM can be performed in a liquid environment. These features have made AFM an indispensable tool in life sciences, as it allows to study samples under physiological conditions.

Imaging is the most basic application of AFM, but modifications of the tip and the device make it possible to perform a number of techniques. One technique frequently used for biological samples is AFM-based single-molecule force spectroscopy (SMFS). [2]

This section will provide an introduction to the general working principles of an AFM and AFM imaging. Section 1.3 will focus on AFM-based SMFS.

### 1.2.2. Force measurement

AFM relies on the measurement of intermolecular forces. To measure these forces, a sharp tip is attached to a cantilever which acts like a spring with a spring constant  $k$ . As it is brought in proximity to the sample, the acting force  $F$  will lead to a cantilever deflection  $z$  according to Hooke's law

$$F = k \cdot z \tag{1.1}$$

with the deflection  $z$  being the parameter that is accessible via measurement. The optical readout system typically used in commercially AFM setups is illustrated in figure 1.1. A laser beam is directed at the backside of the cantilever, from where it is reflected towards a four-segment photodiode. From the different intensities recorded by the four individual segments, the movement of the cantilever can be determined. The voltage difference between the upper and lower sections corresponds to the

vertical movement  $z$  and can be used to obtain information on the sample topography. In contrast, the difference in signal between the left and right segments is caused by the cantilever's lateral movement and can be used for friction force measurements, providing additional (non-topographic) information on the sample surface. [2]

This deflection readout system based upon processing of the signals given by a split photodiode is called the *optical lever method*. It requires the knowledge of a proportionality constant between the photodiode output voltage  $U$  and the cantilever deflection  $z$ . It holds that

$$z = \frac{U}{sens} \quad (1.2)$$

with  $sens$  denoting the mentioned proportionality constant referred to as sensitivity. The photodiode's sensitivity can be determined by bringing the cantilever in contact with a stiff surface and determining the slope of the voltage output  $U$  in the linear region. In this regime, the cantilever deflection  $z$  equals the traveling distance of the piezoelectric element in a direction normal to the sample. [3]

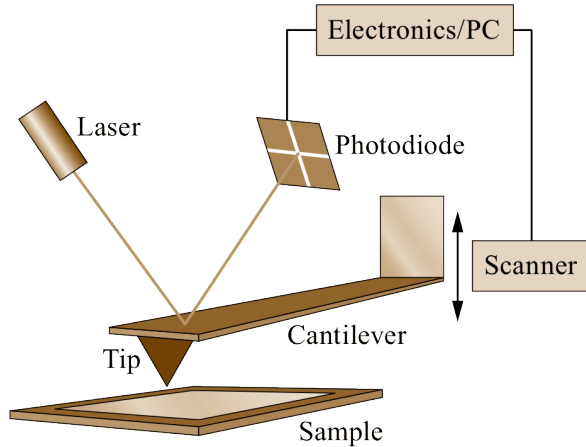


Figure 1.1.: Optical readout-system for cantilever deflection. From Bhushan et al. [2]

The fundamentally limiting factor for the obtainable force resolution  $\Delta F$  is given by the cantilever's thermal noise (with the temperature  $T$  and Boltzmann constant  $k_B$ ) according to

$$\Delta F = (k_B T k)^{1/2} \quad (1.3)$$

and therefore depends on the spring constant. [2] The cantilever's spring constant and dimensions are critical parameters that need to be chosen carefully so as to find a compromise between different requirements. For high accuracy, the goal is to obtain the maximum possible deflection for any given force, which can be achieved by using a soft cantilever (with a small spring constant  $k$ ).

## 1. Introduction

---

However, the resonance frequency  $f_0$  of a spring with an effective mass  $m_0$ , which is given by

$$f_0 = \frac{1}{2\pi} \sqrt{\frac{k}{m_0}} \quad (1.4)$$

should be high enough to make the system insensitive towards the vibrational noise to which it is exposed from its surroundings. Consequently, the ratio  $k/m_0$  needs to be large, which means that for a small  $k$ , the mass  $m_0$  and therefore the dimensions of the cantilever have to be small. [1].

### 1.2.3. Scanning modes

So far, a number of scanning modes have been developed for AFM imaging. For a basic classification, these modes can be grouped into static AFM modes, which use a non-oscillating cantilever, and dynamic AFM modes, where the cantilever is excited to perform oscillations during the scanning process. Further, the various scanning modes differ from each other with regard to the force regime in which they operate and in the way the feedback mechanism is used.

The simplest static imaging mode is contact mode. In this mode, the tip is kept in the contact regime, in which the total interaction force between the tip and the sample is positive. This means that the tip is constantly in contact with the sample. [2], [4]

Contact regime measurements can be performed in constant force mode or in constant height mode. Constant height mode should only be used for very flat and robust samples, as the tip and/or the sample may easily be damaged by the resulting shear forces. The topography is given by the different deflections recorded when raster-scanning the sample.

In constant force mode, the force is controlled as it is held at a constant level by a feedback-loop that aims to maintain constant cantilever deflection. Piezoelectric elements are used to move the cantilever in z-direction with respect to the sample as a response to a change in deflection. Here, the topography is obtained from the distance  $\Delta z$  the piezoelectric element re-positioned the cantilever at any given coordinate. The scanning speed is limited by the reaction of the feedback loop.

For biological samples which are susceptible to damage, soft cantilevers are used to minimize destructive shear forces. However, for fragile samples dynamic imaging modes may be preferable. In intermittent contact or tapping mode, the cantilever is excited to oscillate in a direction normal to the sample surface while scanning. The tip just briefly touches the surface whenever it oscillates towards it. The interaction between tip and sample leads to a change in the oscillation amplitude. The amplitude is used as a feedback-parameter and kept constant by moving the cantilever in z-direction, with the traveling distance yielding topographic information. [2]

For very soft samples, measurements can be performed in non-contact mode with the tip positioned within a regime above the sample in which the interaction is always attractive. Both static and dynamic modes exist for the non-contact regime. [4]

## 1.3. AFM-based single-molecule force spectroscopy

### 1.3.1. Basics of single-molecule force spectroscopy

To understand the binding behavior of a receptor and a ligand, knowledge of the energy landscape underlying the molecules' interaction is required. A number of ensemble techniques are available to study molecular binding. However, if multiple interaction pathways are present, ensemble techniques can only provide an averaged value, not a multilayered analysis of the reactions taking place. Single-molecule techniques are the method of choice when such an analysis is needed, as they yield not only an average, but a distribution of the probed quantity.

SMFS can be performed with any system which has the ability to accurately measure and apply forces along a predefined coordinate. The probability of bond rupture by thermal fluctuations depends on the bond's energy landscape. Applying force to the molecular complex by "pulling" deforms this energy landscape as it lowers the energy barriers in the direction of force exertion. In SMFS, a force is exerted on a molecular complex and a spectrum of rupture forces is recorded. Adequate data evaluation yields a quantitative description of the interaction between the binding partners, providing kinetic rate constants, thermodynamic parameters and energy barriers. [3]

Various experimental setups can be used to perform SMFS. AFM is suitable for this technique as it is based on the detection of ultra-small forces. In AFM-based SMFS, one binding partner is attached to the cantilever tip (in a chemical procedure referred to as tip functionalization) and the other one is attached to a hard surface (such as mica or glass). Using the piezoelectric elements of the AFM device, the tip can be moved relative to the surface, which allows a precise control of the forces exerted on the molecular complex. [2], [3]

### 1.3.2. Cantilever tip functionalization

In AFM-based SMFS, one binding partner is attached to a solid surface, while the other one is tethered to an AFM cantilever tip via a flexible polymer chain, referred to as a linker.

## 1. Introduction

---

Coupling of a protein to the AFM tip via a flexible linker is typically performed in a three-step-process:

1. Generating reactive sites on the cantilever tip surface
2. Attaching one end of the flexible linkers to the reactive sites on the surface
3. Coupling of the molecule-of-interest to the remaining free end of the linker

A number of different protocols exist for either of the three steps. Figure 1.2 illustrates the coupling of a protein (an antibody) to an AFM tip. [5], [6]

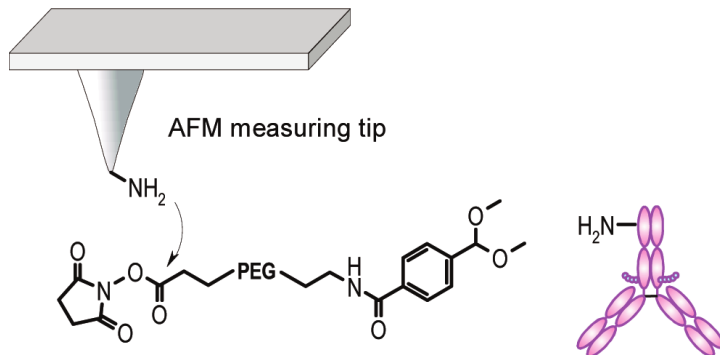


Figure 1.2.: Scheme of a protein coupled to an AFM-tip via an acetal-PEG-NHS linker. Wildling et al. (2011). [6].

AFM cantilevers are typically made of silicon or silicon nitride and as such carry silanol groups (Si-OH) on their surface. These silanol groups can be used to attach molecules carrying free amino-groups (NH<sub>2</sub>), which later serve as a base for coupling of the linker.

Figure 1.3 shows three common methods used for aminofunctionalization of AFM tips. Two of them, ethanolamine- and APhS- based, are performed in liquid phase, while the APTES method relies on a gas phase reaction. Detailed descriptions of these procedures can be found in the literature. [7], [8]

The usage of a flexible crosslinker in SMFS has several advantages. For once, the behavior of the linker upon stretching helps to distinguish molecular recognition from unspecific adhesion because it leads to a characteristic parabolic rupture curve (as will be discussed in section 1.3.3). Further, the protein coupled to the linker can move and rotate (almost) freely within a volume determined by the length of the linker and therefore has the possibility to find a binding partner within this volume.

The linker typically comprises a linear polyethylene glycol (PEG) chain with two molecular groups attached to the ends for reactivity, one designed to attach to the amino-group on the surface and the other one to the molecule via a specific residue. To avoid loop formation, heterobifunctional linkers carrying different coupling groups are preferable.

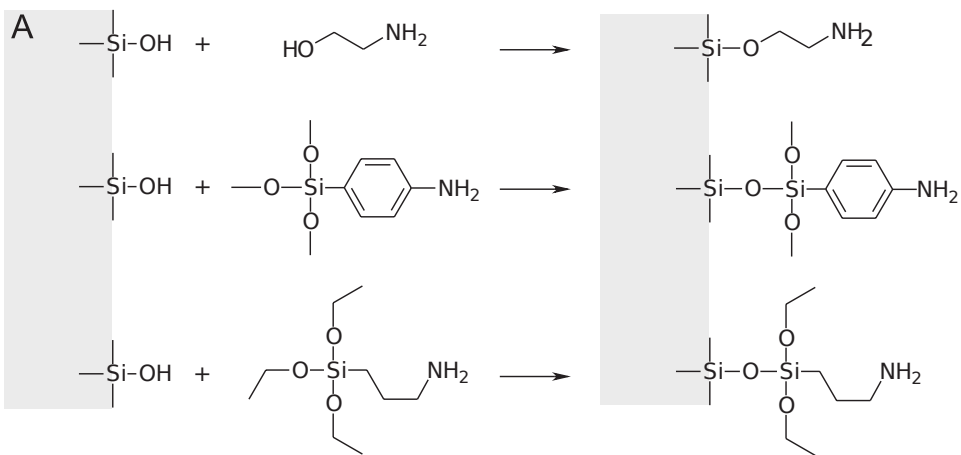


Figure 1.3.: Methods for aminofunctionalization of silicon / silicon nitride surfaces. From Ebner et al. (2007) [7].

The choice of the end groups depends on the kind of residue by which the molecule-of-interest is supposed to be coupled to the linker. For an antibody, coupling is usually performed on a free NH<sub>2</sub>-group from a lysine residue.

An established method uses an aldehyde-PEG-NHS linker (NHS denoting N-Hydroxysuccinimide), with the NHS-ester coupling to the NH<sub>2</sub>-groups on the tip surface. The aldehyde-group can then bind to an NH<sub>2</sub>-group on the antibody. To avoid binding of the aldehyde groups to remaining NH<sub>2</sub>-groups on the surface, the concentration of linkers has to be chosen high enough to reach saturation of these groups. The faster kinetics of NHS-NH<sub>2</sub> compared to aldehyde-NH<sub>2</sub>-group will then avoid loop formation.

Alternatively, acetal-PEG-NHS linkers can be used. The procedure is very similar to the one for aldehyde-PEG-NHS linkers, with an additional step inbetween during which the acetal-group is converted into a reactive aldehyde-group by submerging the tip in citric acid. Acetal-PEG-NHS linkers have several advantages, as lower concentrations of the crosslinker are required and the synthesis is simpler. [5], [6]

### 1.3.3. Force-distance cycle

Figure 1.4 shows an ideal force-distance cycle obtained in AFM-based force spectroscopy experiments. The graph's x-axis shows the distance of the cantilever over the sample, the y-axis shows the force that is calculated from the measured deflection. Over one cycle, the cantilever approaches and is retracted from the surface at a constant speed. As the cantilever approaches the surface but is not yet in contact with it, the detected force is constant in average with noise arising from the cantilever's

## 1. Introduction

---

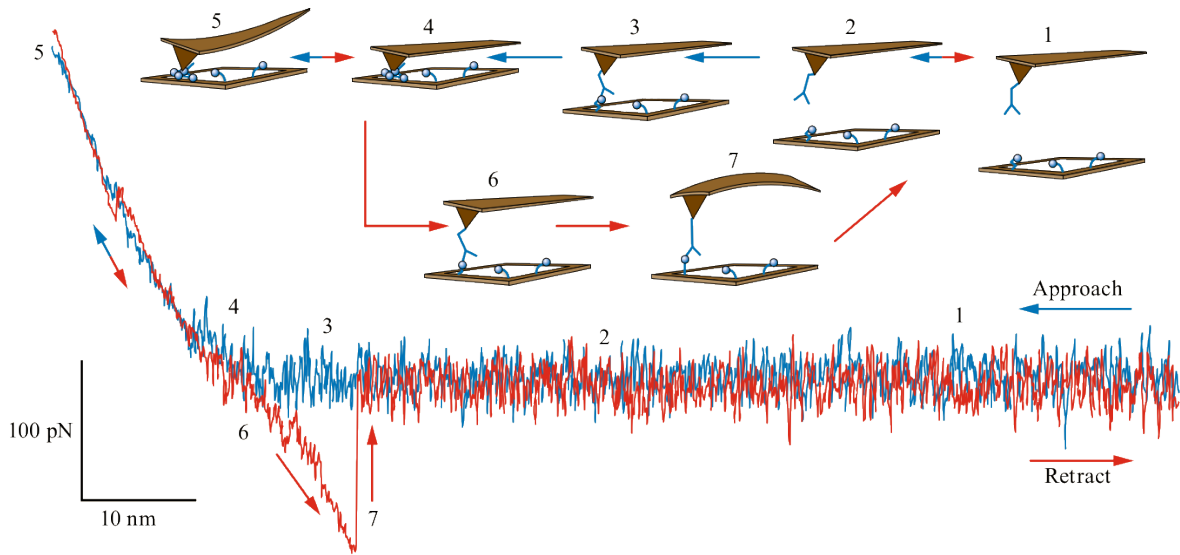


Figure 1.4.: Force-distance cycle in AFM-based SMFS. From Bhushan et al. [2]

thermal motion (1-3). After the cantilever tip reaches the surface (4), a slope can be observed in the force curve while the cantilever bends according to Hook's law (see equation 1.1).

As soon as a predefined maximum force is reached (5), the cantilever is retracted from the surface at the same speed and the contact is lost (6). If no binding event has occurred, the approach- and retract-curve will have the same shape. If a binding event has occurred, a characteristic parabolic curve can be seen as the flexible linker stretches until the rupture takes place (7). The cantilever rapidly snaps upwards, as indicated by the force going back to the baseline level. As the cantilever is retracted further, the mean force stays constant again. [2]

The parabolic curve shape resulting from the stretching of the flexible linker (as explained in section 1.3.4) helps to distinguish specific interactions from unspecific adhesion of the tip to the surface. If adhesion occurs, the cantilever sticks to the surface and bends downwards in a linear fashion as it is retracted, resulting in a linear curve shape extending over the initial contact point (4). [3]

### 1.3.4. Worm-like chain model and effective spring constant

The worm-like chain (WLC) model is frequently used in SMFS to describe the behaviour of a flexible PEG-linker upon stretching. An exact analytical treatment of the WLC model is quite complex. However, at the force scale of typical SMFS experiments, the following approximation is usually

sufficient:

$$F_{WLC}(z^*) = \frac{k_b T}{L_p} \left[ \frac{1}{4(1-z^*/L_0)^2} - \frac{1}{4} + \frac{z^*}{L_0} \right] \quad (1.5)$$

Here,  $L_p$  denotes the persistence length and  $L_0$  the contour length, two parameters describing the properties of the polymer chain. The stretching of the polymer chain by a length  $z^*$  requires a force  $F_{WLC}(z^*)$  as described in equation (1.5). [9]

When a binding event has occurred, the stretching of the linker  $z^*$  equals the distance between tip and sample. The tip-sample distance  $z^*$  depends on the cantilever deflection  $z = F/k$  and the movement  $x$  of the piezoelectric elements in the scanner according to:

$$z^* = x - \frac{F}{k} \quad (1.6)$$

Note that the cantilever deflection  $z = F(x)/k$  is the quantity that is measured by the optical lever method. The relationship between  $x$ ,  $z$  and  $z^*$  is depicted schematically in figure 1.5.

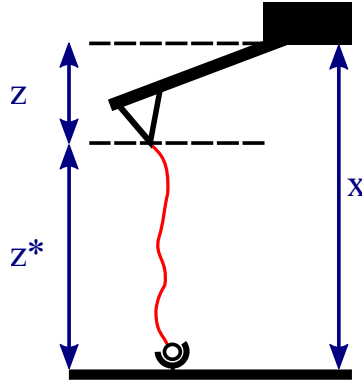


Figure 1.5.: Relationship between cantilever deflection  $z$ , tip-sample distance  $z^*$  and piezo movement  $x$ .

A spring constant  $k_{WLC}$  can be defined for the flexible linker as:

$$k_{WLC}(z^*) = \frac{dF_{WLC}(z^*)}{dz^*} \quad (1.7)$$

It is important to note that this spring constant  $k_{WLC}$  has a non-linear dependence on the linker extension  $z^*$ , leading to the distinct shape of a rupture curve as seen in a force-distance cycle during which an unbinding event has occurred.

For a system comprising a cantilever (behaving like a Hookean spring) and an attached flexible PEG linker in series, the effective spring constant  $k_{eff}$  can be calculated from the following relationship:

$$\frac{1}{k_{eff}} = \frac{1}{k} + \frac{1}{k_{WLC}(z^*)} \quad (1.8)$$

In a force-distance curve, the effective spring constant  $k_{eff}$  at the moment of bond rupture is extracted from the slope immediately before the unbinding. [10]

### 1.3.5. Unbinding force distributions

In a typical SMFS experiment, about 1000 force-distance cycles are recorded for one pulling rate, allowing a statistical evaluation of the acquired data. The number of bindings divided by the total number of cycles recorded gives the *binding probability* of the interaction.

For every interaction study, a specificity proof experiment has to be performed. For this purpose, either of the two binding partners (the one on the tip or on the surface) is saturated by adding free binding partners to the solution. Doing so should significantly lower the binding probability when repeating the experiment.

The *unbinding forces* are collected from the force differences between the rupture (point (7) in figure 1.3.3) and the baseline. From the distribution of unbinding forces, a histogram or a probability density function (PDF) can be calculated. These allow to extract the most probable unbinding force  $F^*$  for one pulling rate. [2]

The representation of force distributions in a histogram is simple, yet the binning width is arbitrary and jump discontinuities at the boundaries of each bin are unavoidable. The estimation of a PDF is generally a better choice. An estimated probability density  $p(x)$  can be calculated using so-called kernel estimation methods. Based upon

$$p(x) = \frac{1}{nb} \sum_{i=1}^n K\left(\frac{x - x_i}{b}\right) \quad (1.9)$$

with  $x_i$  denoting the measured datapoints and  $K$  the kernel of bandwidth  $b$ . Here, the kernel  $K$  needs to be a positive, symmetric and normalized function, but otherwise it can be chosen freely. [3]

To estimate the probability density of the rupture force  $pdf$ , it has been recommended to choose the normal distribution as kernel function and assign each unbinding event's measurement error as bandwidth. [10] This way, more reliable datapoints (with lower standard deviation) get a higher weight and contribute more to the outcome than such with a larger measurement error. The  $pdf$  for a force distribution can then be calculated as

$$pdf(F) = \frac{1}{n} \sum_{i=1}^n \frac{1}{\sqrt{2\pi s_i^2}} \exp\left(-\frac{(F - F_i)^2}{2s_i^2}\right) \quad (1.10)$$

for the measured unbinding forces  $F_i$  and their standard deviations  $s_i$ . [3]

### 1.3.6. Spring constant determination

For correct data analysis, it is paramount to determine the spring constants of all used AFM tips. There are a few methods available to perform spring constant determination.

The thermal noise method is widely used as it is considered to be both accurate and simple. It assumes the cantilever to be a spring with a spring constant  $k$  and connects its thermal motion to its energy via the equipartition theorem according to

$$\frac{1}{2}k\langle z^2 \rangle = \frac{1}{2}k_B T \quad (1.11)$$

which can be rearranged to

$$k = \frac{k_B T}{\langle z^2 \rangle} \quad (1.12)$$

with  $\langle z^2 \rangle$  denoting the mean square of the cantilever's thermal amplitude fluctuations.

To obtain  $\langle z^2 \rangle$ , the cantilever is retracted from the surface so it can oscillate freely. Assuming the cantilever to behave like a simple harmonic oscillator,  $\langle z^2 \rangle$  can be calculated by monitoring the free cantilever's oscillations over a certain time, performing a Fourier transformation of the squared noise signal to obtain the power spectral density and then fitting it with a Cauchy distribution:

$$A = A_{white} + \frac{A_0 \omega_0^4}{(\omega^2 - \omega_0^2)^2 + (\omega \omega_0 / Q)^2} \quad (1.13)$$

Here,  $A_{white}$  denotes white noise floor,  $A_0$  the zero frequency amplitude,  $\omega_0$  the radial resonance frequency and  $Q$  the quality factor.

In the frequency domain, noise becomes visible in two ways: First, as the broadband white noise, which is eliminated by subtracting the component  $A_{white}$ . Second, noise will appear as distinct contributions at off-resonance-frequencies, meaning the corresponding frequency ranges can be excluded from further calculations. Therefore, integration of  $A$  over the frequency after subtraction of  $A_{white}$  and under exclusion of off-resonance peaks yields  $\langle z^2 \rangle$ .

However, two important corrections to this model are necessary. For once, cantilevers are not sufficiently described as single-mode harmonic oscillators, but must be considered as multimode harmonic oscillators. Each mode of oscillation  $i$  (with  $i=1$  denoting the fundamental) can be described as a separate harmonic oscillator with a spring constant  $k_i$  for which the equipartition theorem yields

$$k_i = \frac{k_B T}{\langle z_i^2 \rangle} \quad (1.14)$$

with  $\langle z_i^2 \rangle$  denoting the  $i$ -th mode's mean square deflection, with

$$\langle z^2 \rangle = \sum_0^\infty \langle z_i^2 \rangle. \quad (1.15)$$

## 1. Introduction

---

However, as the spring constants  $k_i$  get higher for higher modes, the corresponding  $\langle z_i^2 \rangle$  get smaller. As a result, the fundamental mode contains the main part of the harmonic oscillator's energy. It can be shown that  $\langle z_1^2 \rangle$  and  $\langle z^2 \rangle$  are connected by a proportionality constant. This means that performing the analysis described above for the first mode requires a correction factor.

This effect is relevant, yet another correction is even more important. It has to be considered that detection via the optical lever method provides information on the angular changes of the cantilever position, not on its absolute deflection. The bending mode of the cantilever needs to be taken into account to connect its absolute distance change to angular changes. Beam theory provides an analytic solution for rectangular cantilevers, including both corrections:

$$k = 0.817 \frac{k_B T}{\langle (z_1^*)^2 \rangle} \quad (1.16)$$

For V-shaped cantilevers, numerical calculations showed that another prefactor is necessary:

$$k = 0.764 \frac{k_B T}{\langle (z_1^*)^2 \rangle} \quad (1.17)$$

In both cases,  $\langle (z_1^*)^2 \rangle$  denotes the fundamental mode's mean square displacement as determined by the optical lever method and the procedure described above. [3], [4]

### 1.3.7. Energy surface of a receptor-ligand interaction

For the unbinding of a receptor-ligand complex



the equilibrium dissociation constant  $K_D$  is connected to the energy barrier between the bound and the unbound state  $\Delta G$  via

$$\Delta G = -k_B T \ln(K_D) \quad (1.19)$$

with  $k_B$  denoting the Boltzmann constant and  $T$  the temperature. The equilibrium dissociation constant  $K_D$  is connected to the kinetic parameters according to

$$K_D = \frac{k_{off}}{k_{on}} \quad (1.20)$$

with  $k_{off}$  being the empirical dissociation rate constant and  $k_{on}$  being the empirical association rate constant.

Typically, AFM-based SMFS experiments take place over timescales of milliseconds up to seconds. At these timescales, the lifetime of the bound state is assumed to depend on thermal fluctuations.

For an energy barrier of height  $E_b$  and a natural oscillation frequency  $\tau_{osc}$ , the bond's lifetime  $\tau$  can be given by an Arrhenius dependency:

$$\tau(0) = \tau_{osc} \exp\left(\frac{E_b}{k_B T}\right) \quad (1.21)$$

Figure 1.6 shows the energy surface of a receptor-ligand complex averaged and projected along a coordinate given by the pulling direction. Here, the parameter  $x_\beta$  denotes the distance of the energy barrier's maximum from the energy minimum (given by the bound state). Pulling on the molecular complex with a force  $F$  is assumed to lower the energy barrier according to: [2]

$$\tau(F) = \tau_{osc} \exp\left(\frac{E_b - x_\beta F}{k_B T}\right) = \tau(0) \exp\left(\frac{-x_\beta F}{k_B T}\right) \quad (1.22)$$

The dissociation rate of a receptor-ligand bond is then given as the inverse of the lifetime  $\tau(0)$  with no force applied: [11]

$$k_{off} = \frac{1}{\tau(0)} \quad (1.23)$$

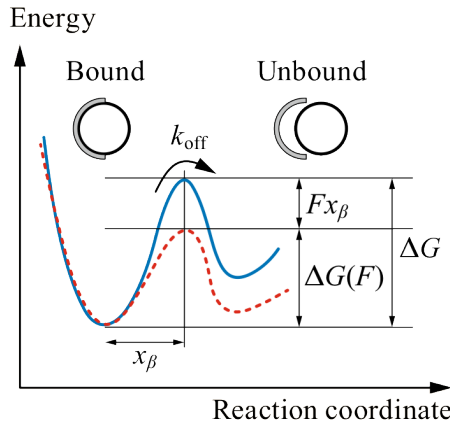


Figure 1.6.: The influence of force exertion on the energy barrier of a receptor-ligand complex. From Bhushan et al. [2]

### 1.3.8. Dynamic force spectroscopy

As can be seen from the description of the force-distance cycle in section 1.3.3, the force is not kept constant over one force-distance cycle, as equation (1.22) would require to calculate the bond lifetime. In dynamic force spectroscopy (DFS) the relationship between the unbinding force and the loading rate  $r$  is studied. The loading rate is obtained as the time-derivative of the force  $F$  immediately before the rupture occurs

$$r = \frac{dF}{dt} \quad (1.24)$$

## 1. Introduction

---

with  $t$  denoting the time. [2] Instead of the force, the absolute pulling rate  $v$  is kept constant over the course of one force-distance cycle. This means that upon binding, the molecular complex is subjected to a linear force ramp

$$F(t) = k_{eff}vt. \quad (1.25)$$

The effective spring constant  $k_{eff}$  can be obtained as the slope at the very end of the rupture curve. The loading rate  $r$  can then be calculated as [3]

$$r = k_{eff}v. \quad (1.26)$$

A number of theoretical models exist to describe the relationship between the most probably rupture force  $F^*$  and the loading rate  $r$ , the first and simplest of them being Bell-Evans model. By fitting the unbinding data collected from SMFS experiments performed for several pulling rates, a number of parameters characterizing the specific interaction between the binding partners can be extracted, most prominently the rate dissociation constant  $k_{off}$ . [2]

Some of these models will be discussed in section 1.4.

## 1.4. Models in dynamic force spectroscopy

### 1.4.1. Bell-Evans model

The Bell-Evans model was developed by Evans & Ritchie [12] and is based on the work of Bell [13]. Bell developed the theoretical framework on bond lifetime and its dependency on an external force (as briefly discussed in section 1.3.7) in order to study adhesive interaction between cells. [13] Later, Evans & Ritchie applied this framework to a system in which the force is not constant, but varies over time in the form of a linear force ramp, laying the foundation for data evaluation in DFS. In their analysis, they utilized Kramers' theory, which analyzes a particle's escape over a potential barrier driven by thermal noise. [12].

Bell-Evans model assumes that throughout the unbinding event, the system maintains a quasi-equilibrium state as the rupture takes place over a timescale exceeding that of diffusional relaxation. The molecular bond's survival probability  $S(t)$  (the bond's chance of surviving for a time  $t$ ) while being subjected to an external pulling force  $F(t)$  is determined by the master equation

$$\frac{dS(t)}{dt} = -k(t)S(t) \quad (1.27)$$

with  $k(t)$  being the time-dependent kinetic dissociation rate. Solving this first-order differential equation for  $S(t)$  gives

$$S(t) = \exp \left[ - \int_0^t k(t') dt' \right]. \quad (1.28)$$

The probability distribution  $p(F)$  of rupture forces  $F$  is connected to  $S(t)$  via

$$p(F)dF = -\dot{S}(t)dt \quad (1.29)$$

which can be rearranged and combined with equation (1.28) to

$$p(F) = \frac{k(F)}{\frac{dF}{dt}} \exp \left( - \int_0^F \left[ \frac{k(F')}{\frac{dF}{dt}} \right] dF' \right). \quad (1.30)$$

Now the expression for the kinetic rate  $k(F)$  as derived by Bell (compare to equations (1.22) and (1.23), as the lifetime  $\tau(F)$  and  $k(F)$  inversely relate to each other)

$$k(F) = k_{off} \exp \left( \frac{Fx_\beta}{k_B T} \right) \quad (1.31)$$

as well as the expression for a linear force ramp as given in equation (1.25) can be inserted into equation (1.30). Together, these equations yield the following expression for the probability distribution of rupture forces as dependent on the loading rate  $r$ :

$$p(F) = \frac{k_{eff}}{r} \exp \left( \frac{Fx_\beta}{k_B T} - \frac{k_{off}k_B T}{rx_\beta} \left[ \exp \left( \frac{Fx_\beta}{k_B T} \right) - 1 \right] \right) \quad (1.32)$$

From this expression, the most probable rupture force  $F^*$  can be calculated to

$$F^* = \frac{k_B T}{x_\beta} \ln \left( \frac{x_\beta \cdot r}{k_B \cdot T \cdot k_{off}} \right) \quad (1.33)$$

which shows a logarithmic dependence on the loading rate  $r$ . In a semilogarithmic representation of rupture force versus logarithmic loading rate, this gives a linear curve shape. [3] The most probable rupture force of a given dataset is obtained as the force for which the force distribution (compare section 1.3.5) has its maximum. Fitting the data collected from different pulling rates with equation (1.33) gives  $k_{off}$  and  $x_\beta$ , characterizing the bond's energy barrier (see figure 1.6 ).

In some systems, the receptor-ligand complex has to overcome not one but two or more sequential energy barriers in order to unbind. For these cases, Bell-Evans model predicts a series of linear regimes with different slopes following upon each other in the semilogarithmic plot. Here, each regime corresponds to one energy barrier and fitting the regimes individually with Bell-Evans model provides the characteristic parameters  $k_{off}$  and  $x_\beta$  for each barrier.

However, if the semilogarithmic representation of the experimental data does not show a series of linear regimes but a nonlinear curve shape, an interpretation with Bell-Evans model would predict a

## 1. Introduction

---

complicated energy landscape consisting of many energy barriers. In these cases, the assumptions underlying Bell-Evans model may not hold up and lead to incorrect results, making it necessary to choose a more elaborate model. [2]

### 1.4.2. Humer-Szabo model and Dudko model

Related models using different parameters to describe the energy landscape were proposed by Hummer & Szabo [14] and Dudko [15].

Hummer & Szabo analyzed the phenomenological description given by Bell-Evans model which is based on Bell's formula (equation (1.31)) and describes the bond's free energy landscape with only one parameter  $x_\beta$ . They point out that while Bell-Evans model appears to have general validity, according to simulations it does not offer an adequate description over the experimentally accessible pulling regimes. Bell's formula assumes that the coordinate of the transition state is independent of the pulling force, while in fact it can be expected to vary due to the combined influence of the pulling potential and molecular potential of the bond. [14] Dudko, Hummer and Szabo suggested modifications of the Bell-Evans model to account for the variation of the transition state, using different descriptions of the bond's free energy surface. [2]

Hummer & Szabo proposed a harmonic potential including a cusp-like feature at the coordinate  $x_\beta$ :

$$U_0(F) = k_B T \Delta G_\beta \left( \frac{x}{x_\beta} \right)^2 \quad \text{for } x < x_\beta \text{ and } U_0(F) = -\infty \text{ otherwise} \quad (1.34)$$

Dudko performed a similar analysis using a linear-cubic energy surface:

$$U_0(F) = \Delta G_\beta \left( \frac{3}{2} \frac{x}{x_\beta} - 2 \left( \frac{x}{x_\beta} \right)^3 \right) \quad (1.35)$$

Again Kramers' theory can be used to obtain expressions for  $k(F)$  and  $p(F)$ :

$$k(F) = k_{off} \left( 1 - \frac{\mu F x_\beta}{\Delta G_\beta} \right)^{1/\mu-1} \exp \left( \frac{\Delta G_\beta}{k_B T} \left[ 1 - \left( 1 - \frac{\mu F x_\beta}{\Delta G_\beta} \right)^{1/\mu} \right] \right) \quad (1.36)$$

$$p(F) = \frac{k(F)}{r} \exp \left( \frac{k_{off} k_B T}{r x_\beta} \right) \exp \left( - \frac{k(F) k_B T}{r x_\beta} \left[ 1 - \left( 1 - \frac{\mu F x_\beta}{\Delta G_\beta} \right)^{-1/\mu} \right] \right) \quad (1.37)$$

Here,  $\mu = 2/3$  gives the quadratic free energy surface (Hummer-Szabo model) and  $\mu = 1/2$  gives the linear-cubic free energy surface (Dudko model). Using the equations for  $k(F)$  and  $p(F)$ , the *mean rupture force*  $\langle F \rangle$  as a function of the loading rate  $r$  can be calculated to:

$$\langle F \rangle \cong \frac{\Delta G_\beta}{\mu x_\beta} \left\{ 1 - \left[ \frac{k_B T}{\Delta G_\beta} \ln \left( \frac{k_{off} k_B T}{x_\beta r} \exp \left( \frac{\Delta G_\beta}{k_B T} + \gamma \right) \right) \right]^\mu \right\} \quad (1.38)$$

Above,  $\gamma \approx 0.577$  denotes the Euler-Mascheroni constant. Formally setting  $\gamma = 0$  gives a good approximation of the most-probable rupture force, corresponding to the maxima of the force distributions. Further, setting  $\mu = 1$  and  $\Delta G_\beta$  (independent of  $\mu$ ), equation (1.38) leads back to Bell-Evans model (compare equation (1.33)).

For  $\mu \neq 1$ , equation (1.38) is valid for force values up to a critical force  $F_c = \Delta G_\beta / (rx_\beta)$ , as the underlying assumptions in Kramers' theory no longer hold up above this limit. [3], [15]

### 1.4.3. Friddle model

A model developed by Friddle, Noy & de Yoreo [16] treats cases in which the experimental data shows a nonlinear dependence of rupture force versus loading rates in the semilogarithmic representation. Such cases are frequently encountered and as discussed in section 1.4.1, Bell-Evans model interprets such rupture force spectra as comprising two linear regimes, each corresponding to a separate energy barrier. In their paper, Friddle et al. provide an evaluation strategy which interprets such a nonlinear rupture force spectrum as being attributed not to two distinct energy barriers, but two kinetic regimes. At lower loading rates and rupture forces, spontaneous rebinding is expected to occur at any time. Assuming that relaxation happens at faster timescales than all other processes occurring in the system, similar to equation (1.27) in the derivation of Bell-Evans model, the probability  $S_b(t)$  of finding the molecular complex in the bound state is determined by

$$\frac{dS_b(t)}{dt} = -S_b(t)k_u(t) + S_u(t)k_b(t) \quad (1.39)$$

with  $S_u(t)$  denoting the probability of finding the bond in the unbound state,  $k_b(t)$  the kinetic rate of binding and  $k_u(t)$  the rate of unbinding. Both rates are time-dependent as they depend on the acting force. For  $k_u(t)$ , Bell's expression (equation (1.31)) is used with an additional term accounting for the harmonic potential given by the stiffness of the pulling device (with a spring constant  $k$ ):

$$k_u(F) = k_{off} \exp \left[ \frac{1}{k_B T} \left( Fx_\beta - \frac{1}{2} kx_\beta^2 \right) \right] \quad (1.40)$$

The authors justify their choice by stating that it could be shown that the loading rates reached in the laboratory are several orders of magnitudes lower than such at which nonlinearities associated with a force-dependent transition state occur. Further, they assume  $k_b(F)$  to depend on the energy stored in a spring that is extended between the spring minimum (at a displacement  $F/k$ ) and the bond's energy barrier (at  $x_\beta$ ) according to

$$k_b(F) = k_{on} \exp \left[ -\frac{1}{k_B T} \frac{k}{2} \left( \frac{F}{k} - x_\beta \right)^2 \right]. \quad (1.41)$$

## 1. Introduction

---

Then,  $k_u(F)$  and  $k_b(F)$  are connected via

$$k_b(F) = k_u(F) \exp \left[ \frac{1}{k_B T} \left( \Delta G_{bu} - \frac{F^2}{2k} \right) \right] \quad (1.42)$$

with the bond's equilibrium free energy  $\Delta G_{bu}$  referring to the free energy difference between the bound and unbound state.

As illustrated in figure 1.7, the rates  $k_u(F)$  and  $k_b(F)$  assume an equal value at an equilibrium force

$$F_{eq} = \sqrt{2k\Delta G_{bu}} \quad (1.43)$$

which is the minimum force required to break the molecular bond. Using equations (1.42) and (1.43), the rebinding rate  $k_b(F)$  can be expressed as a function of  $k_u(F)$  and  $F_{eq}$ . This means that the whole unbinding process can be described by a set of three parameters  $x_\beta$ ,  $k_{off}$  and  $F_{eq}$ , one more than in Bell-Evans model. As also illustrated in figure 1.7,  $k_b(F)$  shows a fast decrease for  $F > F_{eq}$  because of the term  $-F^2/2k$  in equation (1.42). Therefore, in the regime  $F > F_{eq}$  the unbinding process is mainly governed by the dissociation rate  $k_u(F)$ .

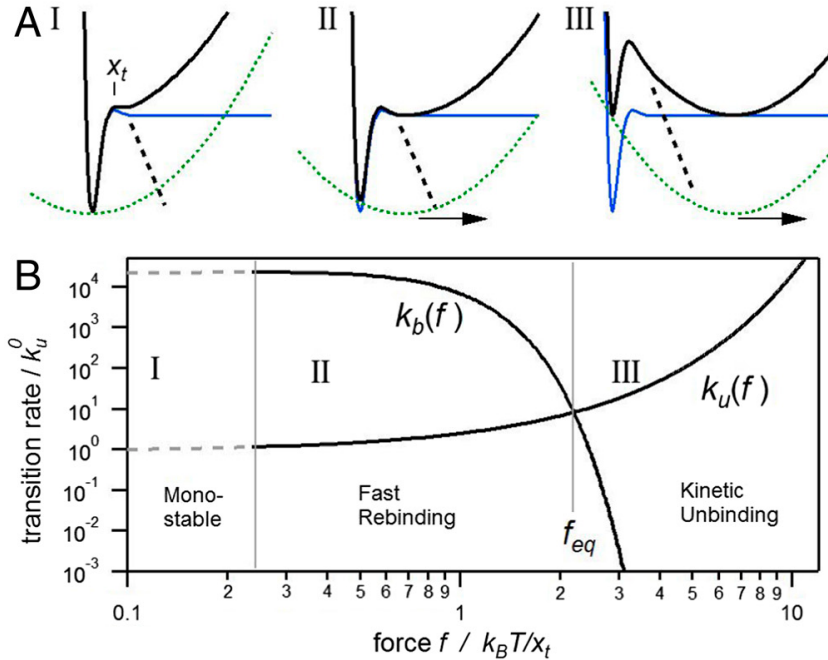


Figure 1.7.: Potential profiles and kinetic rates in Friddle's model over the three regimes (I), (II), (III). In regime (I), the bond is subjected to no load and the minima of the two potentials (bond potential and spring potential) coincide. In regime (II), the bond is subjected to load, meaning that there are two potential minima. In regime (III), the bond has been loaded to an extent that creates a potential barrier between the two minima, making rebinding less probable.  $k_u^0$  denotes the kinetic off-rate  $k_{off}$  at zero force. From Friddle et al. (2012) [16]

It can be shown that under these assumptions the mean rupture force  $\langle F \rangle$  depends on the loading rate  $r$  according to

$$\langle F \rangle = F_{eq} + F_\beta \exp\left(\frac{1}{R(F_{eq})}\right) E_1\left(\frac{1}{R(F_{eq})}\right) \quad (1.44)$$

with  $R(F_{eq}) = r/k_u(F_{eq})F_\beta$ ,  $F_\beta = k_B T/x_\beta$  and  $E_1(z) = \int_z^\infty e^s/s ds$ . By utilizing the approximation  $e^z E_1(z) \cong \ln(1 + e^{-\gamma}/z)$  equation (1.44) can be simplified to

$$\langle F \rangle = F_{eq} + F_\beta \ln\left(1 + \frac{r}{F_\beta k_{off}} \exp\left[-\gamma - \frac{F_{eq}}{F_\beta} + \frac{k_B T}{2 F_\beta^2}\right]\right). \quad (1.45)$$

From equation (1.45), the two formerly discussed regimes can be derived:

- For low loading rates, a linear regime with  
 $\langle F \rangle_{r \rightarrow 0} = F_{eq} + r/k_u(F_{eq})$  and
- for fast loading rates, a nonlinear regime with  
 $\langle F \rangle_{r \rightarrow \infty} = F_\beta \ln(e^{-\gamma} R(0))$ , leading to an  $\ln(r)$ -dependence similar to Bell-Evans model. [16]

Figure 1.8 shows rupture force distributions calculated numerically based on equation 1.39 for a harmonic probe potential. The graph illustrates the expected behavior, as the mean rupture force stays almost constant for lower loading rates (corresponding to the rebinding regime), but increases for higher loading rates. As the loading rate increases further, the distributions broaden. [17]

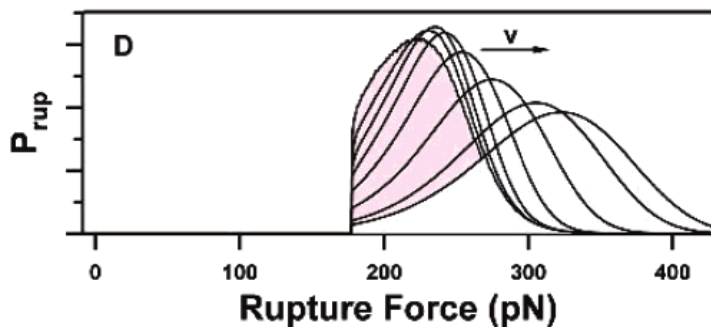


Figure 1.8.: Numerically calculated rupture force distributions assuming a harmonic probe potential, for increasing loading rate for  $k = 0.8 \text{ N/m}$  for pulling rates from  $8 \text{ nm/s}$  up to  $621 \text{ nm/s}$ . From Friddle et al. (2008) [17]

#### 1.4.4. Friddle model for multiple bonds

Friddle et al. also provide an analysis for the case of multiple bonds being formed between the tip and the sample surface. For a total number of possible bonds  $N_t$ , analyzing the dependence of the number of currently present bonds  $N_b$  on the acting force  $F$  shows that like for the single bond model, two regimes can be expected. For low loading rates, the number of bonds  $N(F)$  is meta-stable up to an equilibrium force  $F_{eq}$ , while for higher loading rates bond rupture occurs rapidly after the failure of the first bond. The dependence of rupture force on the loading rate for the equilibrated number  $N$  of bonds that would be present at zero force can be summed up in the following equation:

$$\langle F \rangle_N = F_{eq} + NF_\beta \exp\left(\frac{N}{R(F_{eq}/N)}\right) E_1\left(\frac{N}{R(F_{eq}/N)}\right) \quad (1.46)$$

with  $R(F_{eq}/N) = r/(k_u(F_{eq}/N)F_\beta)$ . Using the same approximation as for the single bond, the formula can be simplified to

$$\langle F \rangle_N = F_{eq} + NF_\beta \ln\left(1 + \frac{r}{NF_\beta k_{off}} \exp\left[-\gamma - \frac{F_{eq}}{NF_\beta} + \frac{k}{2} \frac{k_B T}{F_\beta^2}\right]\right). \quad (1.47)$$

from which the two regimes can be deduced analogously. [16]

### 1.5. Extracting information from force distributions

For a given dataset, the collected rupture forces can be represented in a probability distribution function (PDF) as discussed in section 1.3.5. This can be done for one pulling rate. However, as the effective spring constant may vary (compare section 1.3.4), the datapoints from one pulling rate will spread over a whole range of loading rates, making the distribution harder to interpret.

Theoretical papers usually treat force distributions for different loading rates, not pulling rates. The development of force distributions over a spectrum of loading rates may give valuable insight into the energy landscape underlying the interaction under investigation.

Simulations show that the rupture force distributions for different loading rates are expected to exhibit characteristic trends or features, depending on the overall shape of the potential, on whether or not there are intermediate states present and by which kinetic rates transitions from the ground state to higher states and back occur. Depending on these variables, the overall broadening of the force distribution functions for higher loading rates can be more or less pronounced and in some configurations, bimodalities (double peaks) can appear. [18], [19]

One way to investigate the development of the force distributions relies on loading-rate-wise binning of the data. The force distribution can then be calculated individually for each bin. Binning of force spectroscopy data has already been applied by various teams. For example, Rico & Moy (2007) [20] and Hane et al. (2014) [21] performed binning of their data and subsequently fitted it with one Gaussian function per loading-rate-bin to extract the most-probable rupture force and a standard error for the respective segment.

If multiple peaks are present in the force distribution, multiple Gaussian functions can be fitted onto it. For example, Carvalho et al. (2010) [22] could identify multiple binding events occurring in their system by fitting multiple Gaussian functions.

Each Gaussian fit can be interpreted as one population with a mean value and a standard deviation. However, this is a simplification, as actually force distribution function are not expected to exhibit the shape of a normal distribution, but an asymmetrical curve shape (compare figure 1.8).

Grouping of the data into populations allows to fit these populations individually and investigate them with regard to a possible multibond codependency. If a multibond model is available for the selected fitting model (like for Friddle model, see section 1.4.4), two or more populations can be related to each other by this model.

If no such interconnection can be determined, the populations may result from different, independent types of interactions occurring between the probe and the sample.

## 1.6. C-reactive protein

C-reactive protein (CRP) is a member of a protein family called “pentraxins”. One CRP molecule consists of five identical subunits of about 23 kDa, comprising 206 amino acid residues each, which are noncovalently associated in pentameric symmetry and form a pore in the centre. [23] Each subunit is made up by antiparallel beta sheets which are folded in an arrangement which is referred to as flattened jellyroll topology. Each subunit has a binding site for phosphocholine.

CRP is a plasma protein exhibiting a high degree of phylogenetic conservation. There are known homologues in many species, including both vertebrates and invertebrates. [24]

The name ‘C-reactive protein’ originates from its discovery, which occurred in the laboratory of Oswald Avery while performing studies on patients infected with *Streptococcus pneumoniae*. While running tests on blood sera obtained from patients in the acute phase of the disease, it was discovered that these sera contained an agent which had the ability to precipitate a component of the pneumococcal

## 1. Introduction

---

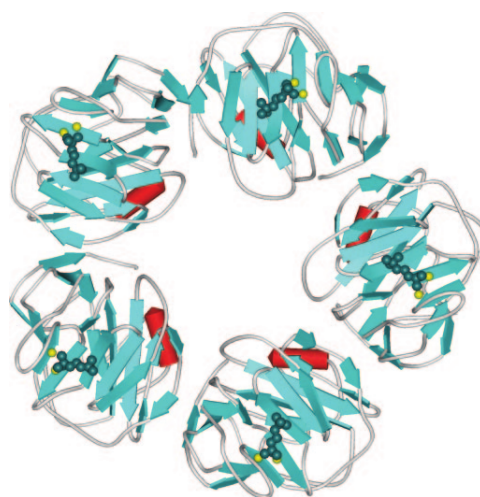


Figure 1.9.: Crystal structure of CRP with bound phosphocholine,  $\text{Ca}^{+2}$  ions in yellow, phosphocholine in green [24]

cell wall, the ‘C’ polysaccharide. This gave it the name ‘C-reactive’ protein. A few decades later, phosphocholine was found to be the specific binding partner of CRP in C polysaccharide. Figure 1.9 shows the crystal structure of a CRP molecule. [24]

Today we know that although CRP has the highest affinity for phosphocholine, it can bind to a number of other ligands, which can originate both from the same organism (autologous) or from an intruder (extrinsic). Upon binding, CRP will cause aggregation or precipitation of the molecules exhibiting these ligands. [23]

CRP is what is called a pattern recognition molecule. It recognizes and binds to molecular sites or configurations which are typically not exposed in a healthy organism, but are accessible in damaged cells or occur on pathogen surfaces. [24] Therefore, autologous ligands include membrane components of damaged or apoptotic cells, while extrinsic ligands may originate from intruding bacteria or fungi. [23]

When an bacterial infection or tissue damage occurs and leads to an inflammation, CRP levels in the blood plasma increase rapidly, reaching a 1000-fold or more of the normal concentration after just a few hours. This makes it very important for clinical purposes, as CRP can be used as a reliable marker for an inflammatory state in a patient. [24]

The rapid increase in CRP levels after encountering an inflammatory stimulus is part of the acute-phase response. The acute-phase describes the initial and non-specific reaction of an organism to an infection, tissue damage or inflammation. During the acute-phase, the synthesis-rate of some proteins – like CRP – gets up-regulated. [23]

The biological function of CRP is complex and depends on the context in which it is acting, but one of its basic functions seems to be to recognize pathogens or damaged cells, then guide other players of the complement system and phagocytic cells to the affected sites. [24]

## 1.7. Mesenchymal stem cells and RAGE receptors

Mesenchymal stem cells (MSC) are cells which have the ability to differentiate into various types of cell lineages (meaning they are multipotential) and which are self-renewing. They are of medical interest, as they offer a lot of potential in tissue engineering. Adding chemical supplements can lead MSC to differentiate into the desired cell type. [25]

Advanced glycation end-products (AGEs) are produced nonenzymatically in a complex series of chemical rearrangements and are known to accumulate in tissues of elderly people. They have been linked to a number of age-related ailments like diabetes or a decrease in bone strength and a resulting increased risk of skeletal fracturing. Receptors for AGEs (RAGEs) are expressed on the surface of MSC. It could be shown that the expression of RAGE in MSC (as well as in a few other cell types) is upregulated in the presence of AGEs. [26]

## 2. Materials and Methods

### 2.1. AFM and cantilever specifications

All SMFS measurements were performed on two SPMs setups produced by Agilent Technologies of model types Agilent 5500 SPM and Agilent LE 5100 SPM. The utilized AFM scanners were produced by Agilent Technologies / Keysight Technologies and had the model numbers N9520A, N9524A and N9524A-69012. As measurement software, PicoView versions 1.20 (for Agilent 5500 SPM) and 1.12 (for Agilent LE 5100 SPM) were used.

For all measurements, silicon nitride AFM cantilever chips produced by BRUKER were used. All chips were equipped with six individual cantilevers (referred to as cantilevers A, B, C, D, E, F) which differed in spring constant, size and shape. Figure 2.1 shows a microscope image of an MSCT-type chip with a laser spot focused on cantilever C. In the image, cantilevers B to F are visible from left to right. Cantilever A is positioned at the other end of the rectangular chip.



Figure 2.1.: Microscope image of an MSCT chip by BRUKER, cantilevers B C D E F visible, laser focused on cantilever C

BRUKER's MSCT-type cantilevers were chosen for all SMFS measurements. Depending on the chip, the following cantilevers were used (nominal parameters given for measurement in air):

- B (rectangular, nominal spring constant 20 pN/nm and resonance frequency 15 kHz)
- C (triangular, nominal spring constant 10 pN/nm and resonance frequency 7 kHz)
- D (triangular, nominal spring constant 30 pN/nm and resonance frequency 15 kHz)

BRUKER's MSNL-10-type cantilever chips were chosen for contact mode imaging. All images were recorded using cantilever D (nominal spring constant 30 pN/nm and resonance frequency 15 kHz).

## 2.2. Cantilever tip and sample functionalization

### 2.2.1. Aminofunctionalization with APTES

Aminofunctionalization of the silicon nitride cantilever tips and mica sheets was performed in a gas phase reaction using (3-aminopropyl)triethoxysilane (APTES), as illustrated in figure 1.2 on page 6. Aminofunctionalization was performed under exclusion of air and moisture in a dessicator (with a capacity of 5 l) filled with argon gas. Two small trays were put inside. They were filled with 30 ml of vacuum-distilled APTES and 10 ml of triethylamine (TEA). The cantilever chips and mica sheets were put next to the trays on an inert, clean surface. Next, the dessicator was closed. After incubating for about 120 minutes, the desiccator was opened, the trays with APTES and TEA were removed and the desiccator was again filled with argon gas. After this, the cantilever chips and mica sheets were left inside the desiccator for two days before storage under argon. [7], [8]

### 2.2.2. Sample preparation

Sample preparation was performed in three steps: First, freshly cleaved mica sheets were APTES-coated in a procedure described in section 2.2.1 and subsequently stored under argon gas until further use. Second, 10 mg of ethylene glycol bis(succinimidyl succinate) crosslinkers, EGS for short, were dissolved in 10 ml of chloroform in a small beaker, one mica sheet was placed inside and 50 µl of TEA were added as a catalyst. The beaker was covered with a lid and the mica was left to incubate for two hours. Afterwards, it was removed from the solution, washed in chloroform (3 times 5 minutes), dried with nitrogen gas and placed on a fresh parafilm in a polystyrene dish.

As a third and final step, a 50 µl droplet of 20 µg/ml human CRP protein (stored at -20 °C, produced by Biorbyt, catalogue number orb391529) [27] suspended in phosphate buffered saline (PBS) buffer was pipetted onto the center of the EGS-functionalized mica sheet. The PBS used here and throughout all other steps of sample preparation and tip functionalization contained 137 mM NaCl, 2.7 mM KCl, 10 mM Na<sub>2</sub>HPO<sub>4</sub> and 1.8 mM KH<sub>2</sub>PO<sub>4</sub> in purified water and was adjusted to pH 7.4 with HCl. [28]

## 2. Materials and Methods

Further, a few drops of water were pipetted onto the parafilm at a safe distance from the mica sheet to avoid evaporation of the protein droplet, the dish was covered with a lid and stored at 4 °C over night for incubation. In the next morning, the mica sheet was mounted onto an AFM sample plate and the sample was washed 50 times inside the AFM fluid cell with PBS before the first measurement was started. From then on, the sample was stored in PBS at 4 °C over night and used for measurements for up to one week.

### 2.2.3. Antibody-coupling via acetal-PEG-NHS linker

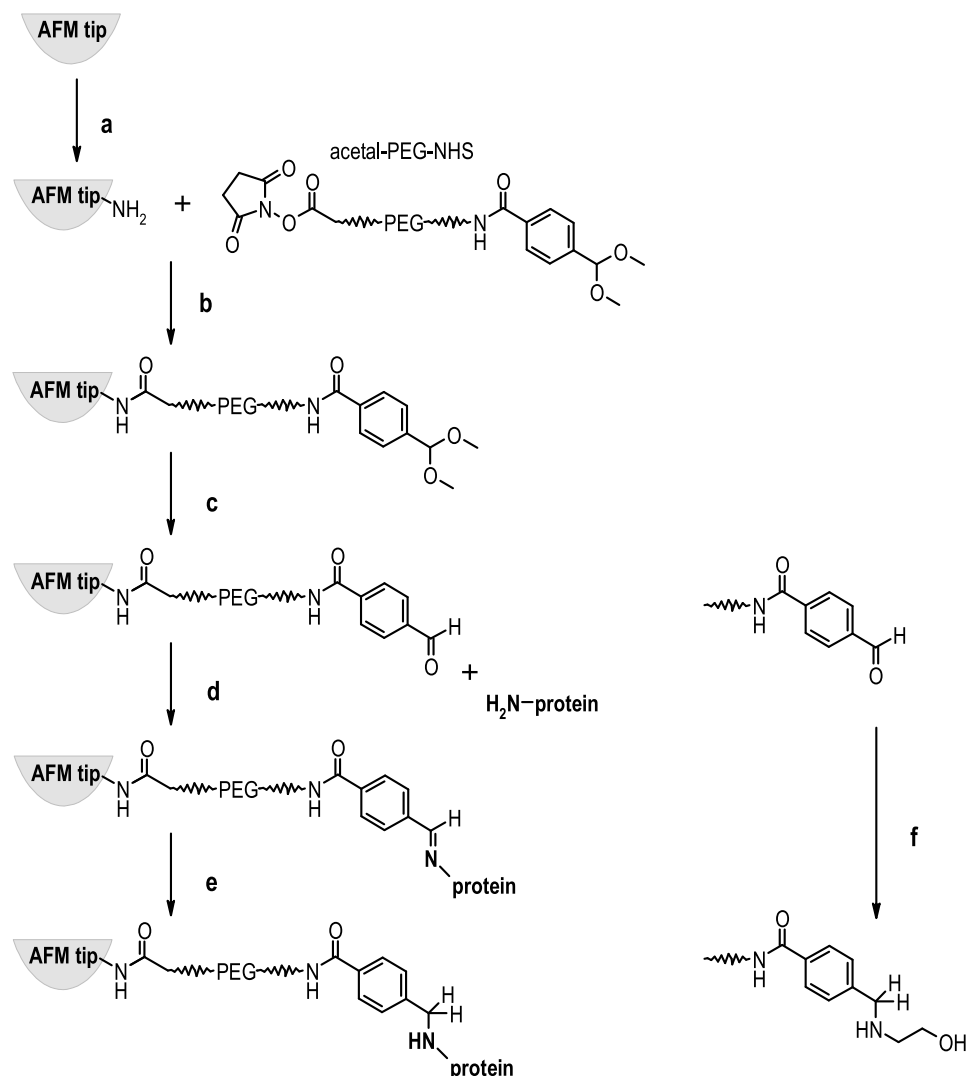


Figure 2.2.: Protein coupling to an AFM tip via acetal-PEG-NHS linker. From Wildling et al., Supplementary. (2011). [6]

Figure 2.2 illustrates the chemical reactions underlying the functionalization procedure. For all experiments, monoclonal antibodies (anti-CRP) were coupled to APTES-coated silicon nitride cantilever tips via acetal-PEG-NHS linkers (compare section 1.3.2).

After APTES-coating of the tips (a), 1 mg of acetal-PEG-NHS linkers were dissolved in 500 µl of chloroform and transferred into a reaction chamber (made of Teflon). Up to five cantilever chips were placed into the chamber and TEA was added as a catalyst, before the solution was mixed carefully, the chamber was covered with a lid and then left to incubate for two hours. During this time, the linker's NHS-groups could bind to the free NH<sub>2</sub>-groups on the tip (b). After this step, the cantilevers were rinsed in chloroform (3 times 10 minutes) and dried under nitrogen.

Following the washing step, the cantilevers were either stored under argon for a few weeks or the functionalization was continued immediately. In the latter case, the cantilevers were transferred into a 1 % water-based citric acid solution for 10 minutes. This step was used to convert the free acetal-groups into reactive aldehyde-groups (c). After rinsing in water (3 times 5 minutes) and drying with nitrogen gas, the cantilevers were placed on a fresh piece of parafilm on a polystyrene Petri dish and arranged in a star-formation, with the tips pointing towards the center of the star. 33 µl of 1.1 µM anti-CRP (formerly stored at -20 °C, diluted in PBS) were pipetted in the center of the star so as to cover all tips. Next, 2 µl of a freshly prepared solution comprising 1 M sodium cyanoborohydride and 20 mM NaOH made of

- 13 mg NaCNBH<sub>3</sub> (toxic)
- 20 µl 100 mM NaOH
- 180 µl water

were added to the protein droplet. The cantilevers were covered with a lid and left to incubate for two hours. During this time, the antibodies coupled to the aldehyde-groups via lysine-residues (d, e). To block unused aldehyde-groups, 5 µl of ethanolamine (1 M, adjusted to pH 8.0) were added and the solution was incubated for another 10 minutes while covered by a lid (f). Finally, the cantilevers were washed (3 times 5 minutes) in PBS (pH 7.4) and stored in a well plate under PBS at 4 °C for up to one week before use. [5], [6]

#### 2.2.4. MSC and anti-RAGE

The framework developed for analysis of the data on CRP and anti-CRP was also applied to evaluate SMFS data recorded by Sarah Rautnig for her master's thesis (2019) under the supervision of Andreas

## 2. Materials and Methods

---

Ebner at the Institute of Biophysics, Johannes Kepler University, Linz.

As was formerly shown by Christoph Mayr in his master's thesis (2019), force spectroscopy on MSC can be performed with RAGE-antibodies (anti-RAGE).

SMFS experiments were performed on MSC suspended in a petri dish in mesenchymal stem cell growth medium and fixated with 4 % formaldehyde, stored at (2 to 8) °C.

Monoclonal RAGE (A11) antibodies of mouse origin, produced by Santa Cruz Biotechnology Inc., were attached to an AFM tip via an acetal-linker analogous to the tip functionalization procedure used for anti-CRP.

For details please refer to the master's thesis of Sarah Rautnig.

### 2.3. Experimental approach

#### 2.3.1. SMFS measurements

SMFS experiments studying the interaction between human CRP protein and monoclonal anti-CRP were performed for eight distinct pulling rates ranging from 0.04 µm/s up to 2.5 µm/s. The total number of recorded force-distance cycles depended on the pulling rate, with 618 curves recorded for the slowest rate and up to a few thousand curves for faster rates. The exact data is listed in table A.1 on page 78 along with the binding probabilities of each pulling rate and the determined spring constants of the respective cantilevers.

Human CRP protein was fixated on a mica surface by APTES-coating, functionalization with EGS crosslinkers and subsequent protein coupling. Anti-CRP was attached to AFM tips by following an established functionalization protocol for acetal-PEG-NHS linkers.

Both during storage and measurement, the cantilevers and the samples were suspended in PBS (adjusted to pH 7.4). All measurements were performed at room temperature on commercial AFM setups (Agilent 5500 SPM and Agilent LE 5100 SPM, Agilent Technologies, USA). AFM scanners of model numbers N9520A, N9524A and N9524A-69012 (Agilent Technologies / Keysight Technologies, USA) were used.

First, the components of the sample fluid cell and the used tweezers were rinsed individually with a water-based sodium dodecyl sulfate (SDS) solution, isopropyl alcohol (isopropanol) and purified water. Then, the sample was placed onto the AFM's sample plate, the dried fluid cell was assembled on top of the mica sheet, fixated with a clamp and filled with PBS. For a freshly-prepared sample, 50 washing steps were performed inside the fluid cell to remove any free CRP-molecules from the solution.

### 2.3. Experimental approach

---

A cantilever functionalized with anti-CRP was restrained on the nose of an AFM scanner by a clamp. The scanner was then immediately mounted onto the AFM setup so as to submerge the tip in the PBS-filled fluid cell. This way, the tip was prevented from drying out.

Now the laser was adjusted so as to be reflected on the foremost segment of the cantilever backside (compare figure 2.1). The photodiode was inserted into the designated slot of the AFM scanner and adjusted so as to detect the laser beam. After this preparatory phase, the PC software (PicoView 1.20 or PicoView 1.12) was utilized to operate the microscope and approach the tip to the sample surface. As soon as contact was established and all parameters characterizing the desired pulling rate (notably, scan range and duration of one cycle) were defined, the measurement was started.

#### 2.3.2. Specificity proof

Three specificity proof experiments, from here on referred to as *block experiments*, were performed by

- recording a set of force-distance cycles with a certain pulling rate,
- adding free CRP to the solution in the fluid cell to block the anti-CRP on the AFM tip and
- repeating the measurement with the same pulling rate.

Two out of three block experiments were performed using the left-over 50 µl protein droplet from the sample preparation. This was collected after diluting the droplet with more PBS so as not to let the protein patch dry out, altogether acquiring 150 µl of a CRP-solution with a maximum possible concentration of 5.8 µg/ml. This is a maximum possible concentration, as it is unclear which percentage of the originally present CRP bound to the surface. For a fluid cell with a capacity of 750 µl, this gave a total maximum concentration of 1.16 µg/ml. The acquired CRP solution was subsequently stored at 4 °C for up to five days until use.

For the third block experiment, a fresh portion of CRP (10 µl of a 100 µg/ml solution in PBS) was added into the fluid cell, giving a total concentration of 1.33 µg/ml of free CRP in the solution.

For all block experiments, the cantilever was left submerged in the fluid cell to incubate for 50 minutes before recording another SMFS measurement series with identical parameters.

For the first block experiment, it was additionally attempted to recover the binding probability by washing the sample in the fluid cell anew for 50 times, cleaning the cantilever by submerging it in fresh PBS over night and then recording a third measurement series with the same scanning parameters.

## 2. Materials and Methods

---

### 2.3.3. Imaging and scratch experiments

All AFM images were recorded at room temperature using a commercial AFM setup (Agilent 5500 SPM, Agilent Technologies) with the sample suspended in PBS. Imaging was performed in static contact mode with the force set to a fixed value (constant force mode). In this mode, the deflection value is used as a feedback parameter. The gains of the feedback loop and force setpoint were optimized to achieve good image quality.

Imaging of mica following all three functionalization steps was performed:

- Mica with APTES-coating
- Mica with APTES-coating and EGS
- Mica with APTES-coating, EGS and CRP

Scratch experiments were performed by restricting the scanning range to a small area (400 nm times 400 nm), setting the gains to a very low level (to suppress the feedback mechanism) and the force to a very high value before raster-scanning over the surface in contact mode for 10 to 15 times. This way, most of the proteins and other molecules got pushed out of this area. By setting the gains and force setpoint to regular values and recording another image with a larger scan range (2 µm times 2 µm), the square-shaped “hole” could be imaged and the height profile could be analyzed.

All AFM images were processed and analyzed with Gwyddion [29].

### 2.3.4. Spring constant determination

The spring constants of all cantilever tips used for SMFS measurements were determined by the thermal noise method (see section 1.3.6).

Spring constant determination was performed at room temperature using the feature Thermal-K included in PicoView 1.20 on a standard AFM setup (Agilent 5500 SPM, Agilent Technologies) with a Thermal-K-PC-card included in the PC.

The cantilever tips, formerly stored in PBS, were rinsed in ethanol (to clean them of salt residues), dried and subsequently stored on a dry, fresh parafilm in a small dish up to spring constant determination. One by one, the chips were mounted onto a well-calibrated closed-loop AFM scanner with the model number N9524A-69012 (Agilent Technologies / Keysight Technologies) equipped with an air-nose. Spring constant determination was performed in air and with an enabled z-closed-loop. As a clean solid surface was required, a freshly-cleaved pure mica sheet was chosen and clamped under the fluid cell for stabilization.

The laser spot was adjusted on the tip to be measured, the tip was approached to the surface and one force-distance cycle was recorded. Maximum indentation force and z-range were chosen in such a way that the linear part of the contact regime could clearly be identified. From this regime, the sensitivity could be determined (compare equation 1.2 on page 3). This step had to be performed anew for every tip as the sensitivity changes every time the laser spot on the cantilever backside is readjusted.

Next, the cantilever was retracted from the surface for about 200 µm and the software feature Thermal-K was started. This feature first determines the resonance behavior of the cantilever over the full accessible frequency range and then gives the option to choose the correct resonance peak. Here, the resonance peak that was best in line with the resonance frequency provided by the manufacturer was chosen. Spring constant calibration was done by recording the noise over the selected frequency range with an acquisition time of 3 s, averaging the acquired value over ten times. The shape of the tip (rectangular or triangular) was selected so the correct prefactor was used in the evaluation.

This entire procedure was repeated for all used cantilevers, as knowledge of the spring constant values is essential for correct data evaluation. The spring constants determined for all used cantilevers can be found in table A.1 in the appendix on page 78.

## 2.4. Data evaluation

Evaluation and curve fitting of all SMFS data was performed using MATLAB (Release 2013a, The MathWorks, Inc., Natick, Massachusetts, United States).

### 2.4.1. Evaluation of force-distance cycles

All force-distance cycles were analyzed using an in-house developed MATLAB program called *kspec*, short for german *Kraftspektroskopie* (force spectroscopy), version 1.9i, owned by Institute of Biophysics, Johannes Kepler University.

*Kspec* first loads in all force-distance curves files from one pulling rate (as outputted by PicoView 1.20/1.12) and extracts the curve data from the .mi files. It displays all curves one by one and provides a graphic user interface (GUI) tool for semi-automated curve fitting.

For every curve, the contact point needs to be selected and the rupture curve needs to be fitted. If possible, a second-order polynomial was fitted onto the rupture curve as this offers the best description

## 2. Materials and Methods

---

of the behavior expected from the elastic stretching of a flexible PEG-linker (compare section 1.3.4). Only if the noise or another artifact distorted the curve in a way that made it impossible to fit a second-order polynomial with the correct sign in curvature, a first-order polynomial was fitted. In figure 2.3, three out of four of the most important parameters extracted from one single force-distance cycle are indicated by colored arrows: The rupture force  $F_i$  is extracted as the force difference between the lowest point of the rupture curve and the baseline (red arrow). The unbinding length is the distance of the rupture point from the contact point (green arrow). The noise amplitude (blue arrow) gives the measurement error or standard deviation  $s_i$ . Additionally, the effective spring constant  $k_{eff}$  is extracted from the slope immediately before the rupture point.

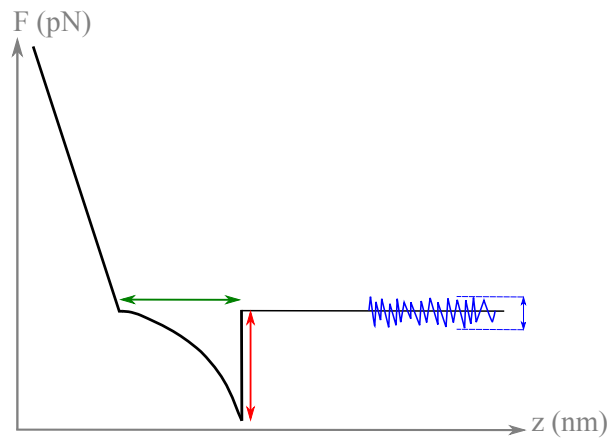


Figure 2.3.: Information extracted from a force-distance curve. The unbinding force is determined by the force difference between the rupture point and the baseline (red arrow), the unbinding length is given by the distance between the contact and the rupture points (green arrow). From the thermal noise (blue), the standard deviation of the unbinding force is calculated (blue arrow). Additionally, the effective spring constant is given by the slope immediately before the rupture event.

### 2.4.2. Distribution of curve parameters

After extraction of the four characteristic parameters from every curve in a given dataset, their distributions were calculated as probability density functions. The distribution of unbinding forces was calculated by formula (1.10), using the unbinding forces as  $F_i$  and the standard errors of the force extracted from the noise as  $s_i$ . As the standard deviations of the unbinding lengths and effective spring constants are not directly experimentally accessible like the standard deviations of the rupture forces, the respective distributions are estimated using the MATLAB built-in function *ksdensity*. This function estimates the probability density function for a given dataset.

### 2.4.3. Pulling-rate-grouped and most-likelihood fitting

Using an established fitting framework developed by Institute of Biophysics, Johannes Kepler University, fitting was performed for most-likely rupture forces calculated from the curve data grouped by their pulling rate. For each recorded pulling rate, a most-likely force and errors in both coordinates (force  $F$  and loading rate  $r$ ) were calculated. Fitting was then performed for these most-likely rupture forces with their respective errors. For details on this procedure, see Rankl et al. (2007) [30].

Using another formerly established fitting framework developed by Institute of Biophysics, Johannes Kepler University, the acquired data was evaluated by a method relying on a maximum-likelihood estimation. This framework performs fitting over all individual datapoints, without grouping them.

### 2.4.4. Loading-rate binning and population-wise fitting

Another evaluation approach performed for this thesis included binning of the data collected from all DFS experiments with respect to the loading rate and identifying individual populations within the data. Similar procedures have been applied elsewhere, for example by Rico & Moy (2007) [20], Carvalho et al. (2010) [22] or Hane et al. (2014) [21].

As the semilogarithmic representation (linear rupture force plotted towards the logarithmic loading rate) is generally preferred for DFS data evaluation, the data was divided into segments that would have equal length in the semilogarithmic plot. A MATLAB-based framework was developed that allows to define the number of bins per decade, sorting all data in a loading rate range stretching over one decade into  $N$  segments with apparently equidistant boundaries. Bins containing less than a minimum amount of datapoints were excluded from further evaluation. After binning the data, a weighted mean value and standard deviation were calculated for the rupture force data within each bin. For this purpose, the weights of all original datapoints  $F_i$  were calculated from their respective standard deviations  $s_i$  (extracted from the noise of the force distance curve) as

$$w_i = \frac{1}{s_i^2}. \quad (2.1)$$

The weighted mean rupture force of each bin was then projected onto the apparent center value of each bin with a lower boundary at a loading rate *lower* and an upper boundary at a loading rate *upper*, calculated as

$$\text{center} = 10^{(\log_{10}(\text{lower}) + \log_{10}(\text{upper})) / 2} \quad (2.2)$$

with the weighted standard deviations as error bars. Subsequently, mean rupture force fitting (see section 2.4.6 below) was then performed for these mean values.

## 2. Materials and Methods

---

For the collected datapoints within each bin, a probability density function was calculated. This can be done by using equation (1.10), performing the summation over all datapoints of the respective segment. Alternatively, using the MATLAB built-in function *ksdensity* yields a smoother distribution curve. The two variants will be compared in the results section.

The data collected for the interaction study on CRP and anti-CRP was grouped into five bins per decade (the same number of bins for every decade of the loading rate) and only bins with a minimum of twenty datapoints were used in the further analysis. The force distribution function was recalculated for the datapoints within each individual bin and subsequently, two Gaussian function were fitted onto the force distribution of each bin.

Subsequently, the mean values and standard deviations of the Gaussian curves were projected onto the apparent center positions of each bin and used for fitting.

### 2.4.5. Weighting of individual datapoints, bins and populations

For fitting of individual datapoints (mean rupture forces extracted from the force-distance cycles), all points were weighted with their respective standard deviations  $s_i$  (extracted from the noise of the force distance curve, see figure 2.3) with a weight

$$w_i = \frac{1}{s_i^2}. \quad (2.3)$$

For fitting the mean values obtained for each bin after performing binning with respect to the loading rate, the weight was calculated from the standard error of the mean  $s_{im}^2$ . The standard error of the mean  $s_{im}^2$  is given by the ratio of the weighted standard deviation  $s_i^2$  of each bin and the square root of the number  $n$  of datapoints within this bin according to

$$s_{im} = \frac{s_i}{\sqrt{n}} \quad (2.4)$$

leading to bin-wise weights

$$w_i = \frac{1}{s_{im}^2}. \quad (2.5)$$

A similar procedure was used for fitting the populations extracted from the individual bins. However, here  $s_i$  was taken as the standard deviation of the Gaussian fit of the respective population of each bin. When fitting Gaussian functions onto the force distributions calculated for the datapoints within one bin, one creates a new probability density function only comprising a sum of these Gaussian functions, normalized to a total area of one.

Figure 2.4 shows an example for this procedure. The original force distribution is shown in blue, the new one in red. The underlying Gaussian functions are shown in red dashed lines.

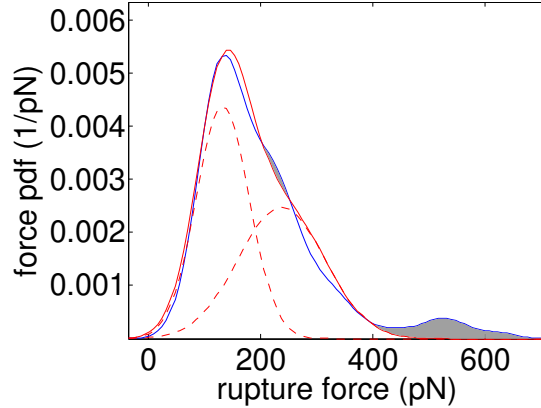


Figure 2.4.: Example for fitting two Gaussians onto a force PDF. Blue: Original PDF. Red solid: New PDF, calculated as the normalized sum of two Gaussian functions. Red dashed: Two Gaussian functions, interpreted as two populations within the data. The grey area is included in the old (blue) PDF, but not covered by the new (red) PDF.

Further, the number of datapoints  $n_i$  belonging to one population had to be estimated. This was achieved in two steps. First, the number of datapoints not accounted for by the fitted Gaussian functions was excluded. Therefore, outliers (datapoints at higher forces) were effectively disregarded. To estimate the number of datapoints that went unaccounted for by the new force distribution, the area covered by the old, but not by the new distribution function was calculated numerically. In figure 2.4, this area  $A_{ex}$  is shown in grey.

The total number of datapoints accounted for by the new distribution function is then given by

$$n_{new} = n \cdot (1 - A_{ex}) \quad (2.6)$$

with  $n$  denoting the original total number of datapoints in the bin. The remaining datapoints  $n_{new}$  are then divided among the identified populations according to the areas  $A_i$  of their respective Gaussian functions:

$$n_i = n_{new} \cdot A_i \quad (2.7)$$

Note that  $\sum_i A_i = 1$  for summation over all populations in one bin. With  $n_i$ , the standard error of the mean can be calculated for population  $i$

$$s_{im} = \frac{s_i}{\sqrt{n_i}} \quad (2.8)$$

and the weight  $w_i$  in a following fitting procedure can be calculated using equation (2.5).

## 2. Materials and Methods

---

### 2.4.6. Mean rupture force fitting

Mean rupture force fitting for Bell-Evans model was performed using the formula (derived from equation (1.38) for  $\mu = 1$ )

$$\langle F \rangle = F_\beta \left[ \ln \left( \frac{r}{F_\beta k_{off}} \right) - \gamma \right] \quad (2.9)$$

with

$$F_\beta = \frac{k_B T}{x_\beta}. \quad (2.10)$$

For Friddle model, fitting was performed with equation

$$\langle F \rangle = F_{eq} + F_\beta \ln \left( 1 + \frac{r}{F_\beta k_{off}} \exp \left[ -\gamma - \frac{F_{eq}}{F_\beta} \right] \right) \quad (2.11)$$

which is derived from equation (1.45) by neglecting the term  $\frac{k}{2} \frac{k_B T}{F_\beta^2}$ . Neglecting this term is justified due to its dependence on the quadratic factor  $1/F_\beta^2$ , letting it become very small very fast. This simplification is valid under the following condition

$$\frac{F_{eq}}{F_\beta} > \frac{k}{2} \frac{k_B T}{F_\beta^2} \quad (2.12)$$

which for  $x_\beta > 0$  can be rearranged to

$$\frac{2F_{eq}}{k} > x_\beta. \quad (2.13)$$

Inserting for  $F_{eq}$  the minimum recorded force  $F_{min}$  of the interaction study on CRP and anti-CRP and for  $k$  the maximum effective spring constant  $k_{eff,max}$  gives

$$\frac{2F_{min}}{k_{eff,max}} = \frac{2 * 21.45 \text{ pN}}{50.42 \text{ pN/nm}} \approx 8.5 \text{ Å} > x_\beta. \quad (2.14)$$

As will become evident in the results section, this condition is easily fulfilled for all evaluation strategies.

Analogously, Friddle fitting for multiple bonds was performed using the equation

$$\langle F \rangle = F_{eq} + NF_\beta \ln \left( 1 + \frac{r}{NF_\beta k_{off}} \exp \left[ -\gamma - \frac{F_{eq}}{NF_\beta} \right] \right). \quad (2.15)$$

This model was used for fitting of higher populations identified via loading-rate-wise binning and Gaussian-fitting.

#### 2.4.7. Fitting specifications and quality assessment

All customary curve fitting regarding the evaluation of loading rate dependence (Bell-Evans, Friddle) was performed using the nonlinear least-squares fitting method provided by MATLAB Curve Fitting Toolbox. [31]

When fitting a model function to a given dataset, the goal is to find function parameters leading to the best possible description of the data by the selected model. This is achieved by choosing an additional function that quantifies how closely the model matches the data and then varying the parameters until this function is minimized. The most common approach is based on minimizing the squared difference between the model values and the data and is therefore referred to as least-squares method. The model parameters are varied in small steps in an iterative processes until a minimum is found. [32] Curve fitting tool box uses a matrix method to realize this algorithm for nonlinear functions.

For the fitting of mean rupture forces versus loading rate, the Trust-region fitting algorithm was used. This algorithm allows to define constraints for the model parameters, which makes sense as the parameters  $k_{off}$ ,  $F_\beta$  and  $F_{eq}$  can only assume positive values. [31]

Once a fitting procedure has been applied to a given dataset and convergence has been reached, the quality of the fit can be assessed by a number of parameters. One of them is  $R^2$  or the *goodness-of-fit*, which describes how well the model correlates to the data.  $R^2$  is calculated as the sum of variations around the mean attributed to the model divided by the sum of total variations around the mean and can assume values from 0 to 1. The closer  $R^2$  is to 1, the better the match. [32], [33]

Another way to judge the quality of a fit is based on assessing the function parameters' standard errors. The smaller these errors, the better the fit, as a small error means that the overall fitting result would be far more off for a small deviation from the optimized parameter. Standard errors are connected to another frequently used indicator, the confidence interval, calculated individually for every function parameter. Typically, a confidence interval is calculated for a certain percentage and indicates that the correct value lies within its boundaries with a certainty given by the chosen percentage. [32] MATLAB Curve Fitting Toolbox provides a 95 % confidence interval for every fitting parameter.

## 3. Results and Discussion

### 3.1. Imaging and scratch experiments

Mica was used as a support for all CRP-samples. Figure 3.1 shows a contact mode image of a freshly-cleaved mica sheet suspended in purified water.

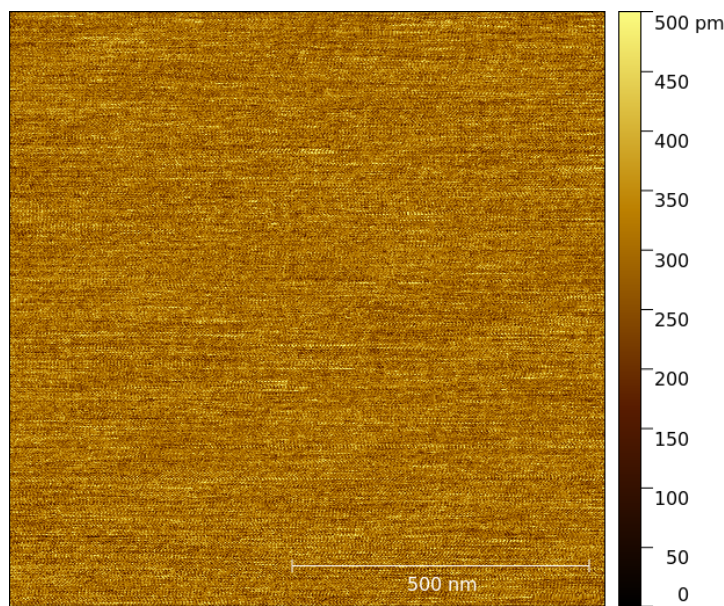


Figure 3.1.: Mica in  $\text{H}_2\text{O}$ , imaged in contact mode

As described in section 2.2.2, mica was coated with APTES for aminofunctionalization. Figure 3.2 shows a contact mode image of mica with APTES. In a scratch experiment, it could be demonstrated that mica is indeed covered in APTES as the APTES layer can be pushed away when applying enough. The result is shown in figure 3.3. In the rectangular-shaped area, APTES was scratched away.

### 3.1. Imaging and scratch experiments

---

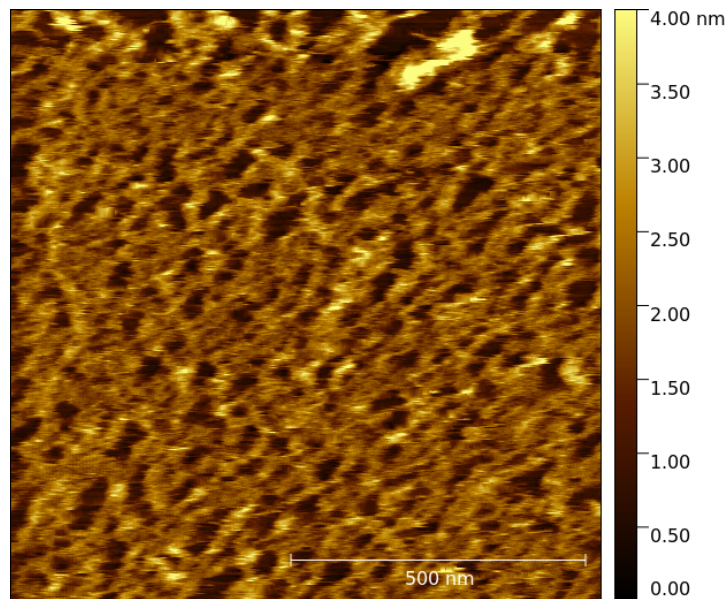


Figure 3.2.: APTES-coated mica in PBS, imaged in contact mode

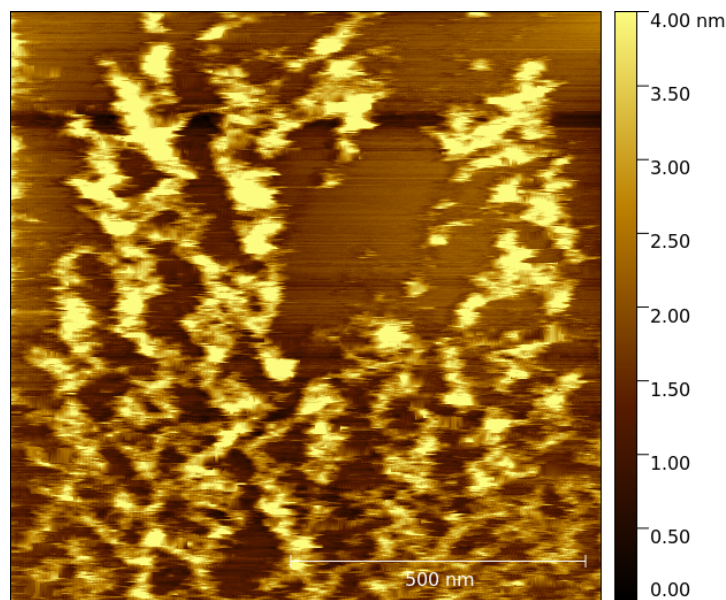


Figure 3.3.: APTES-coated mica, suspended in PBS, scratch experiment, imaged in contact mode

After APTES-coating, the support was functionalized with EGS. Again, imaging in contact mode and a scratch experiment were performed following this intermediate step. The results are shown in figures 3.4 and 3.5, respectively. Figure 3.5 shows a flat, rectangular area becoming visible upon performing

### 3. Results and Discussion

---

the scratch, indicating that coverage with EGS was achieved.

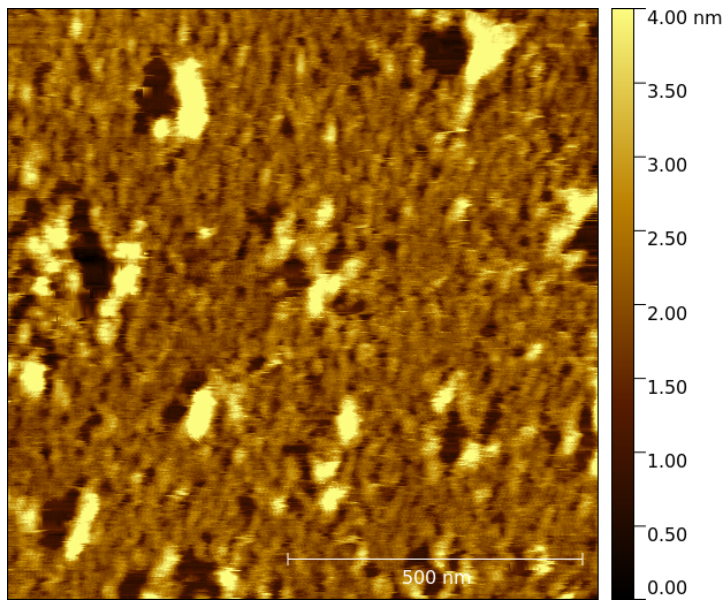


Figure 3.4.: APTES-coated mica functionalized with EGS, suspended in PBS, imaged in contact mode

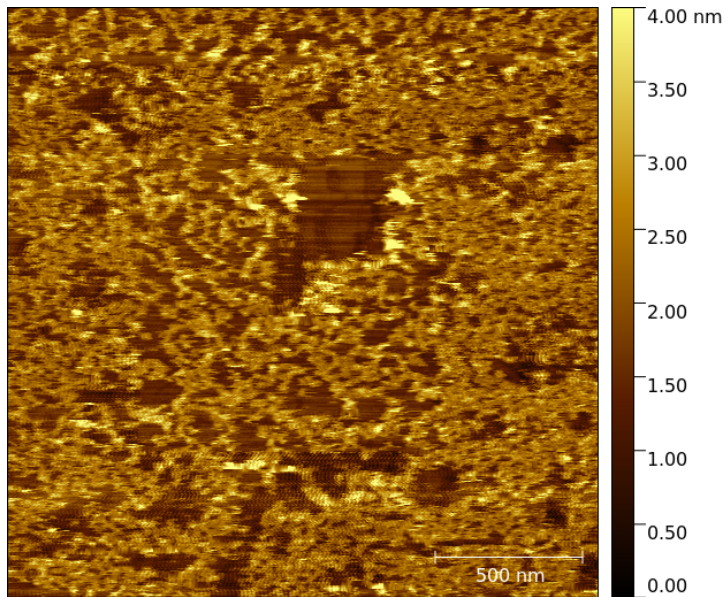


Figure 3.5.: APTES-coated mica functionalized with EGS, suspended in PBS, imaged in contact mode

Finally, the APTES- and EGS-coated mica surface was functionalized with CRP. Again, the sample was imaged and a scratch was performed, the results can be seen in figures 3.6 and 3.7.

### 3.1. Imaging and scratch experiments

---

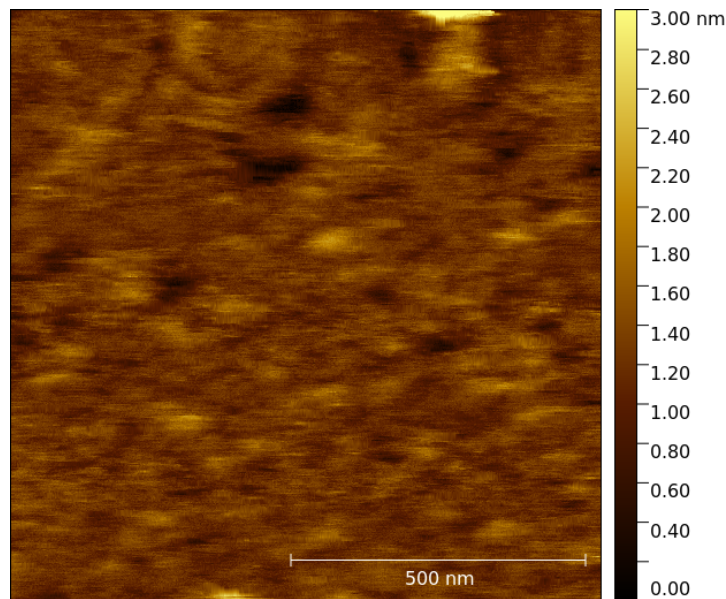


Figure 3.6.: Mica functionalized with CRP, suspended in PBS, imaged in contact mode

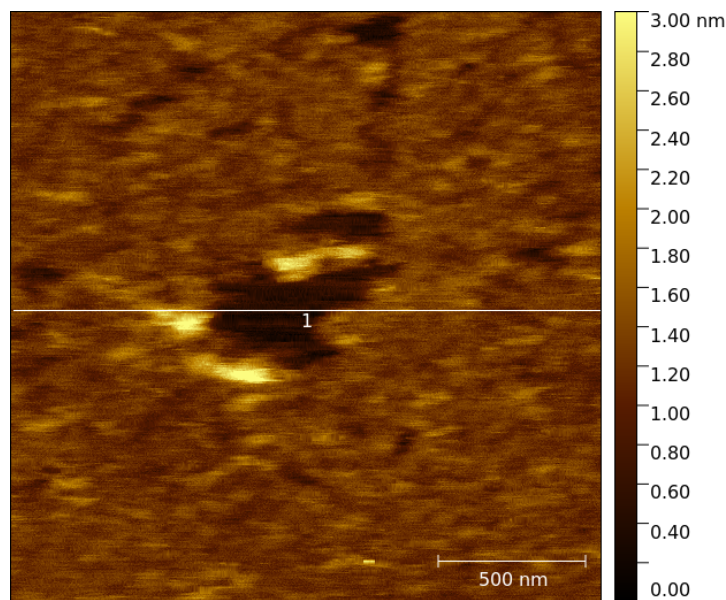


Figure 3.7.: Mica functionalized with CRP, scratch experiment, suspended in PBS, imaged in contact mode

The profile highlighted with a white line in figure 3.7 was analyzed with regard to the height difference between the inner segment (where the protein was scratched off) and the CRP-covered segments to the left and right of the hole.

### 3. Results and Discussion

---

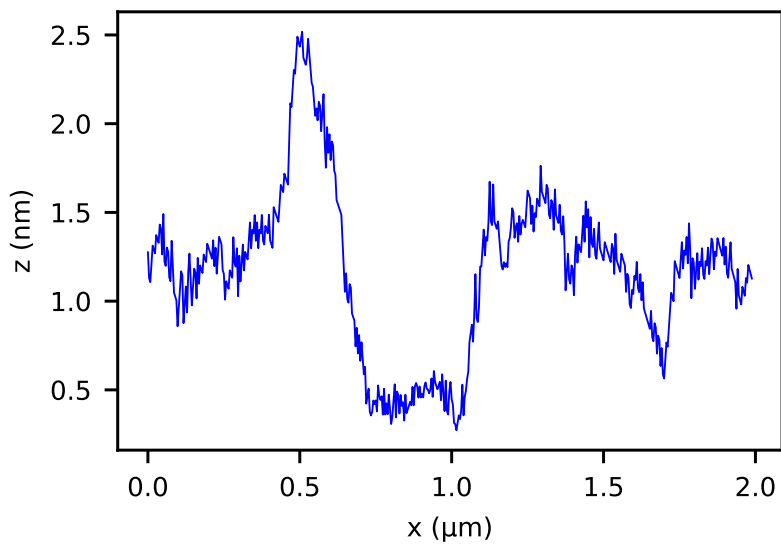


Figure 3.8.: Height profile of the line highlighted in figure 3.7

An analysis of the profile, disregarding the segments immediately before and after the cavity, where protein has been piled up, showed that the average height difference  $\Delta z$  between the lower and the upper level amounts to:

$$\Delta z = (0.72 \pm 0.19) \text{ nm}$$

This height difference is rather low. However, CRP is bound to mica via a flexible EGS-crosslinker. As all imaging was performed in contact mode, it is possible that the pressure inflicted upon the sample by the probe tip squeezed the protein down or pushed it side-wards, resulting in an apparently lower height.

In any case, as can also be seen in figure 3.7 and the profile in figure 3.8, the area where the scratch was performed appears rather flat, indicating that most molecules have been pushed out of this region and the sample was successfully covered in CRP.

## 3.2. SMFS measurements

### 3.2.1. Binding probabilities

In table 3.1, *rate* refers to the pulling rate and *total* gives the total number of force-distance cycles recorded for this particular pulling rate. The binding probability was calculated as the percentage of curves that showed a binding event. The hold time defines the time over which the tip is in contact with the surface. The maximum hold time (*maxht*) was varied for each pulling rate to achieve the best binding probability.

Table 3.1.: Binding probabilities of SMFS performed studying the interaction between CRP and anti-CRP

rate (μm/s)	max ht (s)	total	binding probability (%)
0.04	0	618	13.27
0.08	0	1905	4.51
0.2	0.3	1512	8.99
0.3	0.3	1291	10.92
0.6	0.3	4965	6.89
1	0.3	1486	4.10
1.2	0.3	1858	7.48
2.5	0.5	1224	5.64

The whole experiment, comprising functionalization of sample and tips as well as the actual SMFS measurements, were performed seven times. A complete overview on which pulling rate was recorded using which sample and tip is given in table A.1 in the appendix on page 78.

### 3.2.2. Distributions

Figure 3.9 shows exemplary results of one SMFS experiment performed with a pulling rate of 0.6 μm/s for 4965 times, yielding a binding probability of 6.89 %. The four plots show the rupture force distribution as calculated by formula (1.10), probability density functions estimated for the effective spring constants and unbinding lengths as well as a comparison of unbinding forces and lengths. The collected results for all pulling rates are given in appendix A starting from page 79.

### 3. Results and Discussion

---

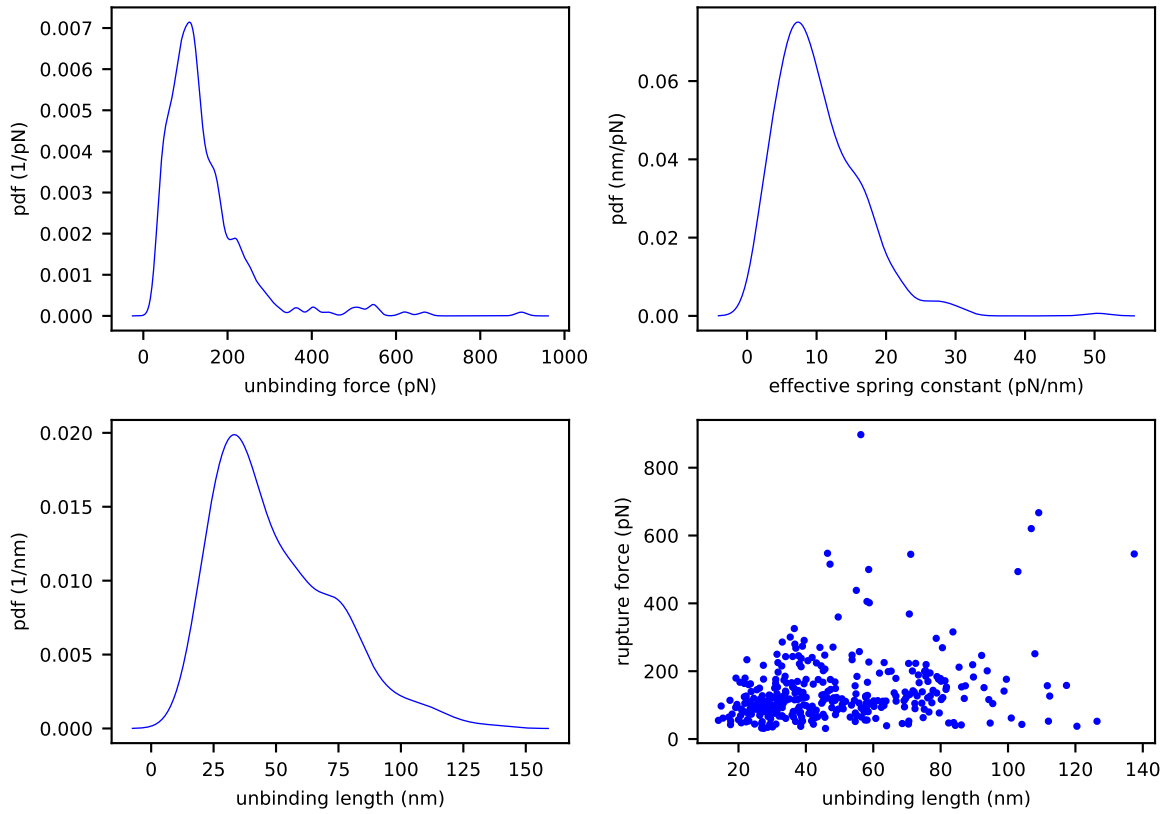


Figure 3.9.: Unbinding force distribution, effective spring constant distribution, unbinding length distribution and comparison of unbinding force and unbinding length, acquired for a pulling rate of  $0.6 \mu\text{m/s}$  and a maximum hold time of  $0.3 \text{s}$ , total number of curves: 4965, binding probability: 6.89 %

#### 3.2.3. Block experiments

Altogether, three block experiments were performed during the interaction study on CRP and anti-CRP. Two of them were performed with leftover CRP collected from the droplet after tip functionalization (maximum possible concentration  $1.16 \mu\text{g/ml}$ ), the third one with a fresh portion of CRP (giving  $1.33 \mu\text{g/ml}$ ).

For two out of three block experiments, a decrease in binding probability could be observed. A block experiment is considered successful when the binding probability could be reduced considerably upon adding the blocking agent, in this case free CRP. In this sense, block number one (see table 3.2) and three (see table 3.4) were successful, while block number two (see table 3.3) was not.

Table 3.2.: 1st block experiment, performed at a pulling rate of  $1\text{ }\mu\text{m/s}$  with a maximum hold time of  $0.3\text{ s}$  upon adding  $1.16\text{ }\mu\text{g/ml CRP}$

	total	binding probability (%)
original	1486	4.10
block	2097	1.57
recovery	1537	4.42

Table 3.3.: 2nd block experiment, performed at a pulling rate of  $0.6\text{ }\mu\text{m/s}$  with a maximum hold time of  $0.3\text{ s}$  upon adding  $1.16\text{ }\mu\text{g/ml CRP}$

	total	binding probability (%)
original	2271	12.36
block	2306	11.49

Table 3.4.: 3rd block experiment, performed at a pulling rate of  $0.2\text{ }\mu\text{m/s}$  with a maximum hold time of  $0.3\text{ s}$  upon adding  $1.33\text{ }\mu\text{g/ml CRP}$

	total	binding probability (%)
original	1512	8.99
block	1503	0.60

For block experiment number one, the binding probability prior to the block was already very low. However, upon adding free CRP it could be reduced by about 60 %. Additionally, after thorough rinsing of the sample and the cantilever in PBS and performing another measurement, the original binding probability could be recovered to a level very close to the original one.

Figure 3.10 shows an overlay of the unbinding force distributions before (*Original*) and after the block (*Block*). Figure 3.11 shows an overlay of the distributions of unbinding forces recorded before the block (*Original*) and after rinsing of sample and cantilever (*Recovery*).

As can be seen in figure 3.10, before the block the distribution shows a double-peak at about  $100\text{ pN}$  (at  $91.7\text{ pN}/125.2\text{ pN}$ ) and one peak at  $237.6\text{ pN}$ . After the block, there are corresponding peaks at  $147.1\text{ pN}$  and  $257.6\text{ pN}$ , with the second one showing a decrease in height. This could mean that there are two kinds of interactions present, either due to double-bindings of one antibody to the CRP-covered surface or to two separate linkers being attached to the tip. In either case, only one type

### 3. Results and Discussion

---

of interaction seems affected by the blocking agent, which could either mean that only one interaction is specific or, if there were two linkers, that only one antibody had a blocking CRP-molecule bound.

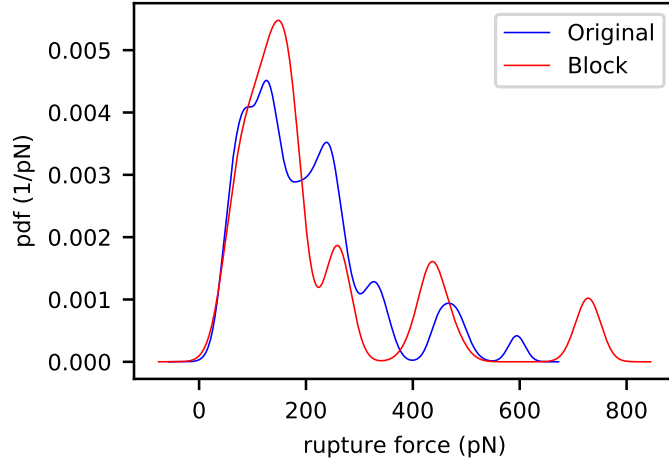


Figure 3.10.: Force distributions acquired for a pulling rate of 1  $\mu\text{m}/\text{s}$  and maximum hold time of 0.3 s, original (unblocked, in PBS, 1486 curves recorded, binding probability 4.10 %) and blocked (with 1.16  $\mu\text{g}/\text{ml}$  free CRP in PBS, 2097 curves recorded, binding probability 1.57 %)

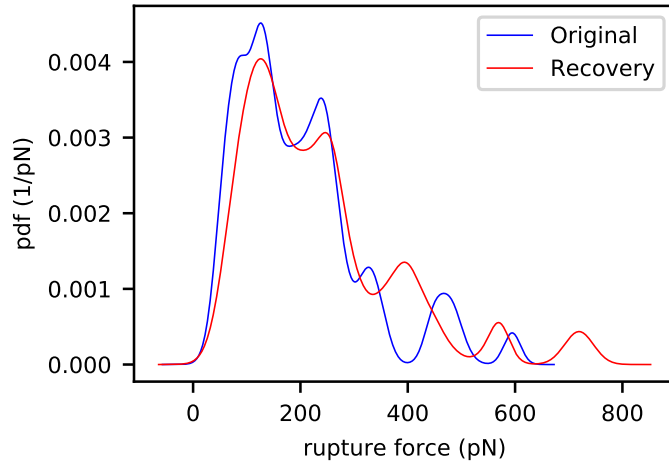


Figure 3.11.: Force distributions acquired for a pulling rate of 1  $\mu\text{m}/\text{s}$  and maximum hold time of 0.3 s, original (1486 curves recorded, binding probability 4.10 %) and recovery (1537 curves recorded, binding probability 4.42 %)

Both possibilities can be reconciled with the finding shown in figure 3.11. The distribution curve of the recovered measurement shows two dominant peaks, at 124.6 pN and 245.6 pN. The overlay of rupture

force distributions of the original and the recovered measurement shows that the second individual peak can partly be recovered as the two distributions have a similar shape.

However, the results are clearly not definite, mainly due to the overall low number of bindings. A higher total number of bindings would give smoother distribution curves and would make it easier to draw conclusions.

Block number two was clearly unsuccessful as the binding probability could not be reduced. However, as this block was also performed with CRP leftover from tip functionalization, the concentration may have been lower than estimated or the CRP may have deteriorated during storage.

Figure 3.12 shows the original and blocked force distributions calculated for the third block experiment. This block experiment showed the most pronounced decrease in binding probability. Altogether nine bindings were recorded, their rupture force values stretching over almost the whole range of the original force distribution. However, due to the overall low number, no further conclusions can be drawn from this.

A recovery experiment was attempted after rinsing the sample and storing it in fresh PBS over a weekend, but the measurement aborted as no bindings were detected. As this could easily be caused by the deterioration of the sample and/or tip over time, this finding is not necessarily a contradiction to the success of the block.

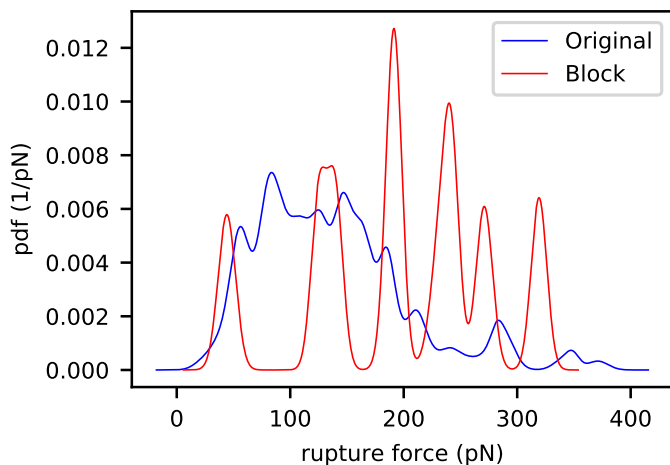


Figure 3.12.: Force distributions acquired for a pulling rate of  $0.2 \mu\text{m}/\text{s}$  and maximum hold time of  $0.3 \text{ s}$ , original (unblocked, in PBS, 1512 curves recorded, binding probability 8.99 %) and blocked (with  $1.33 \mu\text{g}/\text{ml}$  free CRP in PBS, 1503 curves recorded, binding probability 0.60 %)

### 3.3. CRP and anti-CRP interaction study evaluation

#### 3.3.1. Collected DFS results

The unbinding forces recorded for the eight pulling rates listed in table 3.1 were further processed by calculating the respective loading rates for every datapoint as the product of effective spring constant and pulling rate (see equation (1.26)). The collected results are shown in figure 3.13.

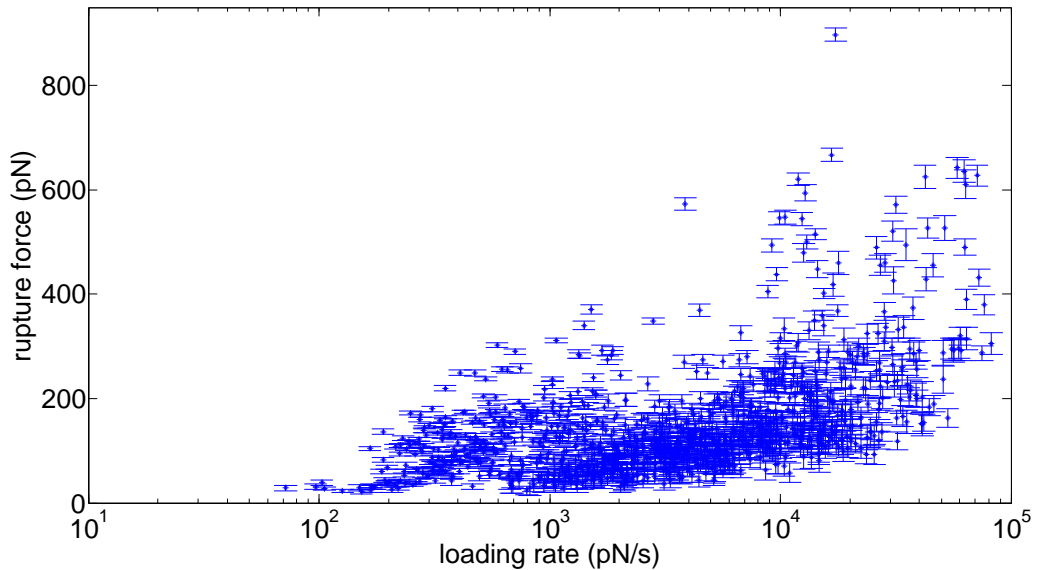


Figure 3.13.: Rupture force data recorded for studying the interaction of CRP and anti-CRP. Collected from eight distinct pulling rates and plotted towards the loading rate. Error bars give the standard deviation of the individual datapoints. 1055 datapoints in total.

In the following, different evaluation approaches for this dataset will be compared.

#### 3.3.2. Grouping by pulling rate

A frequently used method relies on grouping of the data by the recorded pulling rate. For each pulling rate, a most-likely rupture force and error bars in both coordinates (force and loading rate) are calculated. The result of grouping the data in this way and performing and a Bell-Evans fit for the most-likely rupture force are shown in figure 3.14.

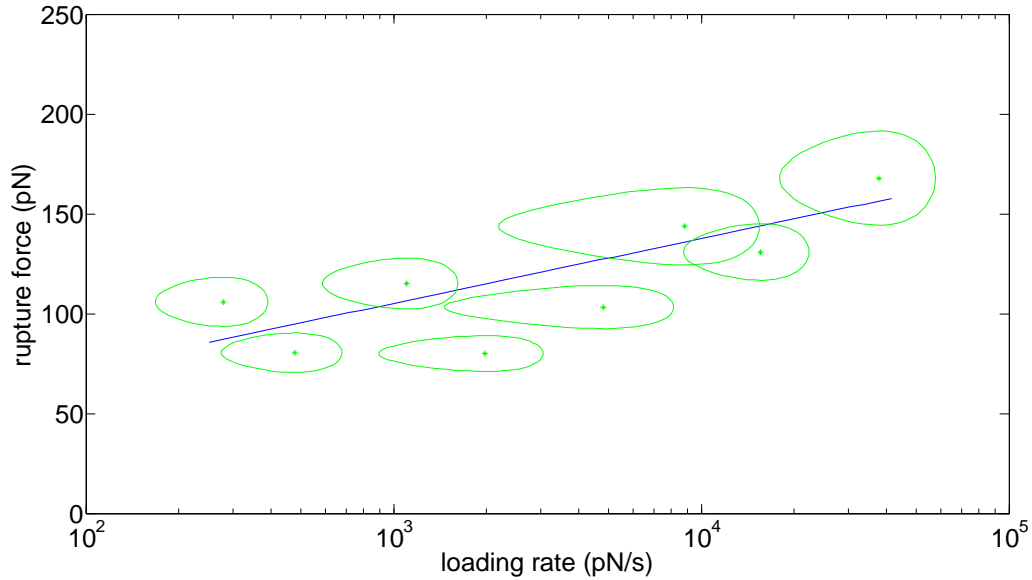


Figure 3.14.: Green: DFS data grouped by pulling rate, most-likely force and standard deviations in both coordinates indicated by the ovals. Blue: Bell-Evans fit of most-likely rupture force. Fit results:  $x_\beta = (2.91 \pm 0.78) \text{ \AA}$ ,  $k_{off} = (0.04 \pm 0.08) \text{ s}^{-1}$

This fitting method does not seem like a good choice. As datapoints recorded at the same pulling rate have different effective spring constants, the data can stretch over a wide range of loading rates. Grouping before the fitting procedure makes it harder to recognize the actual curve shape and find a good model to predict its trend.

### 3.3.3. Maximum-likelihood fit

Using the established maximum-likelihood fitting framework developed by the Institute of Biophysics, JKU, the acquired DFS data on the interaction study on CRP and anti-CRP was fitted with the models by Bell-Evans, Hummer-Szabo and Dudko. The results for Bell-Evans are shown in figure 3.15.

An optical examination shows that Bell-Evans fit does not appear to be a good choice for the data as it fails in predicting the overall shape of the data cloud.

For the models by Hummer-Szabo and Dudko, the fitting method could not calculate a final result with numeric standard errors and yielded Bayesian Information Criteria (BIC) of 11189 and 12563, respectively. The higher the BIC of a likelihood-fit, the lower is the goodness-of-fit. [34] Therefore, these two models were disregarded in the further analysis.

### 3. Results and Discussion

---

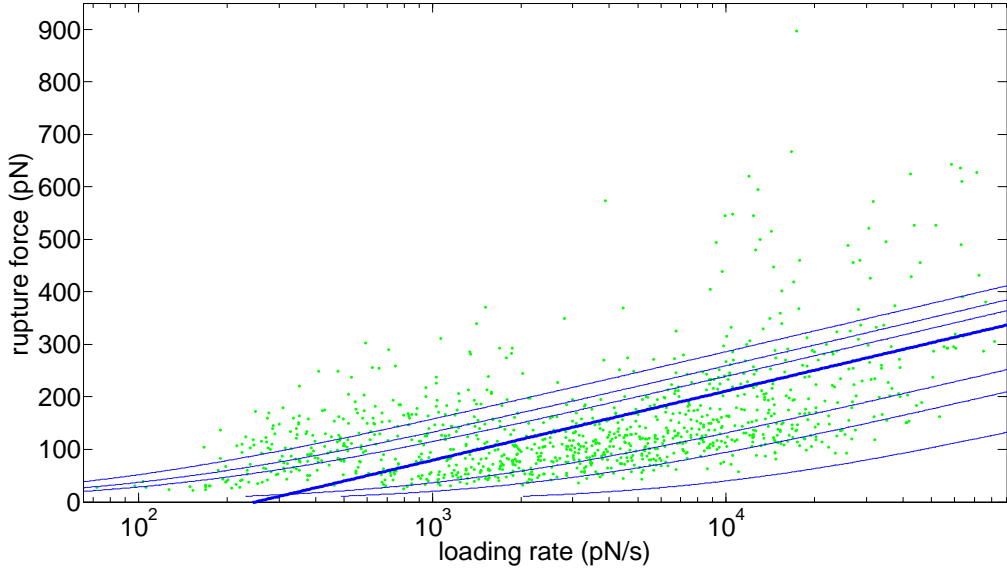


Figure 3.15.: Green: DFS data for the interaction study on CRP and anti-CRP. Blue thick solid line: Maximum-likelihood Bell-Evans fit of most-likely rupture force. Fit results:  $x_\beta = (0.719 \pm 0.015) \text{ \AA}$ ,  $k_{off} = (4.36 \pm 0.25) \text{ s}^{-1}$ , BIC=9816.4

#### 3.3.4. Loading rate binning

As established evaluation and fitting methods did not lead to conclusive results, an alternative approach was chosen for further analysis of the data collected for CRP and anti-CRP.

All in all, 1055 datapoints were collected. In the first stage in data processing, all datapoints with a unbinding length of more than 150 nm were disregarded. As the linker molecule has a finite length, this is justified. By this step, the number of datapoints was slightly reduced from 1055 to 1038.

Following this step, binning of the data was performed with respect to the loading rate as described in the Materials & Methods starting from section 2.4.4 onwards. In a first step, the data was binned in five segments per decade. All bins containing less than twenty datapoints were disregarded in the further analysis.

Force distributions as PDFs were recalculated for the datapoints in every used bin. This can be achieved by using formula (1.10) as suggested by Baumgartner et al. [10], performing a summation over the datapoints with their mean forces and standard deviations. There are alternative methods for estimating the PDF like the MATLAB-function *ksdensity*, which estimates the whole PDF instead of summing up only the present datapoints. Therefore, it yields a smoother curve, making the final result easier to fit with Gaussian functions. However, it does not take into account the datapoints' individual

errors. To determine which method is suitable, they were compared for each bin. The results can be seen in the appendix in figures B.1 to B.7. In all of these figures, the PDF calculated with formula (1.10) is given in red, the PDF calculated with *ksdensity* is blue.

Comparing the two types of PDFs shows that the higher the number of datapoints in the respective bin, the closer the match between the two curves. For bins like the last one (bin center 50 118.72 pN/s), the deviation is most pronounced. This might suggest that for bins with such low number of datapoints the estimation done by the MATLAB-function is no longer reliable. However, it was decided to use the PDFs calculated using *ksdensity* as they are more suitable for fitting Gaussian functions. Moreover, the bins for higher loading rates exhibit the broadest distribution functions, leading to the high standard deviations. Together with their low number of datapoints, the weighting scheme (discussed in section 2.4.5) will lead to these bins having a low overall influence on the final fitting results, making the error produced by keeping them rather small.

Figures 3.16 to 3.22 show the development of the force distributions calculated for all bins with more than twenty datapoints for increasing loading rates.

Two trends are clearly visible for the development of the force distributions. For once, the distributions for lower loading rates are quite similar with respect to their peak force and width. For higher loading rates, starting from around 6000 pN/s, the peak forces increase and the distributions show a clear broadening. This behaviour is best illustrated by an overlay as given in figure 3.23 and is well in accordance with theoretical expectations.

Second, in every force distribution there seems to be one dominant peak and a second, smaller peak at a higher force. This can be interpreted as a hint that there are two populations present.

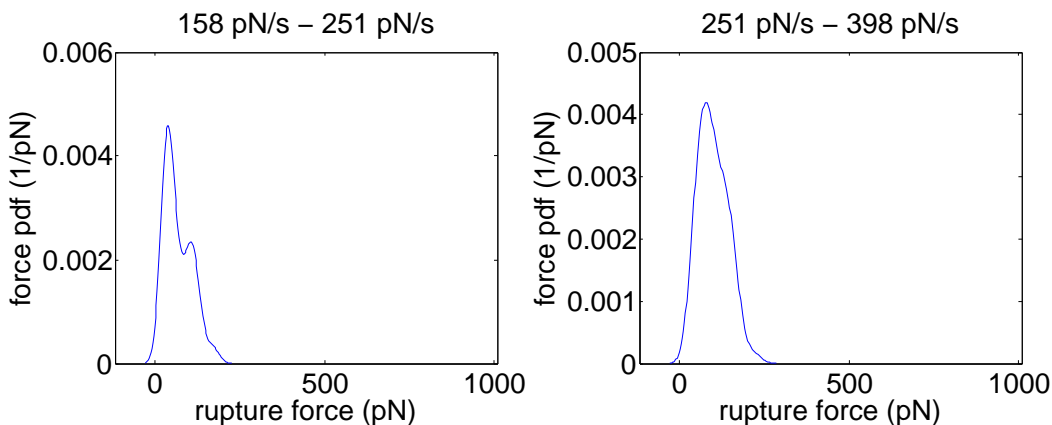


Figure 3.16.: Force PDF for 199.53 pN/s (31 datapoints) and 316.23 pN/s (63 datapoints)

### 3. Results and Discussion

---

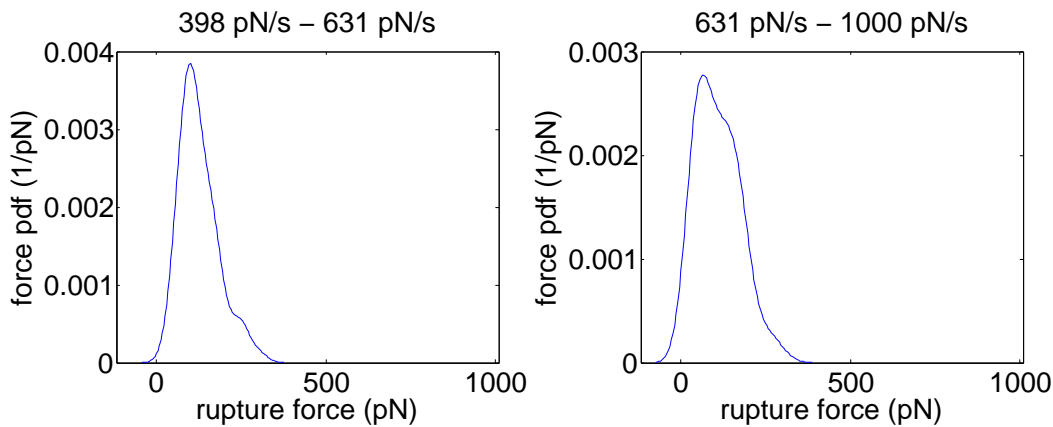


Figure 3.17.: Force PDF for 501.19 pN/s (64 datapoints) and 794.33 pN/s (72 datapoints)

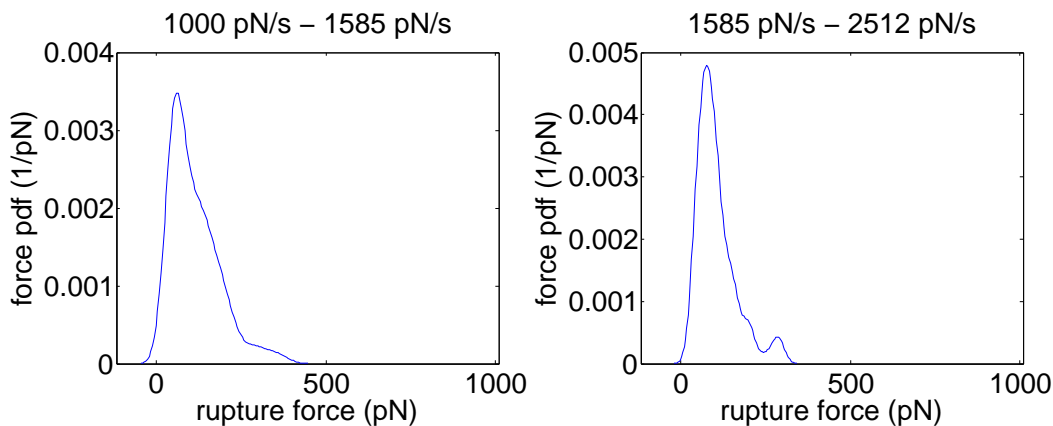


Figure 3.18.: Force PDF for 1258.93 pN/s (103 datapoints) and 1995.26 pN/s (101 datapoints)

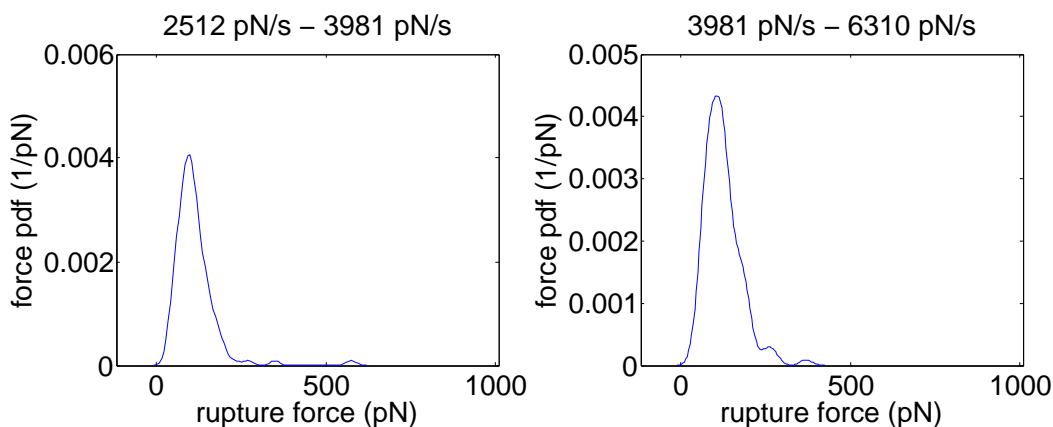


Figure 3.19.: Force PDF for 3162.28 pN/s (112 datapoints) and 5011.87 pN/s (118 datapoints)

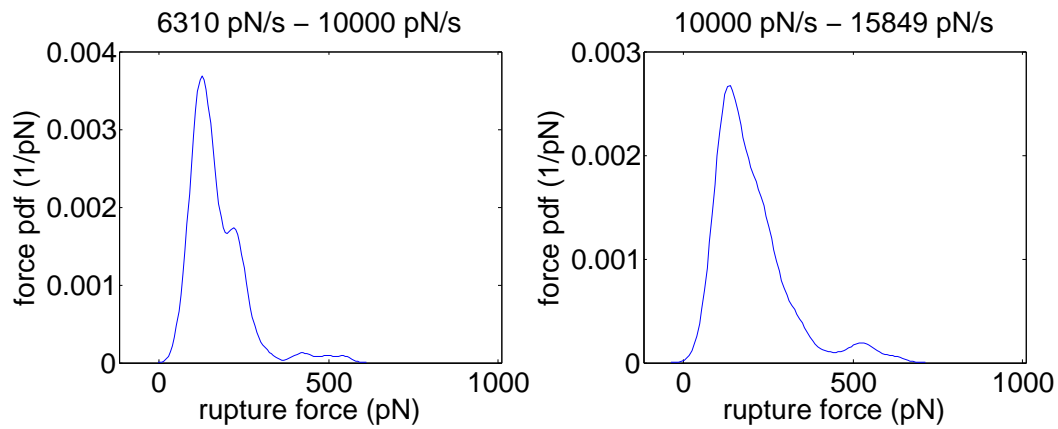


Figure 3.20.: Force PDF for 7943.28 pN/s (111 datapoints) and 12 589.25 pN/s (109 datapoints)

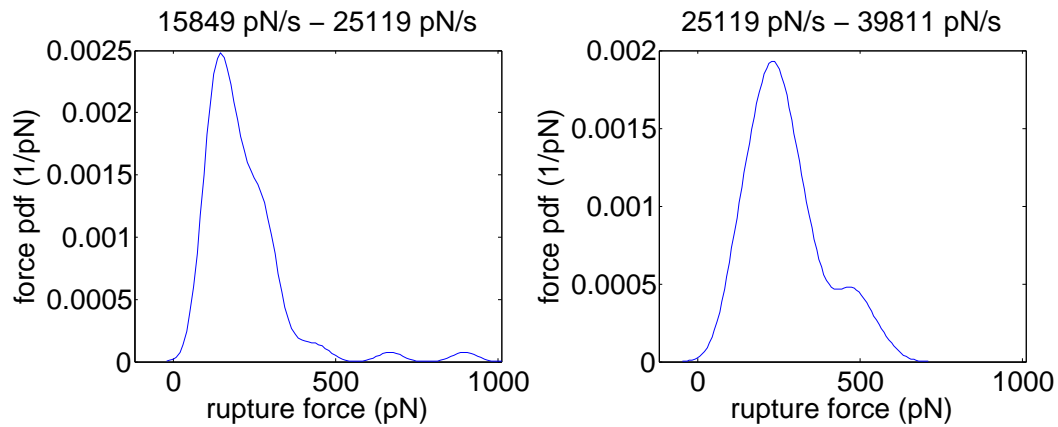


Figure 3.21.: Force PDF for 19 952.62 pN/s (69 datapoints) and 31 622.78 pN/s (47 datapoints)

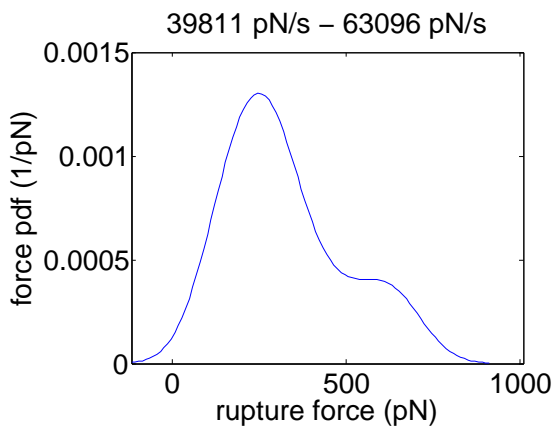


Figure 3.22.: Force PDF for 50 118.72 pN/s (22 datapoints)

### 3. Results and Discussion

---

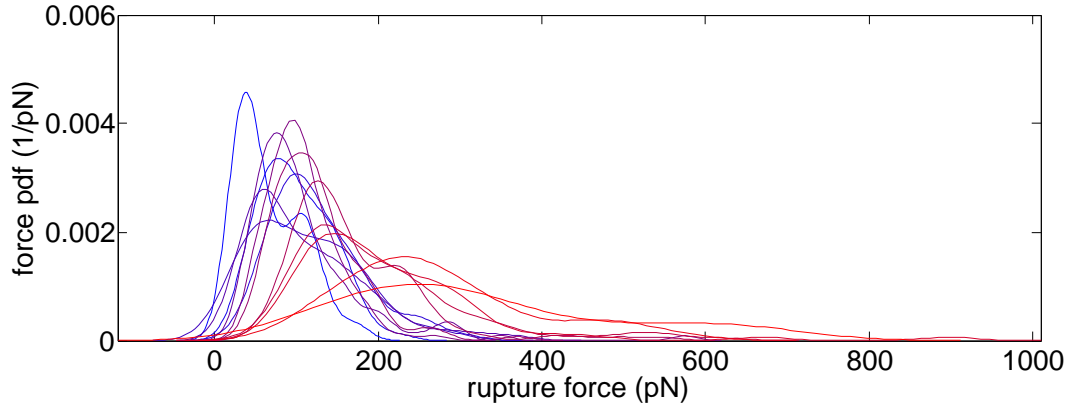


Figure 3.23.: Force distribution development for increasing loading rates (blue for lowest, red for highest loading-rate bin). Loading rate bin center points given in table 3.5.

Table 3.5.: CRP anti-CRP data binning results: Bin center refers to the apparent central loading rate of the bin, datapoints gives the number of datapoints within it (all bin with less than 20 datapoints were disregarded for further analysis).  $F_m$  gives the weighted mean rupture force of the bin,  $s_m$  its standard deviation.  $F^*$  gives the force at the maximum of the force distribution within the bin.

bin center (pN/s)	datapoints	$F_m$ (pN)	$s_m$ (pN)	$F^*$ (pN)
199.53	31	66.91	38.94	37.22
316.23	63	100.25	41.39	78.09
501.19	64	130.36	54.58	101.36
794.33	72	124.11	60.72	65.70
1258.93	103	141.19	76.74	58.60
1995.26	101	122.74	66.29	75.88
3162.28	112	121.66	76.56	98.10
5011.87	118	125.64	53.41	107.20
7943.28	111	170.51	81.35	126.31
12589.25	109	225.00	117.27	137.74
19952.62	69	237.66	158.72	146.59
31622.78	47	262.64	112.32	228.82
50118.72	22	306.66	154.42	246.09

### 3.3. CRP and anti-CRP interaction study evaluation

The entire binning result is shown in figure 3.24. Here, the data is given in blue and the bins are indicated by black vertical lines. For each bin, the weighted mean value and standard deviation are given in red (as datapoints with error bars). For comparison, the green datapoint gives the location of the maximum of the force distribution for the respective bin.

Table 3.5 shows the apparent central loading rates, number of datapoints, weighted mean values, standard deviations and most-likely forces (the maximum of the *ksdensity*-calculated force PDF) for all bins containing more than twenty datapoints.

As there appear to be two regimes - one of approximately constant force for lower loading rates and one of increasing mean force for higher loading rates - Friddle model was chosen for fitting the data. The results of the mean forces given in table 3.5 fitted with formula (2.11), weighted as described in section 2.4.5, is shown in figure 3.25.

For comparison, the original (not-binned) data was also fitted with Friddle model, as shown in figure 3.26.

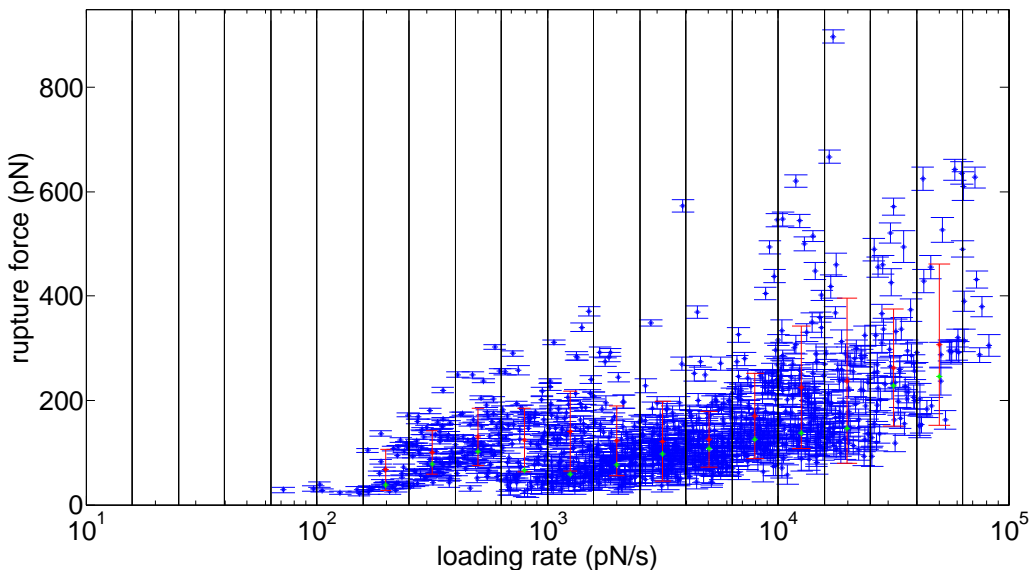


Figure 3.24.: Binning of the collected data recorded for CRP and anti-CRP into 5 bins per decade with a minimum of 20 datapoints per bin. Red point gives the weighted mean value of forces in the bin projected onto the apparent center point, red errorbars give the weighted standard deviations. Green points give the maximum of the rupture force distribution in the bin. The results are given in table 3.5.

### 3. Results and Discussion

---

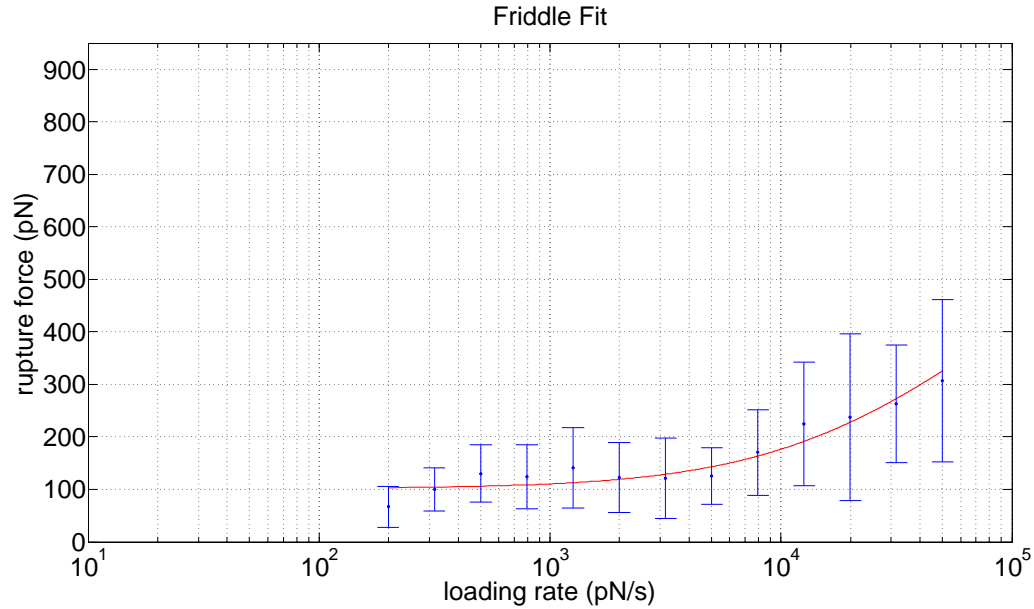


Figure 3.25.: Friddle fit of mean rupture forces calculated for the individual bins shown in figure 3.24. Fitting results with 95 % confidence intervals:  $F_{eq}=101.3 \text{ pN}$  [80.03, 122.5],  $F_\beta=165.4 \text{ pN}$  [-194.5, 525, 2],  $k_{off}=31.97 \text{ s}^{-1}$  [-39.48, 103.4].  $R^2 = 0.757$ .

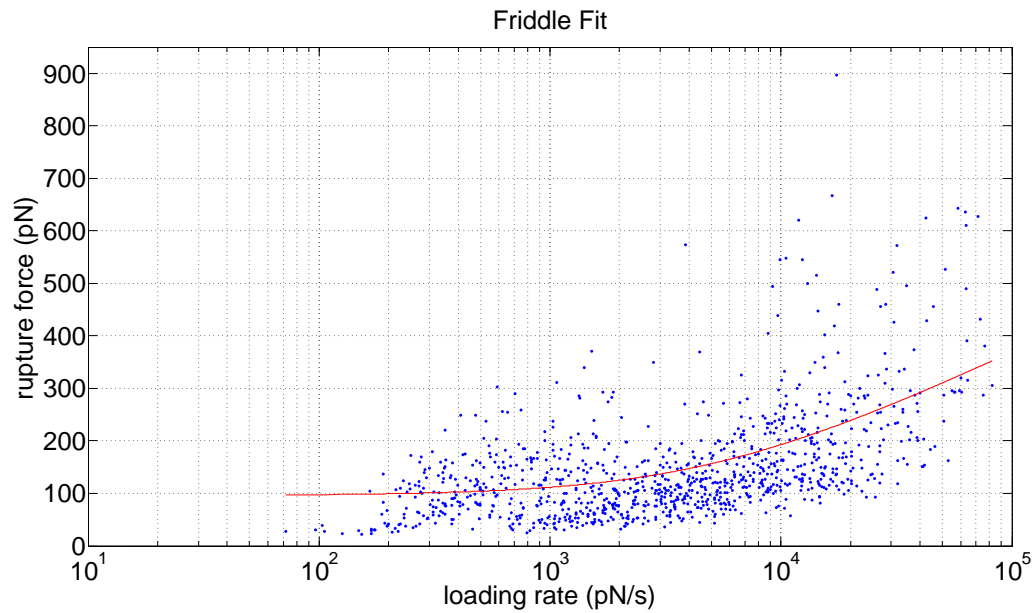


Figure 3.26.: Friddle fit for mean rupture forces of CRP and anti-CRP performed for 1038 individual datapoints. Fitting results with 95 % confidence intervals:  $F_{eq}=95.95 \text{ pN}$  [89.57, 102.3],  $F_\beta=91.51 \text{ pN}$  [50.98, 132],  $k_{off}=11.43 \text{ s}^{-1}$  [2.126, 20.73].  $R^2 = 0.2222$ .

Unsurprisingly, the  $R^2$  value calculated for fitting the individual datapoints is considerably lower than for fitting of the bin-wise mean values (0.222 versus 0.7570) because the datapoints spread over a wide range. However, interestingly the confidence intervals are considerably narrower for fitting of the not-binned data compared to the bin-wise mean forces.

### 3.3.5. Analysis of the higher loading rate regime

As described in section 1.4.3, Friddle model predicts a  $\ln(r)$ -dependence for higher loading rates. To check if Friddle model is indeed a good choice, this prediction was tested for the data on CRP and anti-CRP. As starting from around 6000 pN/s, the curve seems to enter the nonlinear regime, this part of the curve was analyzed separately with Bell-Evans model by fitting it with equation (2.9).

Figure 3.28 shows the result for fitting of individual datapoints (381 in total), figure 3.27 shows the fit for the bin-wise mean values (the last five bins as given in table 3.5).

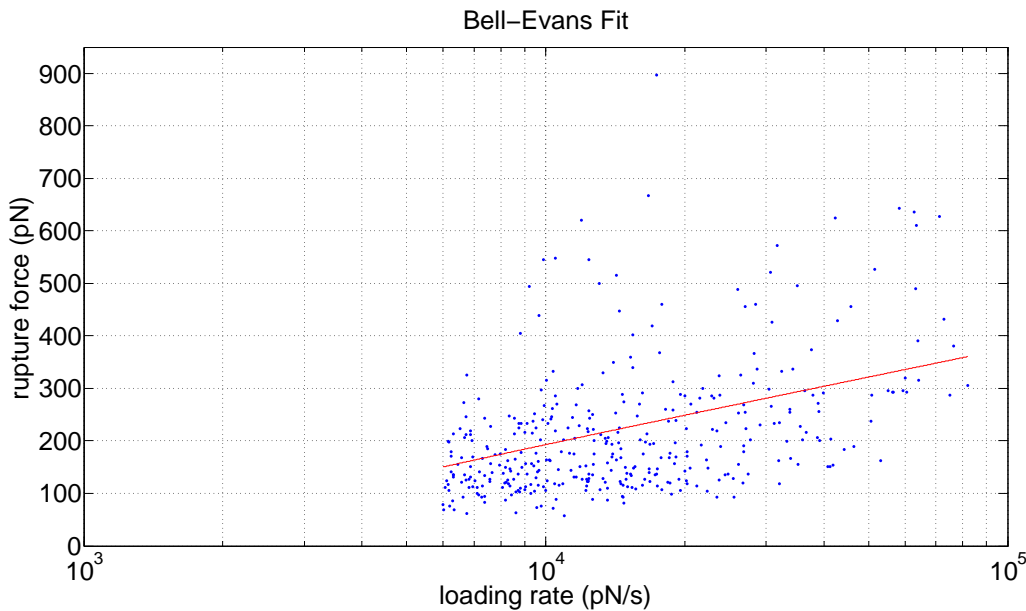


Figure 3.27.: Bell-Evans fit for mean rupture forces of CRP and anti-CRP performed for 381 individual datapoints for loading rates starting from 6000 pN/s. Fitting results with 95 % confidence intervals:  $F_\beta=78.1 \text{ pN}$  [60.54, 95.67],  $k_{off}=10.33 \text{ s}^{-1}$  [6.44, 14.23].  $R^2 = 0.1453$ .

### 3. Results and Discussion

---

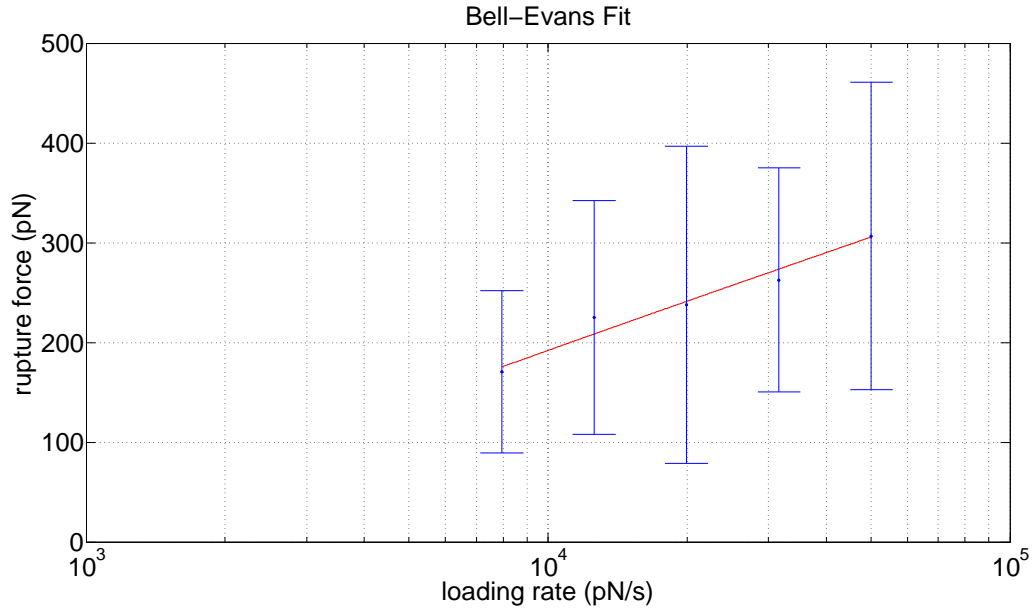


Figure 3.28.: Bell-Evans fit of mean rupture forces calculated for the individual bins shown in figure 3.24 for loading rates starting from 6000 pN/s. Fitting results with 95 % confidence intervals:  $F_\beta=69.29$  pN [38.44, 100.1],  $k_{off}=8.721$  s $^{-1}$  [1.24, 16.21].  $R^2 = 0.9367$ .

For the Bell-Evans fit of the original data, the obtained value for  $k_{off}$  is remarkably similar to the one obtained by a Friddle fit for the whole loading rate range. For the bin-wise mean values, the match is not nearly as good. However, the Friddle fit of the whole range yields a rather wide confidence interval, encompassing the confidence interval of the Bell-Evans fit result, so it is not conclusive whether the two  $k_{off}$  values agree with each other or not.

#### 3.3.6. Population analysis

The force PDFs calculated for the individual bins can be used to examine the data with respect to multiple populations that might occur within it. As most of the force PDFs shown in figures 3.16 to 3.22 appear to have one dominant peak and a smaller second peak at a higher force, two Gaussian functions were fitted into the PDF of each bin. The results are shown in figures 3.29 to 3.35. For each bin, the solid blue curve shows the original ksdensity-derived force PDF, the dashed red lines show the fitted Gaussian functions and the solid red line shows the sum of the fitted Gaussian functions, representing the newly calculated PDF.

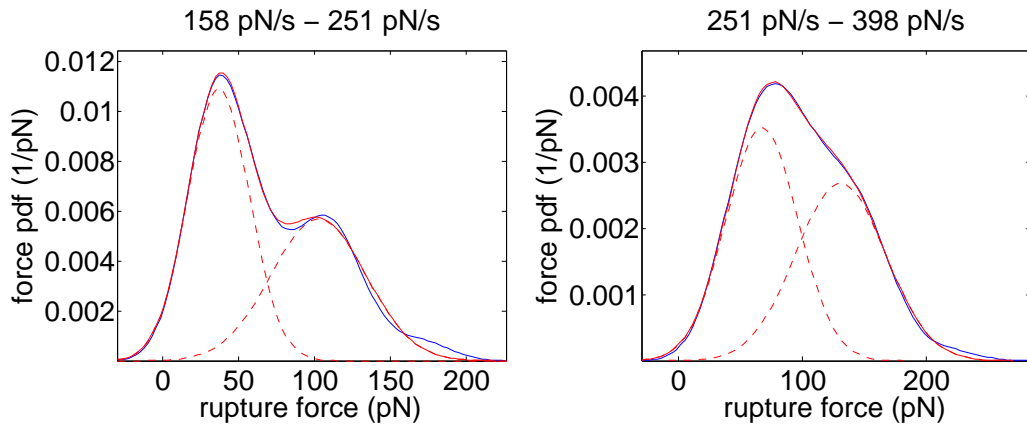


Figure 3.29.: Force PDFs and fitted Gaussian functions for 199.53 pN/s and 316.23 pN/s

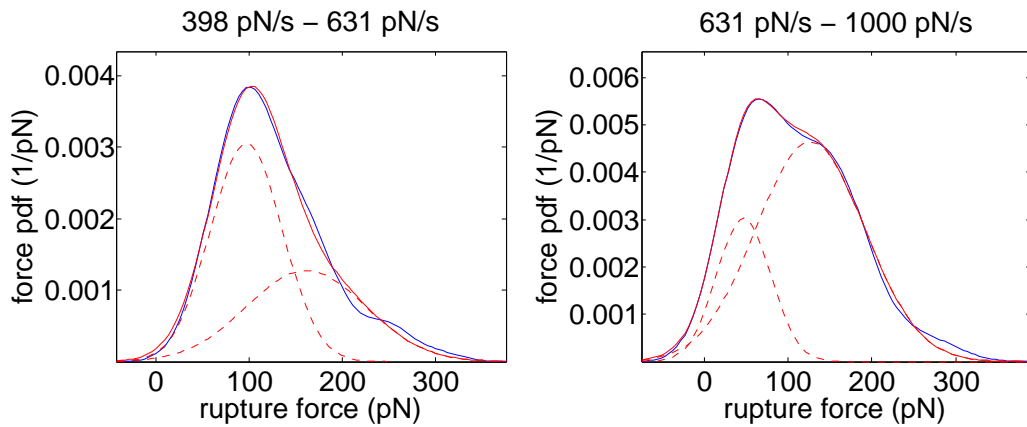


Figure 3.30.: Force PDFs and fitted Gaussian functions for 501.19 pN/s and 794.33 pN/s

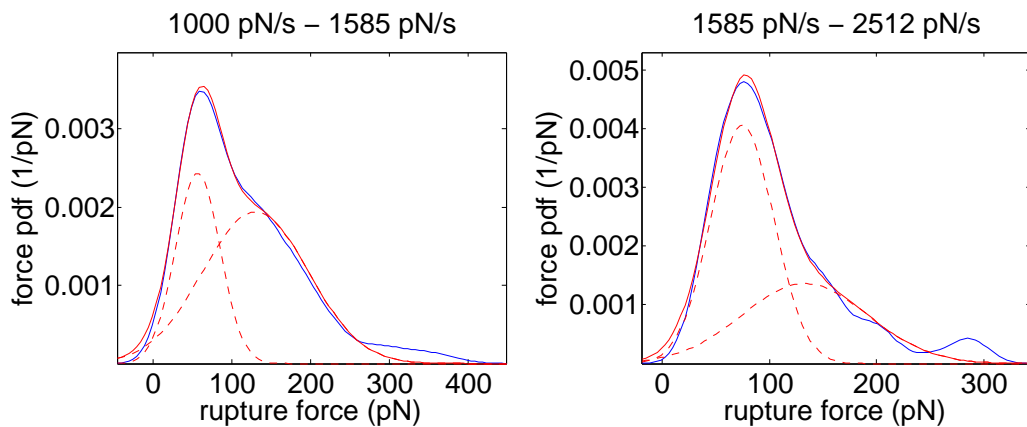


Figure 3.31.: Force PDFs and fitted Gaussian functions for 1258.93 pN/s and 1995.26 pN/s

### 3. Results and Discussion

---

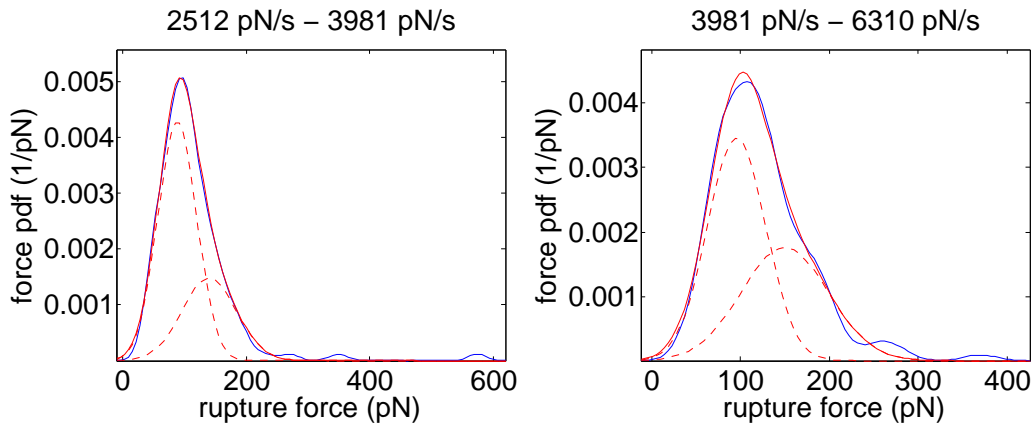


Figure 3.32.: FForce PDFs and fitted Gaussian functions for 3162.28 pN/s and 5011.87 pN/s

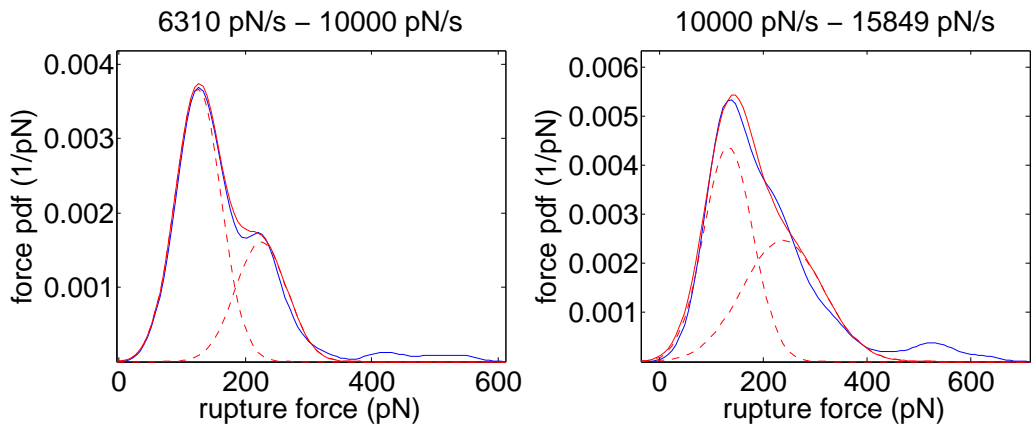


Figure 3.33.: Force PDFs and fitted Gaussian functions for 7943.28 pN/s and 12 589.25 pN/s

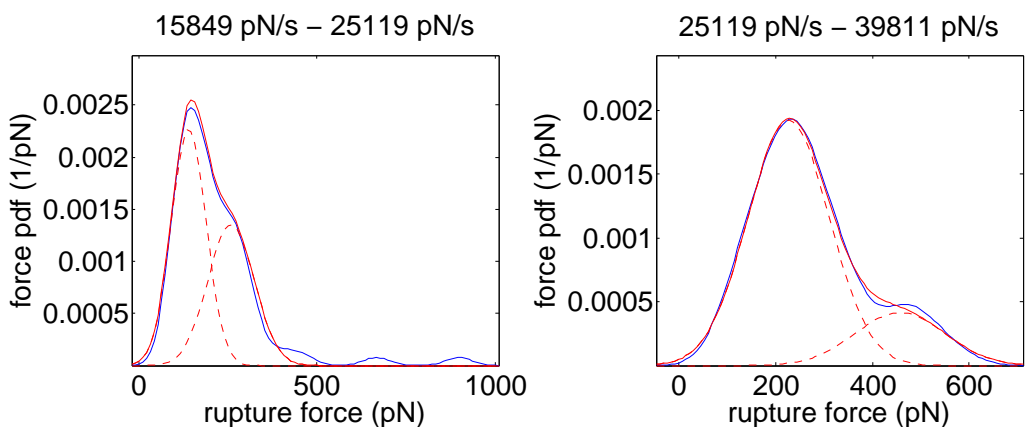


Figure 3.34.: Force PDFs and fitted Gaussian functions for 19 952.62 pN/s and 31 622.78 pN/s

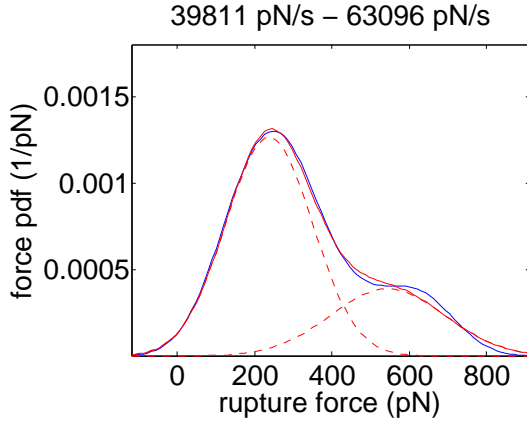


Figure 3.35.: Force PDFs and fitted Gaussian functions for 50118.72 pN/s

The results of population analysis via Gaussian fitting are summarized in table 3.6 and figure 3.36. Table 3.6 shows the mean force  $F_i$ , standard deviation  $s_i$  and area  $A_i$  of the Gaussian function as well as the proportional number of datapoints assigned to the respective population. Figure 3.36 shows population 1 in blue and population 2 in red.

Table 3.6.: Mean value  $F_i$ , standard deviation  $s_i$ , leading coefficient  $A_i$  and proportional number of datapoints  $n_i$  for both populations 1 (lower force) and 2 (higher force) identified via fitting of Gaussian functions on bin-wise force distribution functions for data on CRP and anti-CRP.

bin center (pN/s)	$F_1$ (pN)	$s_1$ (pN)	$A_1$	$n_1$	$F_2$ (pN)	$s_2$ (pN)	$A_2$	$n_2$
199.53	36.85	20.26	0.5543	16.8675	102.47	31.23	0.4457	13.5603
316.23	67.48	29.11	0.5141	32.0734	130.91	36.10	0.4859	30.3086
501.19	96.69	38.69	0.5913	36.7831	161.08	63.84	0.4087	25.4223
794.33	46.94	32.31	0.2450	17.3633	126.39	64.96	0.7550	53.5091
1258.93	56.14	28.42	0.3467	34.4360	129.73	67.17	0.6533	64.8971
1995.26	74.56	29.43	0.5987	57.9883	132.92	58.74	0.4013	38.8635
3162.28	88.47	31.44	0.6749	73.3682	140.06	43.87	0.3251	35.3495
5011.87	95.52	32.79	0.5682	64.7322	149.75	48.95	0.4318	49.2009
7943.28	124.67	36.55	0.6715	71.4314	224.79	40.58	0.3285	34.9466
12589.25	132.04	47.58	0.5206	53.3321	236.82	77.22	0.4794	49.1056
19952.62	139.65	49.11	0.5583	36.5964	258.70	65.00	0.4417	28.9545
31622.78	226.65	83.81	0.8066	37.1935	457.05	92.85	0.1934	8.9168
50118.72	237.65	112.05	0.7118	15.3692	544.21	147.64	0.2882	6.2242

### 3. Results and Discussion

---

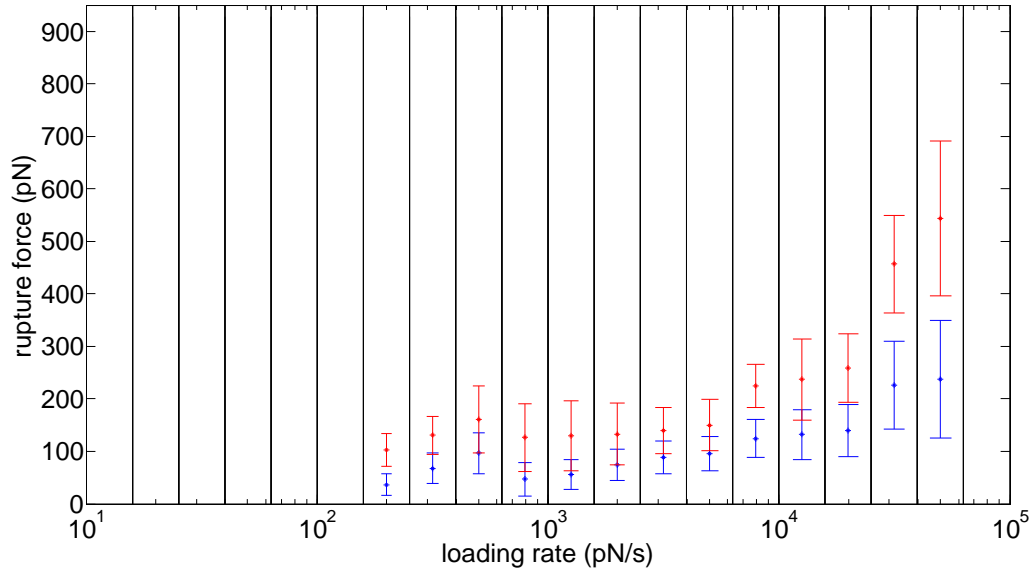


Figure 3.36.: Splitting up of the data collected for CRP and anti-CRP in two populations via fitting with Gaussian functions.  
First (lower force) population given in blue, second (higher force) population given in red.

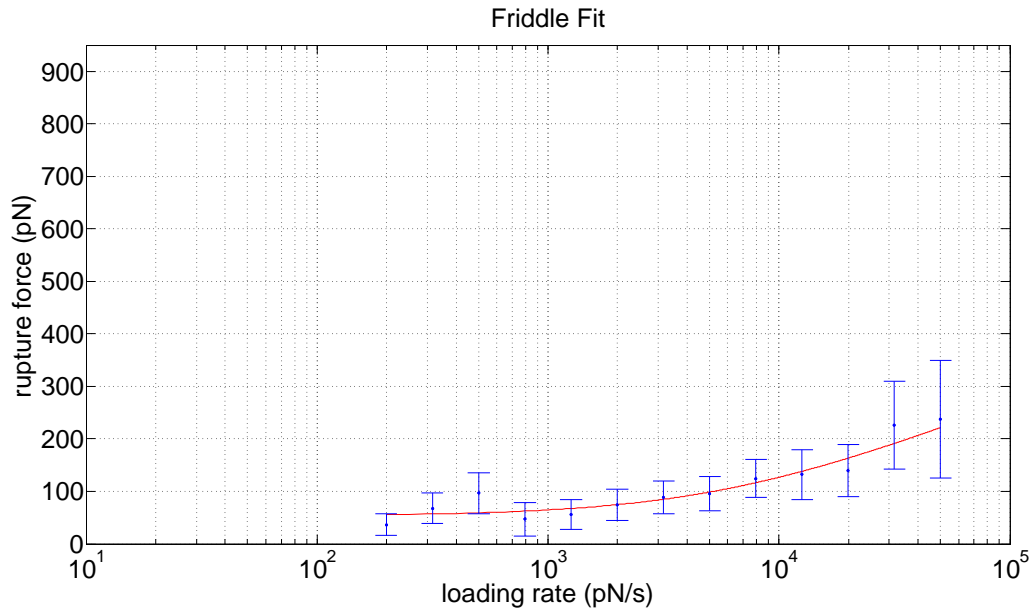


Figure 3.37.: Friddle fit of first population identified for CRP and anti-CRP via Gaussian fitting. Fitting results with 95 % confidence intervals:  $F_{eq}=53.17 \text{ pN}$  [32.92, 73.41],  $F_\beta=75.46 \text{ pN}$  [-22.97, 173.9],  $k_{off}=22.21 \text{ s}^{-1}$  [-18.3, 62.72].  $R^2 = 0.8315$ .

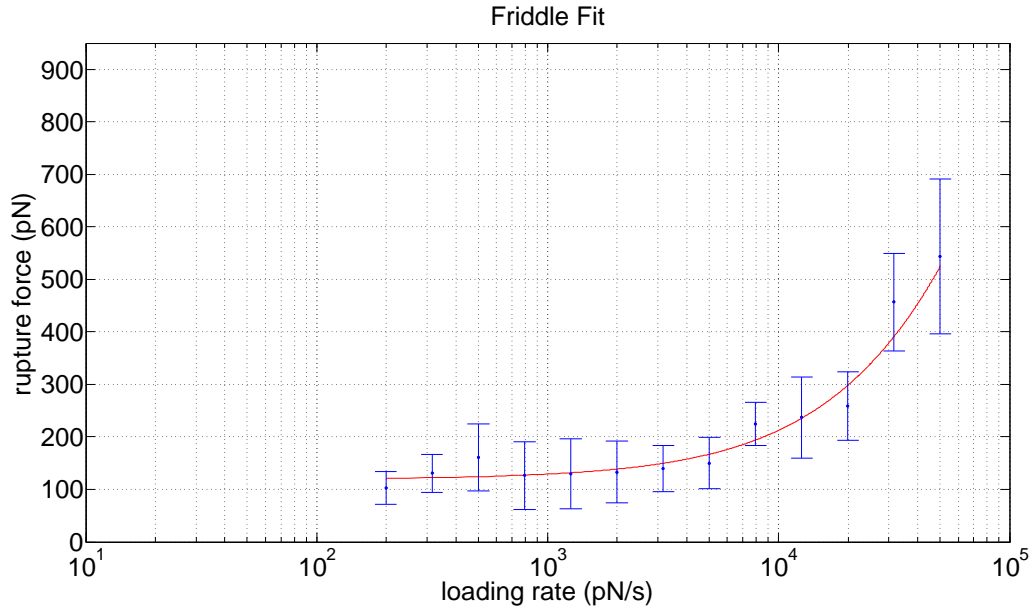


Figure 3.38.: Friddle fit of second population identified for CRP and anti-CRP via Gaussian fitting. Fitting results with 95 % confidence intervals:  $F_{eq}=119.5 \text{ pN}$  [99.25, 139.7],  $F_\beta=1165 \text{ pN}$  [-6051, 8381],  $k_{off}=52.36 \text{ s}^{-1}$  [-9.87, 114.6].  $R^2 = 0.8690$ .

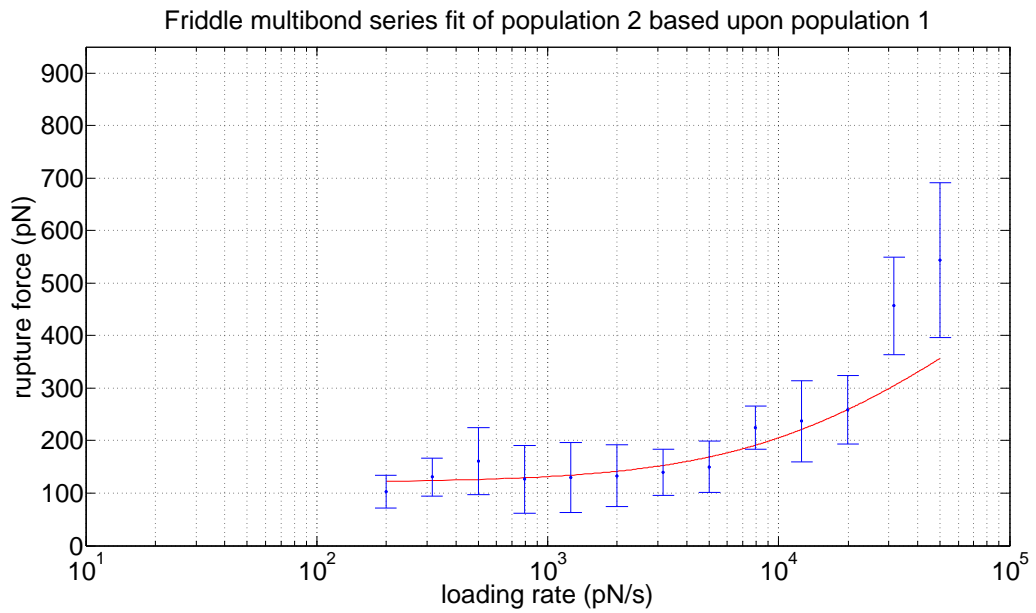


Figure 3.39.: Friddle multibond fit of the second population identified for CRP and anti-CRP via Gaussian fitting based on the first population. Fitting results with 95 % confidence intervals:  $F_{eq}=120.5 \text{ pN}$  [102.7, 138.3].  $R^2 = 0.8082$ .

### 3. Results and Discussion

---

In a first step, the first (lower force) population was fitted with Friddle model. The results are shown in figure 3.37. Next, the second (higher force) population was also fitted with Friddle model independent of the first population. The result is given in figure 3.38.

Finally, the second population was fitted with a Friddle multibond model for  $N = 2$  as given in equation (2.15). For this purpose, the values for  $F_\beta$  and  $k_{off}$  were taken from population 1 and only  $F_{eq}$  was fitted. The result is shown in figure 3.39.

#### 3.3.7. Comparison and discussion of evaluation strategies

Table 3.7 provides a comparison of results acquired for fits performed at multiple stages throughout the analysis of the data on CRP and anti-CRP.

Table 3.7.: Comparison of fitting results for original, bin-wise and population-wise data on CRP and anti-CRP. Friddle fit were done over the whole loading rate range, Bell-Evans fit for loading rates  $r > 6000$  pN/s. The Friddle multibond fit was done for population 2, using the fit results of  $k_{off}$  and  $F_\beta$  from population 1. All fitting results are given with their 95 % confidence intervals. The parameter  $x_\beta$  was calculated via equation (2.10) for a room temperature of 23 °C.

	$k_{off}$ ( $s^{-1}$ )	$F_{eq}$ (pN)	$F_\beta$ (pN)	$x_\beta$ (Å)	$R^2$
Friddle fit original data	11.43 (2.12, 20.73)	95.95 (89.57, 102.3)	91.51 (50.98, 132)	0.4451	0.2222
Friddle fit binned data	31.97 (-39.48, 103.4)	101.3 (80.03, 122.5)	165.4 (-194.5, 525.2)	0.2463	0.7570
Friddle fit population 1	22.21 (-18.3, 62.72)	53.17 (32.92, 73.41)	75.46 (-22.97, 173.9)	0.5397	0.8315
Friddle fit population 2	52.36 (-9.87, 114.6)	119.5 (99.25, 139.7)	1165 (-6051, 8381)	0.0350	0.8690
Friddle multibond fit ( $N = 2$ )	-	120.5 (102.7, 138.3)	-	-	0.8082
Bell-Evans fit original data	10.33 (6.438, 14.23)	-	78.1 (60.54, 95.67)	0.5235	0.1453
Bell-Evans fit binned data	8.72 (1.24, 16.21)	-	69.29 (38.44, 100.1)	0.5901	0.9367

Fitting the original (not-binned) data as compared to the bin-wise mean values yields rather low  $R^2$  values, which is not surprising as the unbinding force data stretches out over a wide range for every loading late. Still, fitting of the original as compared to the binned data yields narrower confidence intervals as the total number of fitted datapoints is by far higher. Therefore, binning the data and fitting of the bin-wise mean values does not appear to have real advantages over fitting of the original data cloud other than that the curve shape is better visible, making it easier to identify which model is suitable for fitting.

Fitting Gaussian functions onto the bin-wise force distribution functions allows to identify individual populations within the data. These populations could correspond to multibonds (multiple bonds of the same interaction type occurring at the same time), to different kinds of specific interactions or one or multiple populations could be attributed to unspecific interaction between the molecules on the tip and the surface. In an attempt to find out which of these is the case, the two isolated populations were fitted both individually and with a multibond model of population 2 based upon population 1. The goodness-of-fit ( $R^2$ ) of the result is similar to the corresponding value for individual Friddle fitting of population 2 (0.8082 versus 0.8690). Also, the obtained values for  $F_{eq}$  are very similar, both being about a factor two higher than the corresponding value for population 1. However, a visual evaluation of the fitting result in figure 3.39 shows that the fit underestimates the rather high forces obtained for the highest two loading rates, with the theoretical values not even lying within the margin of the standard deviations. In contrast, the value for  $x_\beta$  obtained by individual fitting of population 2 is strikingly low, reducing the credibility of this fit (although the confidence interval of the corresponding  $F_\beta$  value is very wide, making the value quite uncertain).

It has to be pointed out that the two bins at the highest loading rates show a rather low number of datapoints (47 and 22, see table 3.5), rendering their estimated force distributions rather uncertain. Especially for the last bin this can also be seen in figure B.7, as there is quite some divergence between the force distributions calculated using two different methods. Also, unspecific interaction can occur in addition to multibonds, possibly yielding datapoints at high forces.

Further, the values for  $k_{off}$  can be compared. The value obtained for the Friddle fit of the bin-wise mean forces lies between the values obtained for individual fitting of population 1 and population 2. This would make sense if the populations were independent and the bin-wise mean forces represent an average of the two interactions. However, the confidence intervals are rather wide for all cases, showing considerable overlaps. Therefore, with the data at hand it cannot be concluded for sure whether the second population corresponds to a double-bond scenario or not, but there are indications that this might be the case. As the system comprises a bivalent antibody attached to the tip and a surface densely covered by CRP, population 2 could very well represent the  $N = 2$  case.

## 3.4. MSC and RAGE-antibody interaction study evaluation

### 3.4.1. Collected DFS results

To test the developed evaluation framework on an additional dataset, in the following an analysis will be presented of data recorded by Sarah Rautnig (2019) for her master's thesis at the Institute of Biophysics, Johannes Kepler University (Linz), under supervision of Andreas Ebner. For details on tip and sample preparation please see the master's thesis of Sarah Rautnig.

Figure 3.40 shows the collected results of 24 measurement series recorded on MSC with anti-RAGE. All in all, 5977 bindings were detected for this system. As will be motivated below, Friddle fit was selected for evaluation of the data on MSC and anti-RAGE. The result is given in figure 3.41.

### 3.4.2. Loading rate binning

As for the data on CRP and anti-CRP, the data for MSC and anti-RAGE was binned in five bins per decade with a minimum number of twenty datapoints per bin. The binning result is shown in figure 3.42. As the overall curve shape suggests an analysis with Friddle model, figure 3.43 shows the results of a Friddle fit performed for the bin-wise mean values of the unbinding force with the weights defined as described in section 2.4.5. The bin-wise force distribution functions estimated by two kernel methods (formula (1.10) in red and *ksdensity* in blue) are provided in the appendix in figures C.1 to C.8. Again, these figures show that the higher the number of datapoints in the respective bin is, the closer the match between the two PDFs tends to become.

### 3.4.3. Population analysis

Figure 3.44 shows the force distribution development (calculated by *ksdensity*) for the interaction study on MSC and anti-RAGE. For isolating individual populations, these force PDFs were each fitted with two Gaussian functions, respectively. The results of Gaussian fitting are given in the appendix in figures D.1 to D.8. The results of population analysis are summarized in figure 3.45 and table 3.8.

As for CRP and anti-CRP, the two isolated populations were first fitted individually with Friddle model. The results can be seen in figures 3.46 and 3.47. Then, a Friddle multibond fit was performed for the second (higher force) population based on the parameters obtained from the Friddle fit of the first population, as shown in figure 3.48.

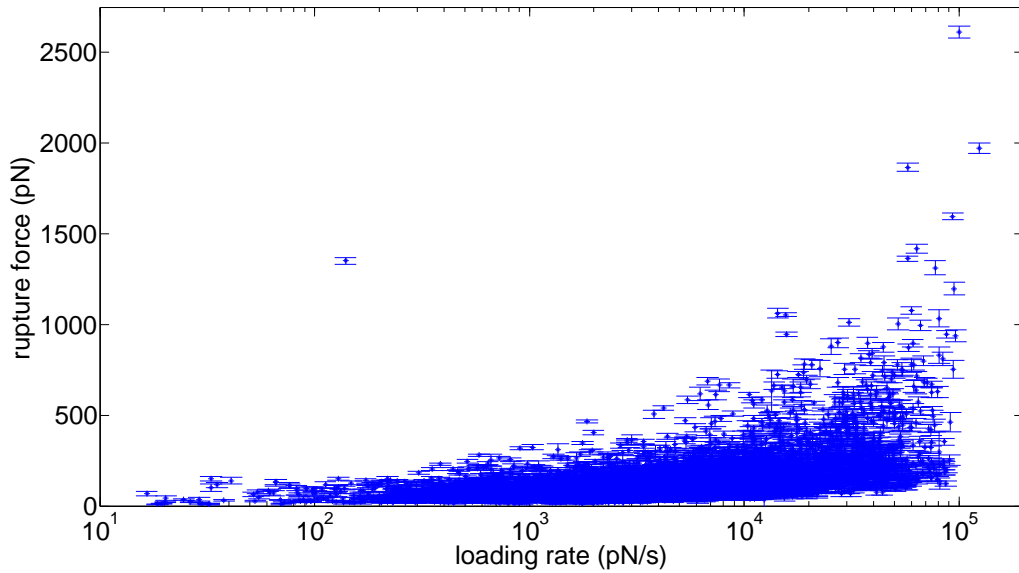


Figure 3.40.: Rupture force data recorded for studying the interaction of MSC and anti-RAGE. Collected from 24 distinct pulling rates and plotted towards the loading rate. Error bars give the standard deviation of the individual datapoints. Data recorded by Sarah Rautnig (2019).

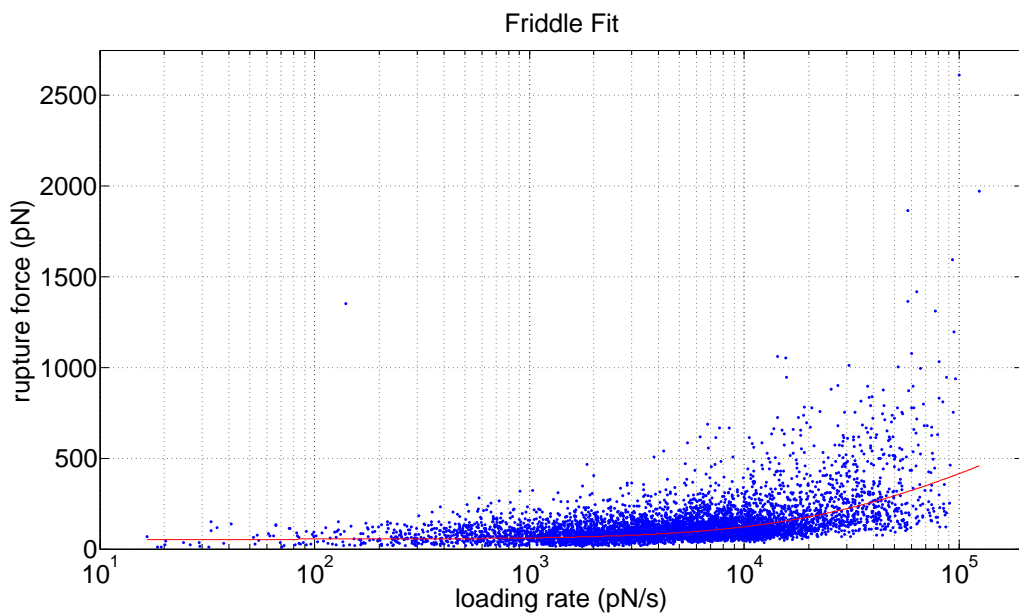


Figure 3.41.: Friddle fit for mean rupture forces of MSC and anti-RAGE performed for 5977 individual datapoints. Fitting results with 95 % confidence intervals:  $F_{eq}=52.69 \text{ pN}$  [49.68, 55.7],  $F_\beta=256.2 \text{ pN}$  [189.7, 322.6],  $k_{off}=57.55 \text{ s}^{-1}$  [48.68, 66.41].  $R^2 = 0.2659$ .

### 3. Results and Discussion

---

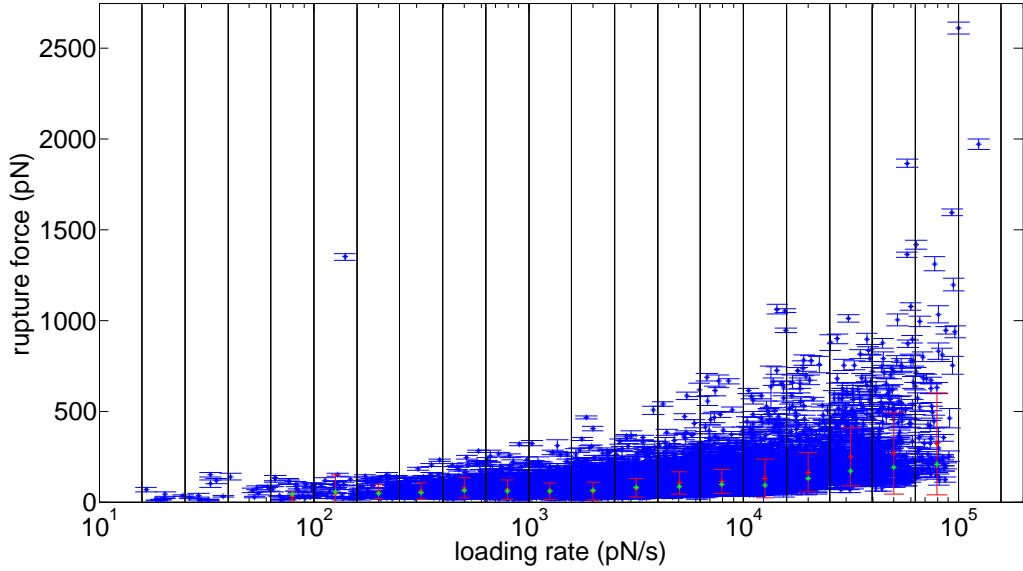


Figure 3.42.: Binning of the collected data recorded for MSC and anti-RAGE into 5 bins per decade with a minimum of 20 datapoints per bin. Red point gives the weighted mean value of forces in the bin projected onto the apparent center point, red errorbars give the weighted standard deviations. Green points give the maximum of the rupture force distribution in the bin. Data recorded by Sarah Rautnig (2019).

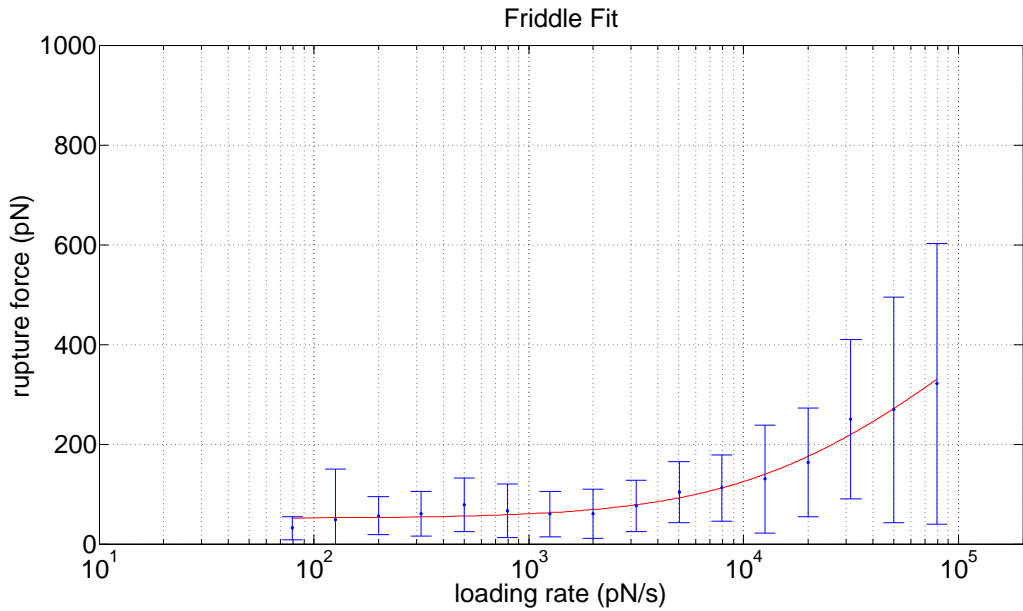


Figure 3.43.: Friddle fit for mean rupture forces of MSC and anti-RAGE performed for the mean rupture forces calculated for the individual bins shown in figure 3.42 . Fitting results with 95 % confidence intervals:  $F_{eq}=51.29$  pN [40.69, 61.89],  $F_\beta=162$  pN [-1.06, 325.1],  $k_{off}=43.87$  s $^{-1}$  [12.29, 75.45].  $R^2 = 0.9188$ .

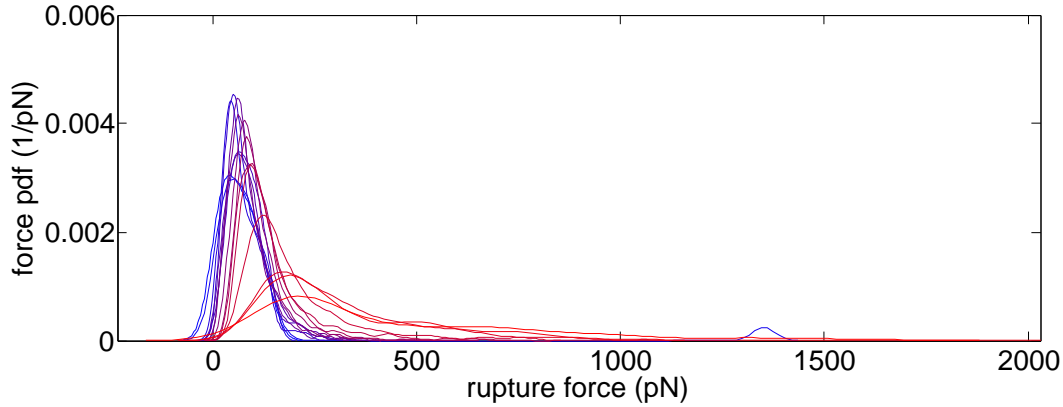


Figure 3.44.: Force distribution development of MSC and anti-RAGE for increasing loading rates (blue for lowest, red for highest loading-rate bin). Loading rate bin center points given in table 3.8.

Table 3.8.: Mean value  $F_i$ , standard deviation  $s_i$ , leading coefficient  $A_i$  and proportional number of datapoints  $n_i$  for both populations 1 (lower force) and 2 (higher force) identified via fitting of Gaussian functions on bin-wise force distribution functions for data on MSC and anti-RAGE.

bin center (pN/s)	$F_1$ (pN)	$s_1$ (pN)	$A_1$	$n_1$	$F_2$ (pN)	$s_2$ (pN)	$A_2$	$n_2$
79.43	26.41	31.31	0.4555	9.9884	91.56	39.52	0.5445	11.9395
125.89	26.75	25.02	0.1617	3.5612	74.75	49.69	0.8383	18.4596
199.53	41.88	22.98	0.5951	32.9060	106.97	33.06	0.4049	22.3903
316.23	45.82	22.79	0.5398	49.4343	96.75	37.97	0.4602	42.1405
501.19	46.75	20.29	0.1667	26.4184	88.89	42.68	0.8333	132.0541
794.33	63.42	35.81	0.7179	173.2170	131.36	52.57	0.2821	68.0571
1258.93	57.37	24.75	0.5409	219.9927	104.99	44.28	0.4591	186.7449
1995.26	62.05	28.49	0.6476	397.3039	125.52	52.52	0.3524	216.1523
3162.28	74.62	28.52	0.5728	425.7833	123.49	49.34	0.4272	317.4936
5011.87	82.11	28.97	0.5232	425.596	135.27	49.17	0.4768	387.8809
7943.28	89.55	34.00	0.6387	567.5335	164.25	54.70	0.3613	321.0342
12589.25	98.00	35.25	0.6823	499.4873	197.58	68.42	0.3177	232.5966
19952.62	124.89	46.22	0.5847	218.0800	241.47	101.87	0.415	154.8872
31622.78	183.83	79.87	0.5137	135.5521	375.06	188.50	0.4863	128.3222
50118.72	193.30	83.03	0.5513	96.5917	484.08	265.34	0.4487	78.6034
79432.82	211.54	115.56	0.5402	33.4850	647.70	277.20	0.4598	28.5070

### 3. Results and Discussion

---

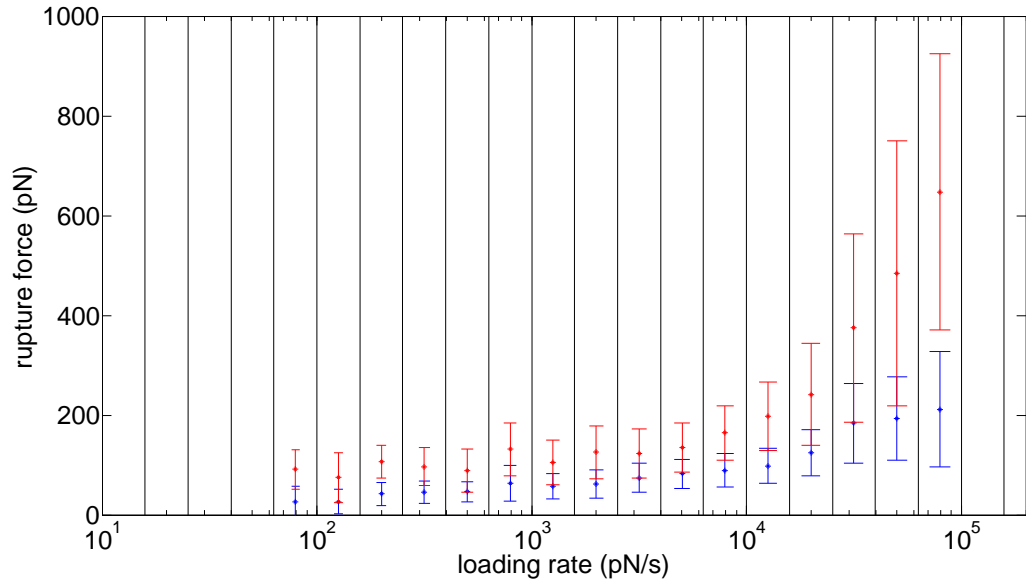


Figure 3.45.: Splitting up of the data collected for MSC and anti-RAGE in two populations via fitting with Gaussian functions. First (lower force) population given in blue, second (higher force) population given in red. Data recorded by Sarah Rautnig (2019).

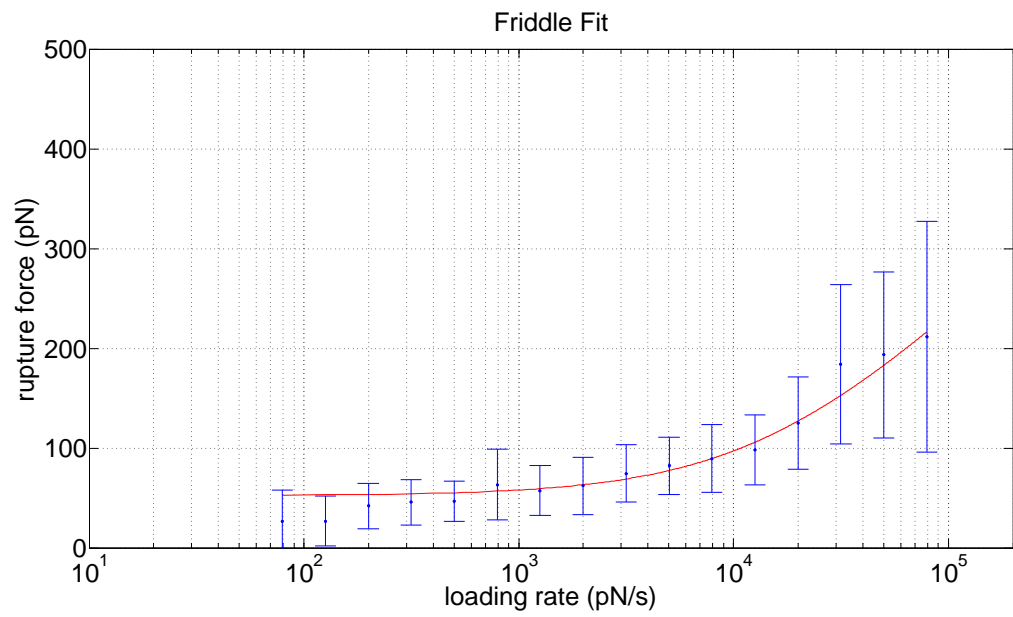


Figure 3.46.: Friddle fit of first population identified for MSC and anti-RAGE via Gaussian fitting. Fitting results with 95 % confidence intervals:  $F_{eq}=52.31 \text{ pN}$  [44.65, 59.97],  $F_\beta=91.37 \text{ pN}$  [4.62, 178.1],  $k_{off}=54.83 \text{ s}^{-1}$  [2.24, 107.4].  $R^2 = 0.9257$ .

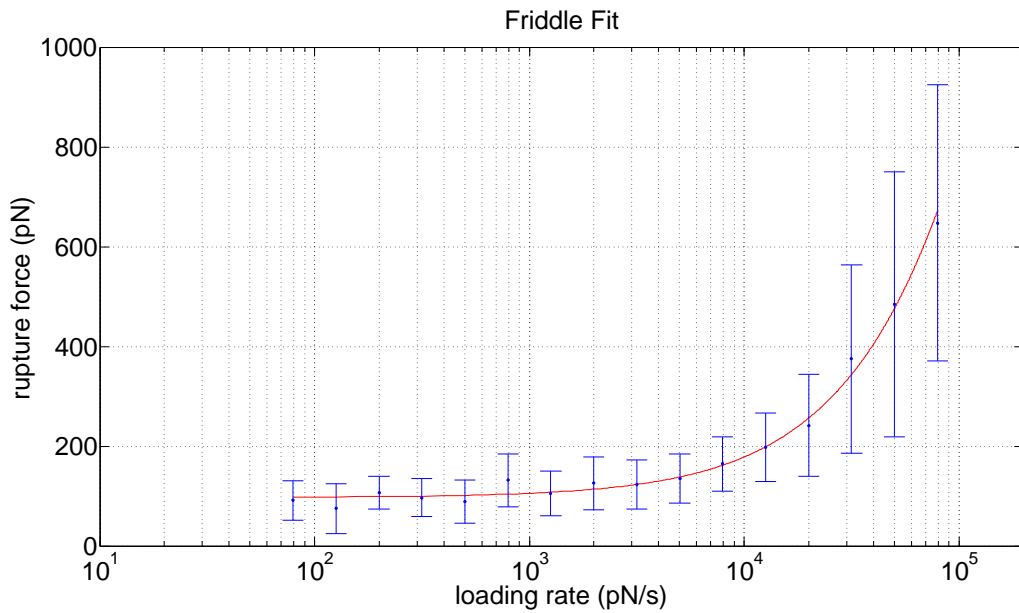


Figure 3.47.: Friddle fit of second population identified for MSC and anti-RAGE via Gaussian fitting. Fitting results with 95 % confidence intervals:  $F_{eq}=97.28 \text{ pN}$  [89.32, 105.3],  $F_\beta=2264 \text{ pN}$  [-6311, 10839],  $k_{off}=65.35 \text{ s}^{-1}$  [41.64, 89.07].  $R^2 = 0.9548$ .

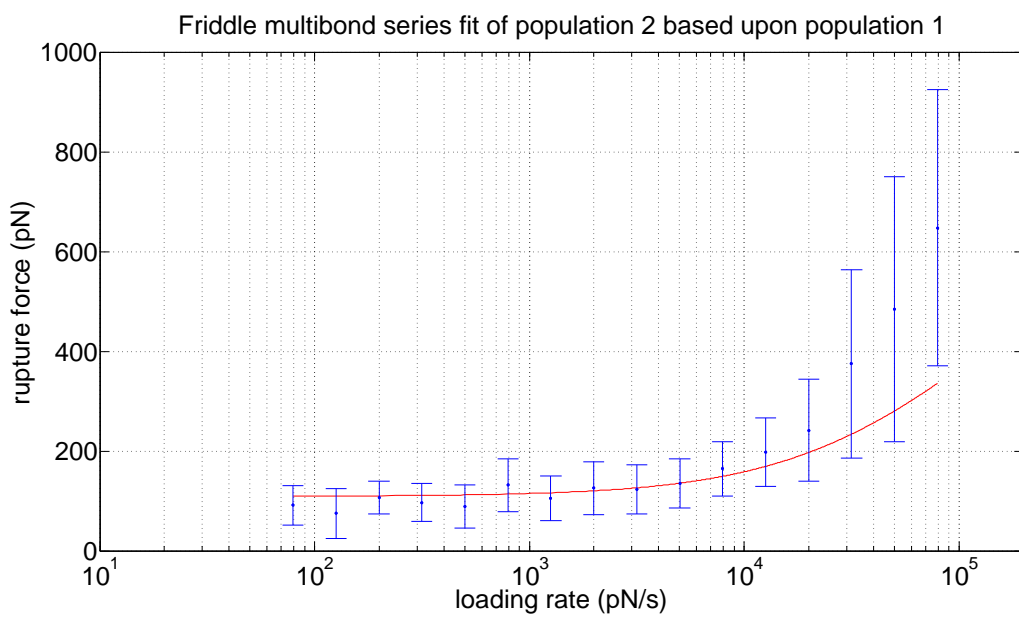


Figure 3.48.: Friddle fit of second population identified for MSC and anti-RAGE via Gaussian fitting based on the first population. Fitting results with 95 % confidence intervals:  $F_{eq}=109.3 \text{ pN}$  [102.7, 138.3].  $R^2 = 0.7388$ .

### 3. Results and Discussion

---

#### 3.4.4. Comparison and discussion of evaluation strategies

Table 3.9 shows a comparison of all fits performed for the data on MSC and anti-RAGE recorded by Sarah Rautnig (2019).

Table 3.9.: Comparison of fitting results for original, bin-wise and population-wise data on MSC and anti-RAGE. The Friddle multibond fit was done for population 2, using the fit results of  $k_{off}$  and  $F_\beta$  from population 1. The parameter  $x_\beta$  was calculated via equation (2.10) for a room temperature of 23 °C.

	$k_{off}$ ( $\text{s}^{-1}$ )	$F_{eq}$ (pN)	$F_\beta$ (pN)	$x_\beta$ ( $\text{\AA}$ )	$R^2$
Friddle fit original data	57.55 (48.68, 66.41)	52.69 (49.68, 55.7)	256.2 (189.7, 322.6)	0.1590	0.2659
Friddle fit binned data	43.87 (12.29, 75.45)	51.29 (40.69, 61.89)	162 (-1.06, 325.1)	0.2514	0.9188
Friddle fit population 1	54.83 (2.239, 107.4)	52.31 (44.65, 59.97)	91.37 (4.622, 178.1)	0.4458	0.9257
Friddle fit population 2	65.35 (41.64, 89.07)	97.28 (89.32, 105.3)	2264 (-6311, 10839)	0.0180	0.9548
Friddle multibond fit ( $N = 2$ )	-	109.3 (96.84, 121.7)	-	-	0.7388

Altogether, 5977 unbinding events were detected over a series of 24 SMFS experiments. This high amount of data can be expected to make the whole analysis more profound than the analysis of CRP and anti-CRP.

As for CRP and anti-CRP, the data was split up in two populations by fitting of Gaussian functions onto the bin-wise unbinding force PDFs. The two populations were fitted individually with Friddle model and related to each other by performing a Friddle multibond model fit of the second populations based upon the first population. Again, the multibond friddle fit underestimates the high forces for the highest loading rates. Also, the parameter  $R^2$  (goodness-of-fit) is considerably lower for the Friddle multibond fit than for the individual Friddle fits.

On the other hand, the value obtained for  $x_\beta$  for fitting only population 2 is remarkably low (although it is rather uncertain, as the confidence interval of the corresponding  $F_\beta$  is rather wide).

All in all, it is not conclusive whether the second population really corresponds to a multibond. However, considering that the system under investigation is a stem cell, exhibiting a multitude of

### 3.4. MSC and RAGE-antibody interaction study evaluation

---

receptors on its surface, it would be plausible that a substantial part of the detected bindings is caused by unspecific interaction of the RAGE-antibody with the cell membrane. Based on the low  $R^2$  value obtained for the Friddle multibond fit as compared to the individual fit of population 2, it could be concluded that the second population does not represent a double-bond scenario, but an independent interaction type.

The results indicate that for this system it does not make sense to split the data in two populations. It might be recommendable to repeat the evaluation by fitting only one Gaussian function (thereby disregarding outliers) and fit the mean values of the Gaussian functions with Friddle model.

### 3.5. Conclusion and outlook

This master's thesis comprises the evaluation of an interaction study on CRP and anti-CRP. The data obtained from DFS experiments were evaluated by different methods. The most important approach relied on binning of the data into a certain number of segments per decade with respect to the loading rate. For the datapoints within each bin, the force distribution functions were calculated and analyzed individually. The development of force distributions over the spectrum of loading rates is expected to contain valuable information on the nature of the underlying interaction. Here, it was attempted to identify individual populations occurring within the data by fitting it with two Gaussian functions, which were then interpreted as corresponding to two populations (one of lower, one of higher rupture forces). The two populations were fitted individually with Friddle model and then related to each other by a multibond Friddle fit of the second population based on the parameters obtained for the first population. The results indicate that the two populations might correspond to cases in which single- and double-bonds occur within the system.

However, the results are not conclusive. It turns out that while one can separate the data into two (or more) groups by Gaussian fitting, interconnecting the populations and interpreting their relationship is difficult. Maybe more sophisticated fitting algorithms, like a maximum-likelihood fit, would yield parameters with narrower confidence intervals, lending more weight to conclusions drawn from the fits and their relationships.

More research is necessary to characterize the interaction of CRP and anti-CRP. One possibility would be to reverse the system, hence to couple the CRP-molecule to the cantilever tip and bind anti-CRP on the substrate surface, and then perform another measurement series. In the configuration as the system was measured here, double-bonds can occur because the bivalent antibody has two short segments by which it can potentially bind to the CRP-covered surface. If the system was to be reversed, one could expect to detect only single-bonds, as CRP is rather small and a single CRP-molecule should only bind to one binding site. If such a dataset were to be recorded, it could be related to the data acquired for this master's, which could then be interpreted easier. The first population identified for the system as measured for this master's thesis should then correspond to the data obtained from the reversed system, as the rupture forces should be about the same.

Further studies on CRP are of interest as it stands in the center of an ongoing collaboration with the Surface Nanoengineering Group from the Institute of Physical Chemistry of the Polish Academy of Sciences. Future goals of the collaboration include additional SMFS studies on the interaction of CRP with peptides identified by the collaborator via phage-display. These studies will then allow to compare the affinities of the antibodies and the peptides to CRP.



# **Appendix**



## Appendix A.

### SMFS results for CRP and anti-CRP

Table A.1.: Specifications on the SMFS results for CRP and anti-CRP

sample	cantilever	$k$ (pN/nm)	rate ( $\mu\text{m}/\text{s}$ )	max ht (s)	total	binding probability (%)
#7	B	23	0.04	0	618	13.27
#6	C	13	0.08	0	1905	4.51
#7	C	13.33*	0.2	0.3	1512	8.99
#4	B	22	0.3	0.3	1291	10.92
#6	D	43	0.6	0.3	4965	6.89
#5	B	32	1	0.3	1486	4.10
#5	B	31	1.2	0.3	1858	7.48
#4	D	45	2.5	0.5	1224	5.64

In table A.1, the column labeled with  $k$  contains the spring constant values of the respective cantilevers, *rate* refers to the pulling rate and *total* gives the total number of force-distance cycles recorded for this particular pulling rate. The binding probability was calculated as the percentage of curves that showed a binding event. The hold time defines the time over which the tip is in contact with the surface. The maximum hold time (*maxht*) was varied for each pulling rate to achieve the best binding probability. The spring constant of tip 5C from sample #7, highlighted with a star (\*) could not be determined by the thermal noise method, as this tip was damaged during the experimental session. Therefore, an average was calculated from three cantilevers taken from the same package. These can be assumed to have a similar spring constant due to their joint production.

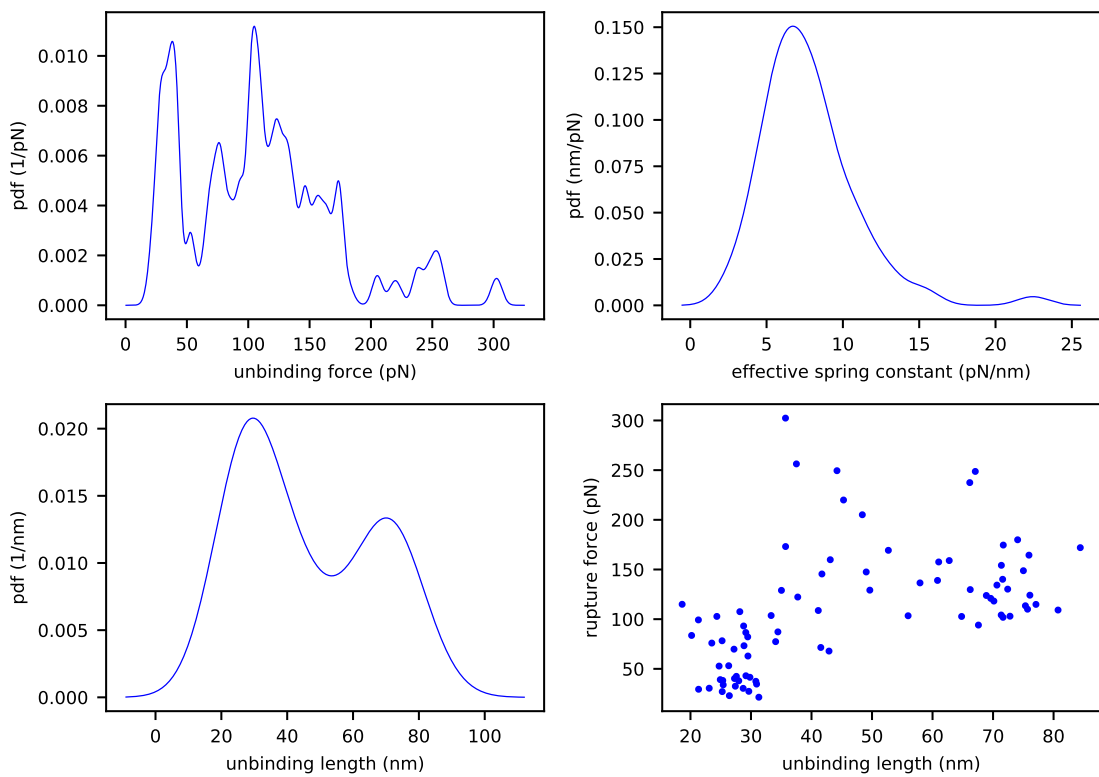


Figure A.1.: Pulling rate  $0.04 \mu\text{m}/\text{s}$ , maximum hold time  $0\text{s}$

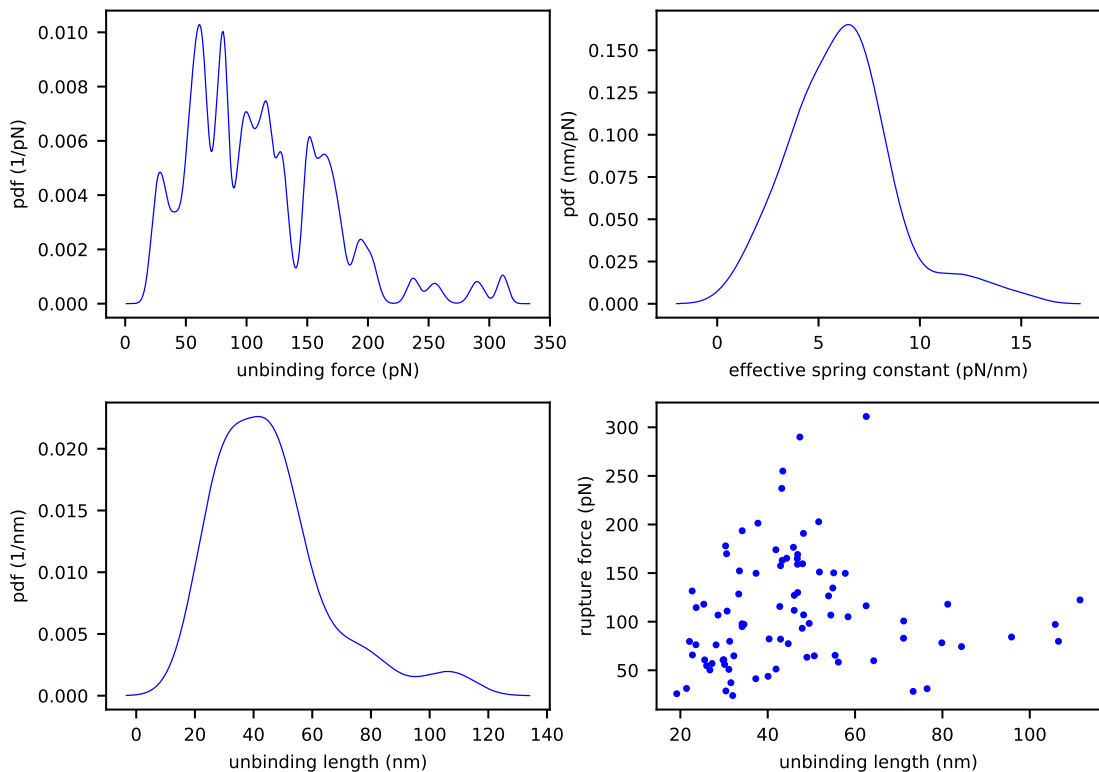


Figure A.2.: Pulling rate  $0.08 \mu\text{m}/\text{s}$ , maximum hold time  $0\text{s}$

## Appendix A. SMFS results for CRP and anti-CRP

---

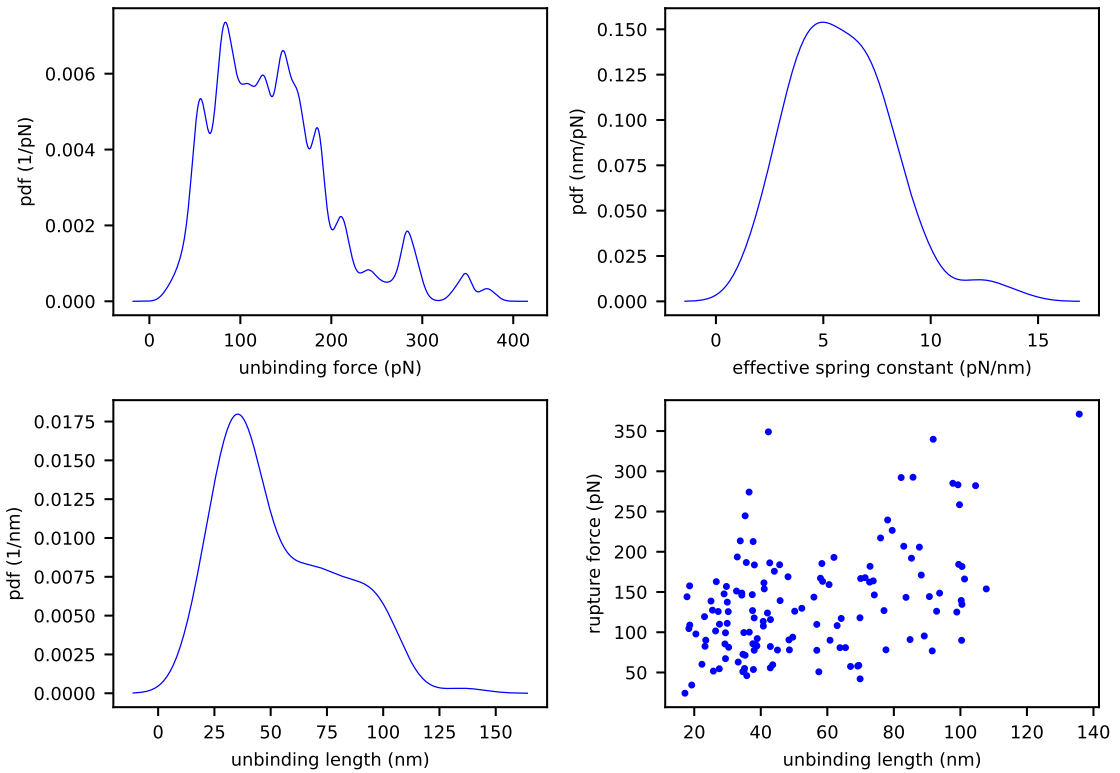
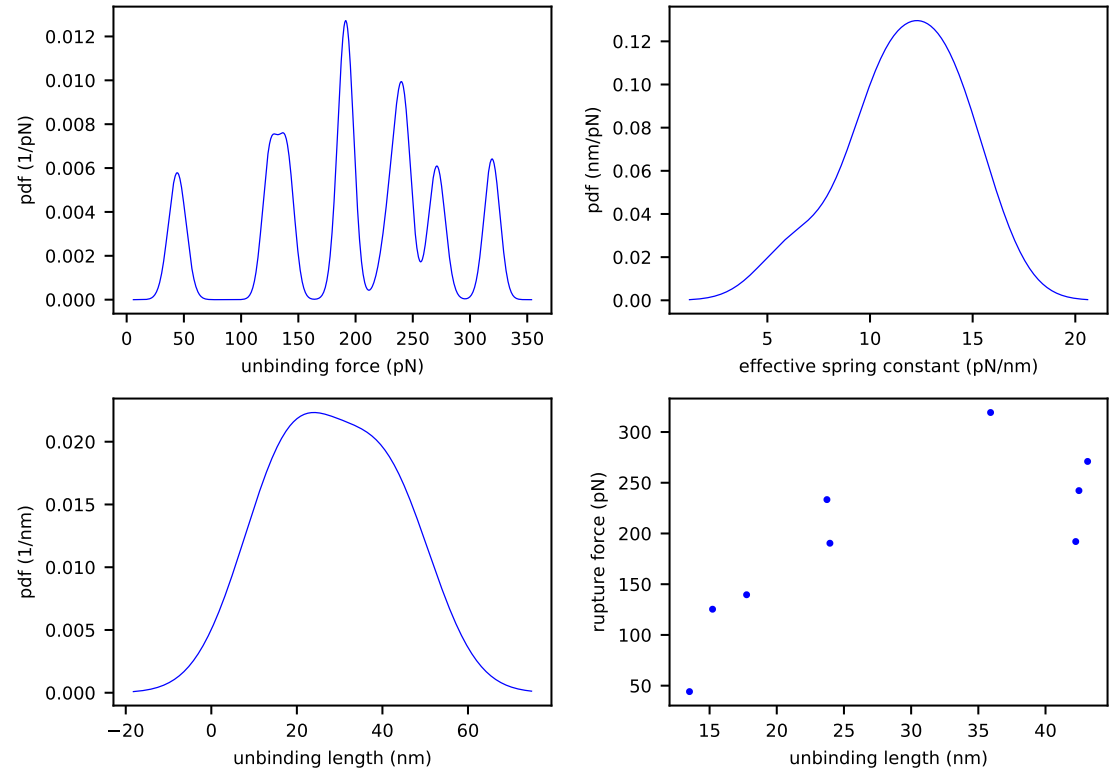


Figure A.3.: Pulling rate  $0.2 \mu\text{m/s}$ , maximum hold time  $0.3 \text{s}$



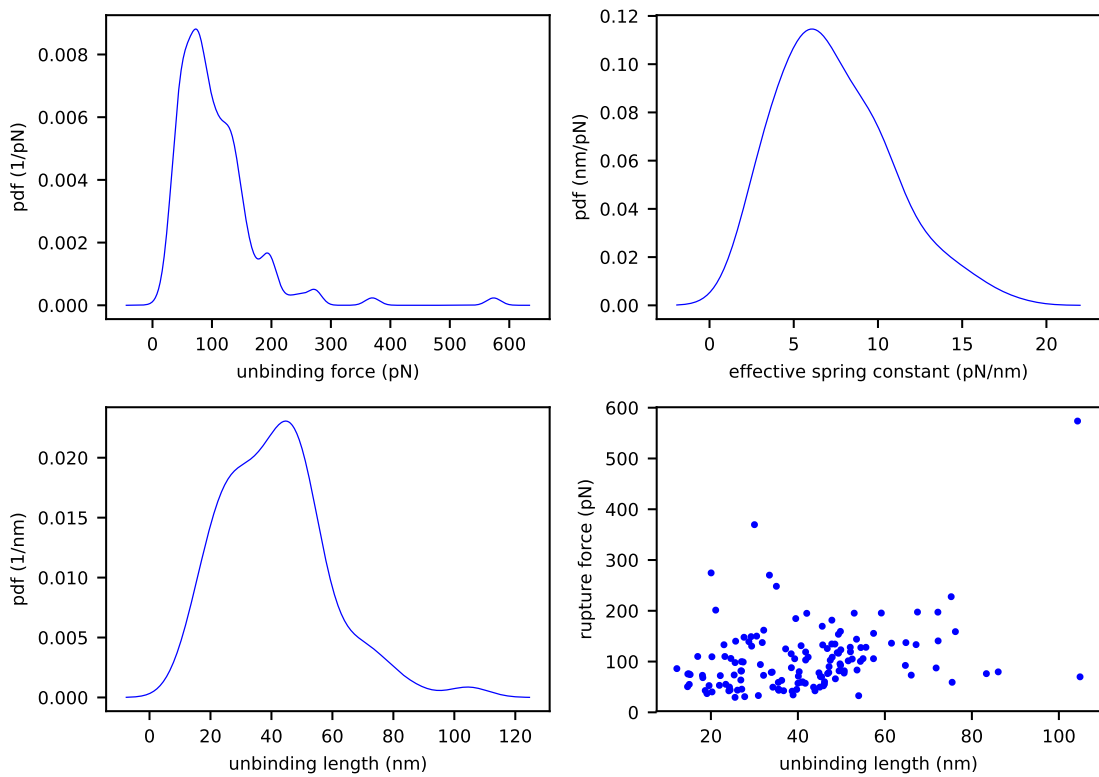


Figure A.5.: Pulling rate  $0.3 \mu\text{m/s}$ , maximum hold time  $0.3 \text{s}$

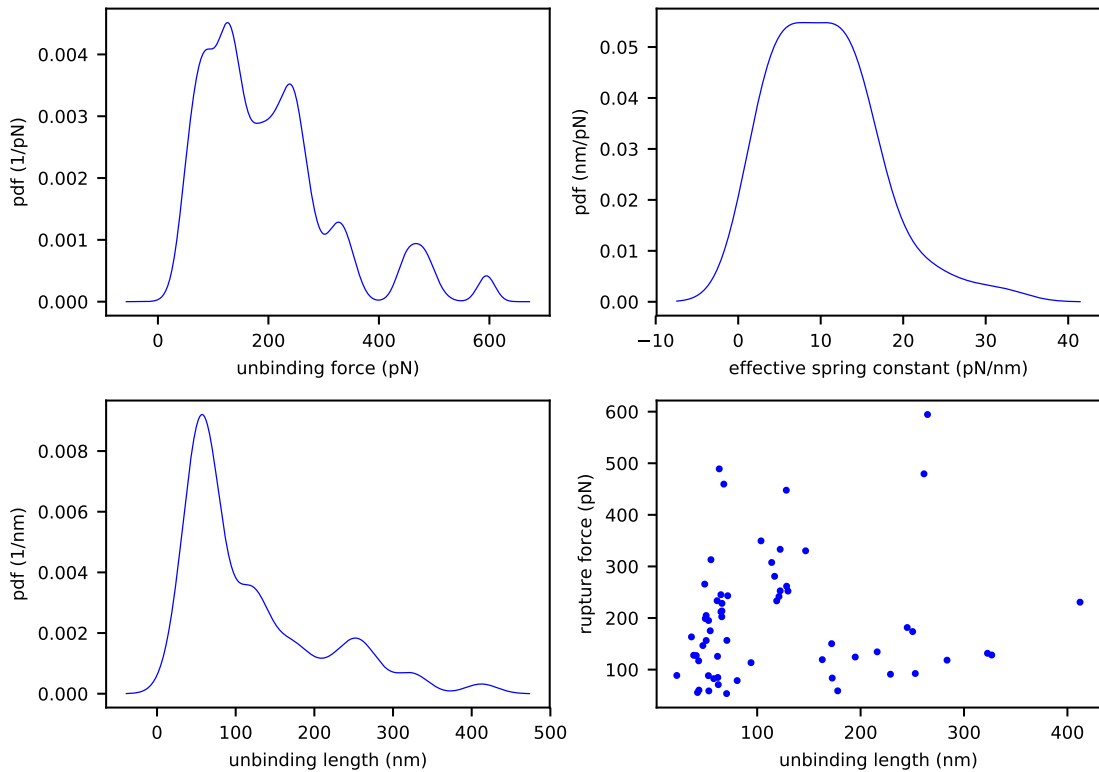


Figure A.6.: Pulling rate  $1 \mu\text{m/s}$ , maximum hold time  $0.3 \text{s}$

## Appendix A. SMFS results for CRP and anti-CRP

---

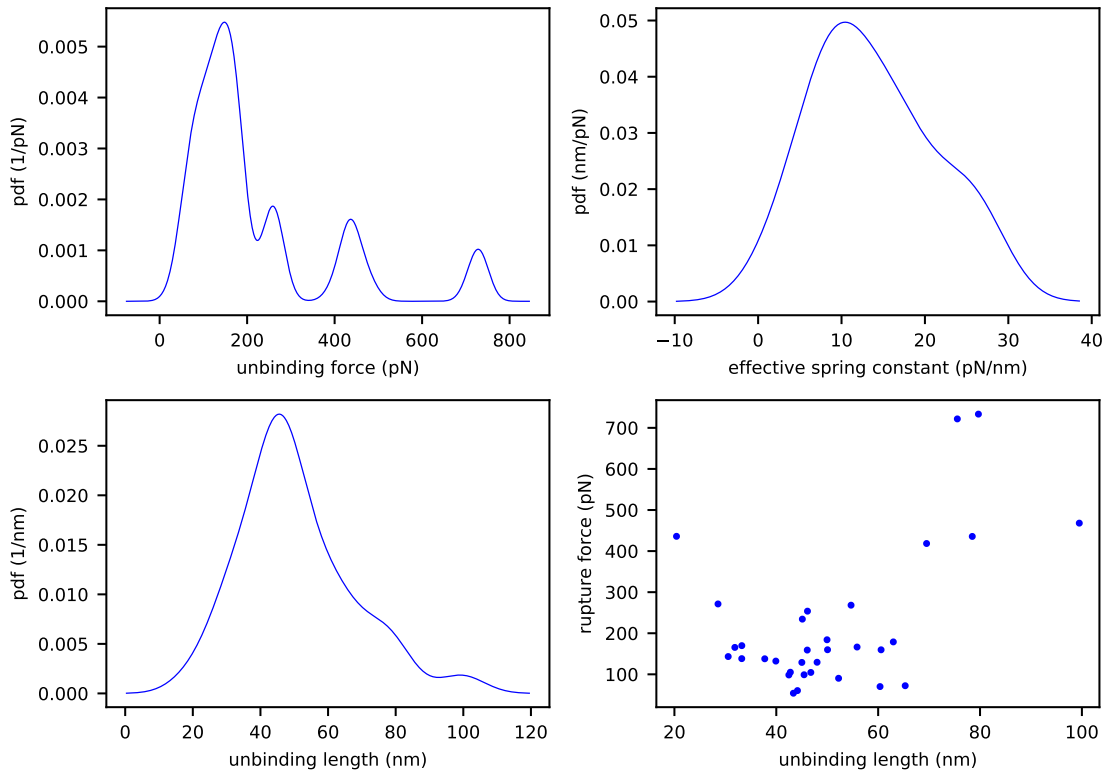
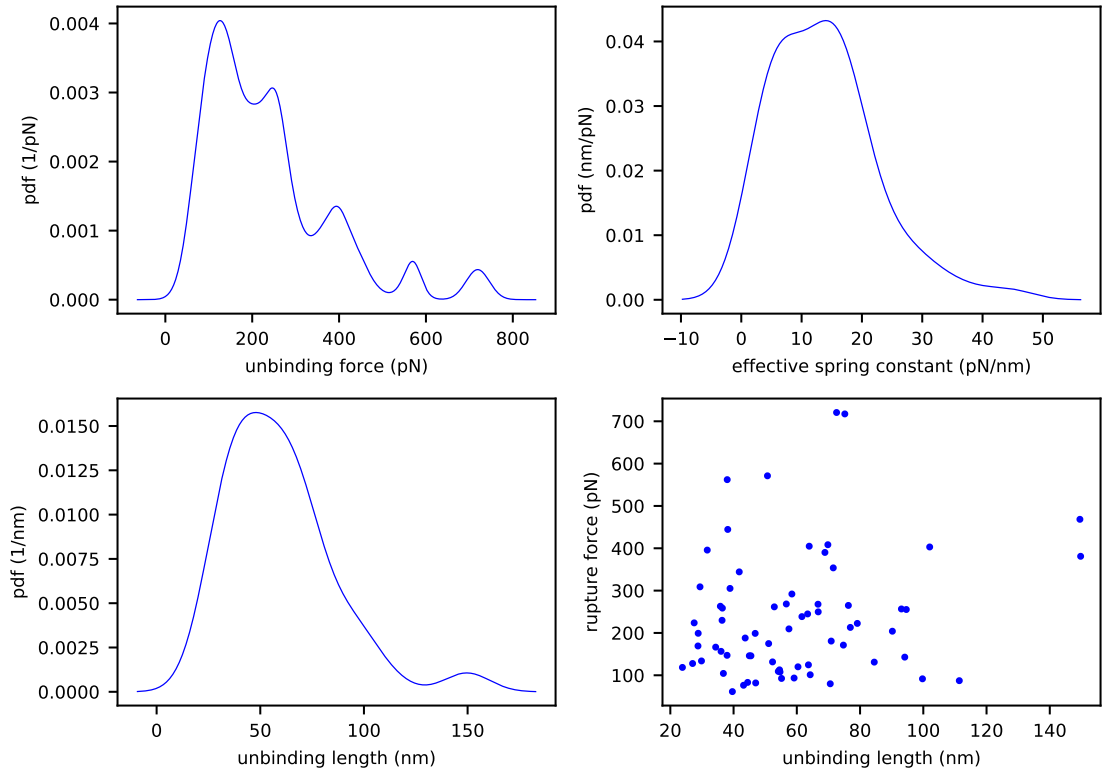


Figure A.7.: Pulling rate  $1 \mu\text{m/s}$ , maximum hold time  $0.3 \text{ s}$ , blocked with  $1.16 \mu\text{g/ml}$  CRP



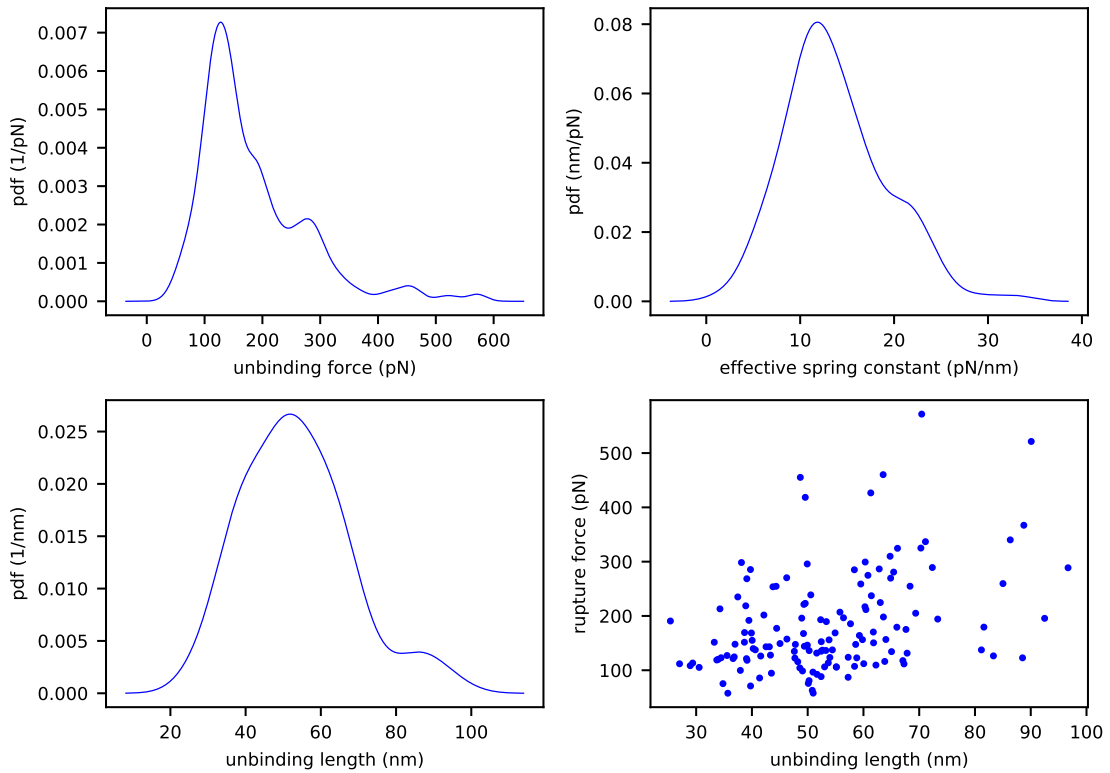


Figure A.9.: Pulling rate  $1.2 \mu\text{m/s}$ , maximum hold time  $0.3 \text{ s}$

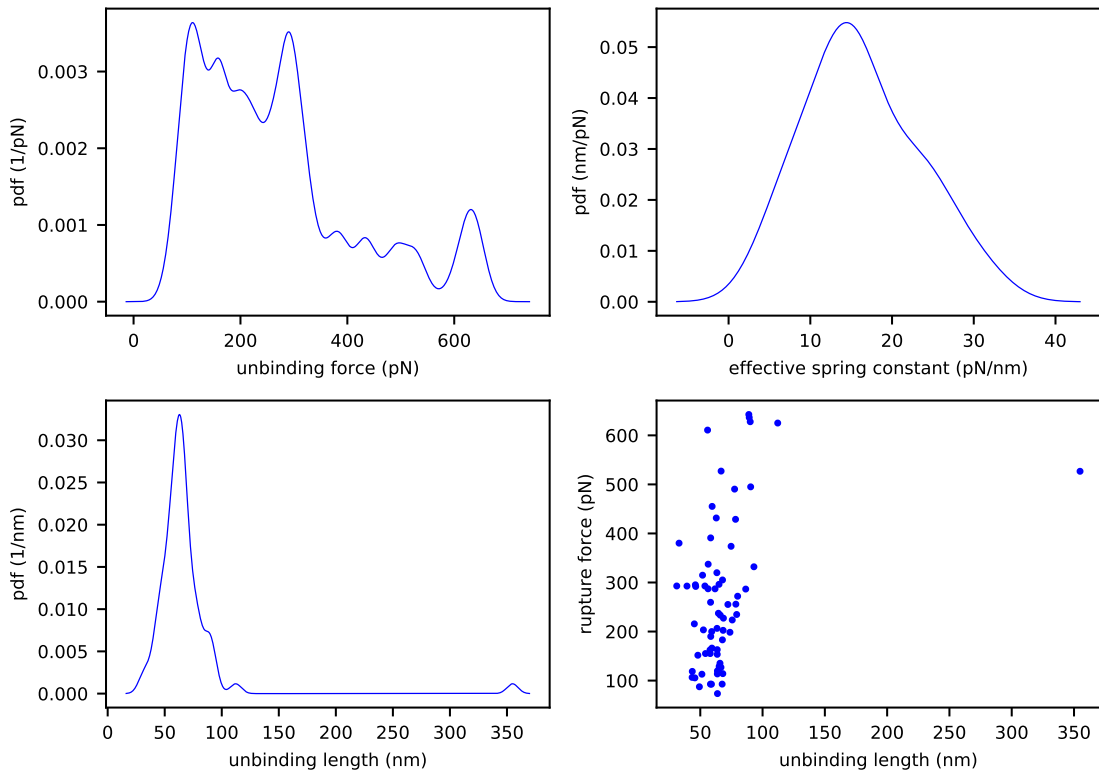


Figure A.10.: Pulling rate  $2.5 \mu\text{m/s}$ , maximum hold time  $0.5 \text{ s}$

## Appendix B.

### Bin-wise rupture force distributions for CRP and anti-CRP

In figures B.1 to B.7, the PDF calculated with formula (1.10) is given in red, the PDF calculated with *ksdensity* is blue.

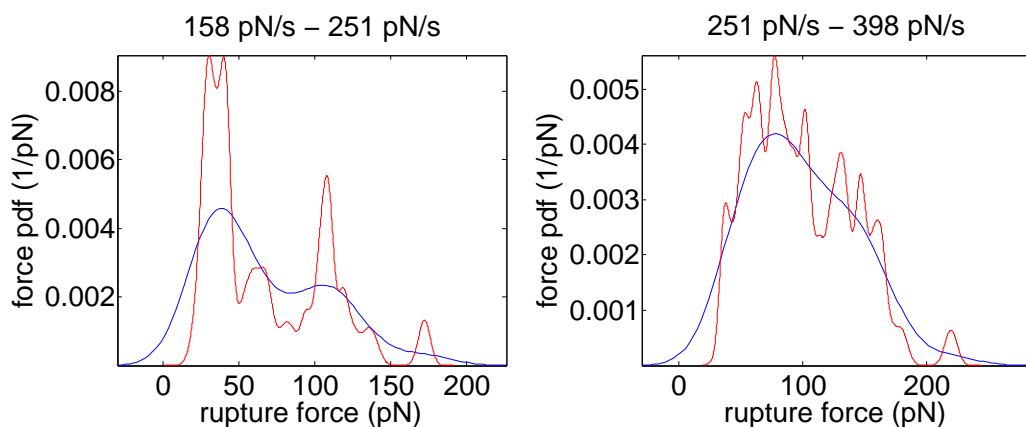


Figure B.1.: Force PDFs for 199.53 pN/s (31 datapoints) and 316.23 pN/s (63 datapoints)

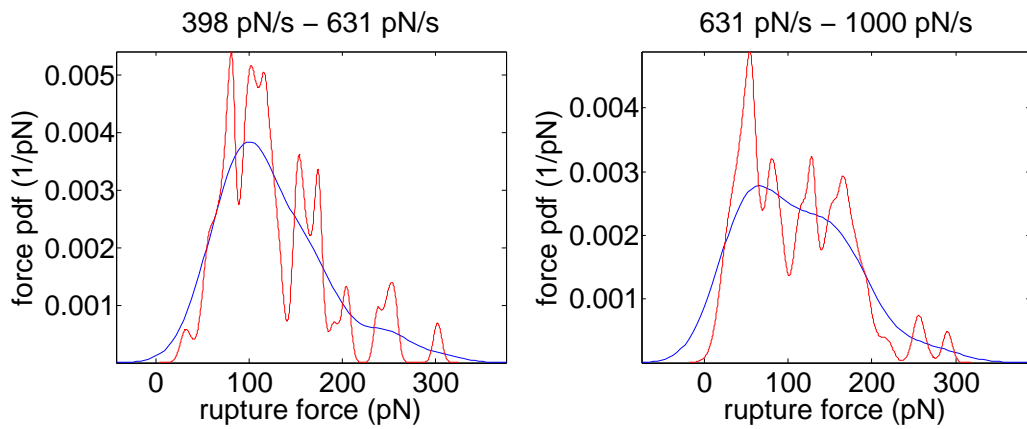


Figure B.2.: Force PDFs for 501.19 pN/s (64 datapoints) and 794.33 pN/s (72 datapoints)

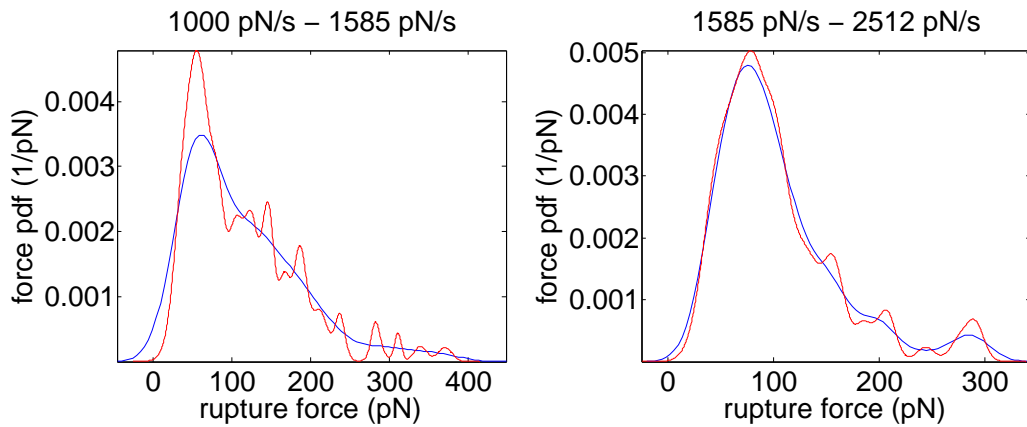


Figure B.3.: Force PDFs for 1258.93 pN/s (103 datapoints) and 1995.26 pN/s (101 datapoints)

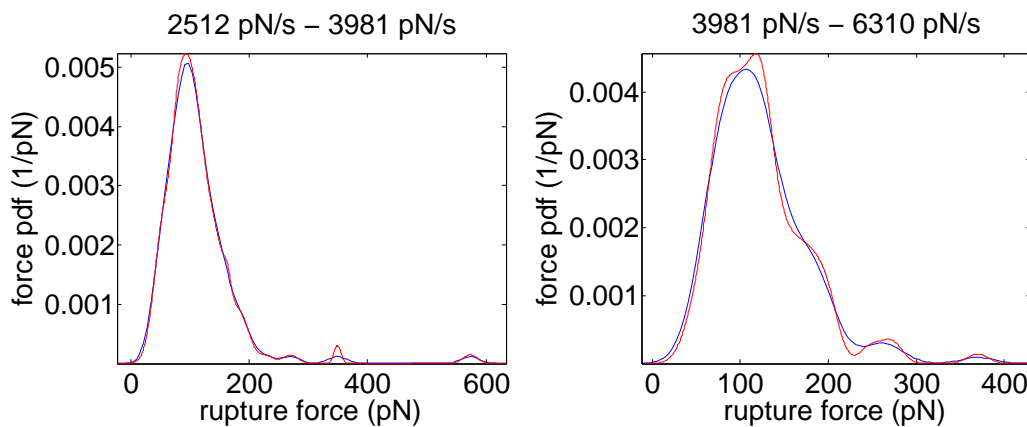


Figure B.4.: Force PDFs for 3162.28 pN/s (112 datapoints) and 5011.87 pN/s (118 datapoints)

Appendix B. Bin-wise rupture force distributions for CRP and anti-CRP

---

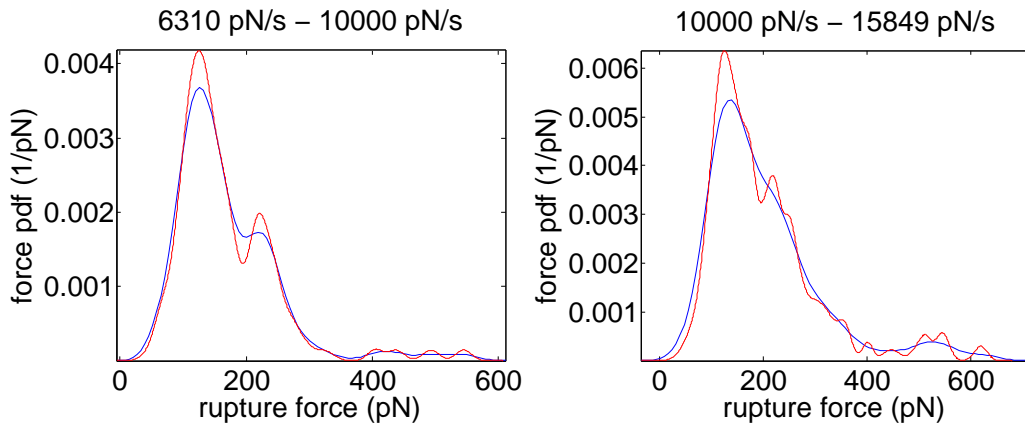


Figure B.5.: Force PDFs for 7943.28 pN/s (111 datapoints) and 12 589.25 pN/s (109 datapoints)

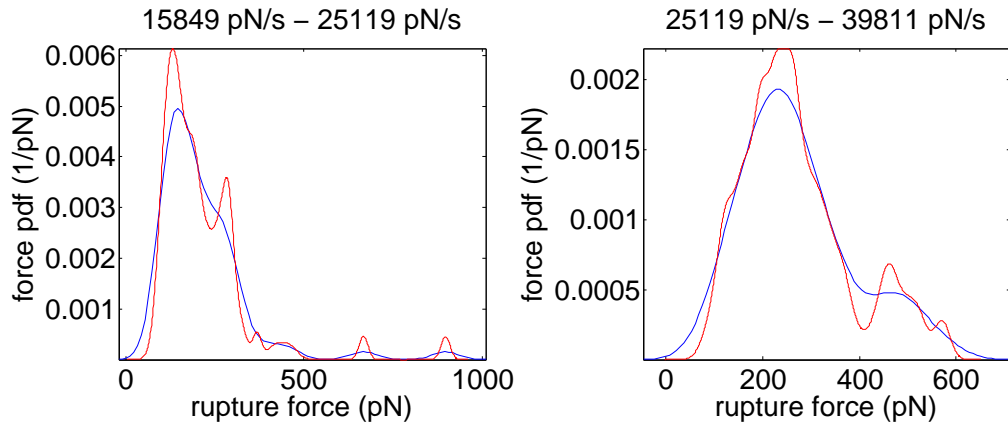


Figure B.6.: Force PDFs for 19 952.62 pN/s (69 datapoints) and 31 622.78 pN/s (47 datapoints)

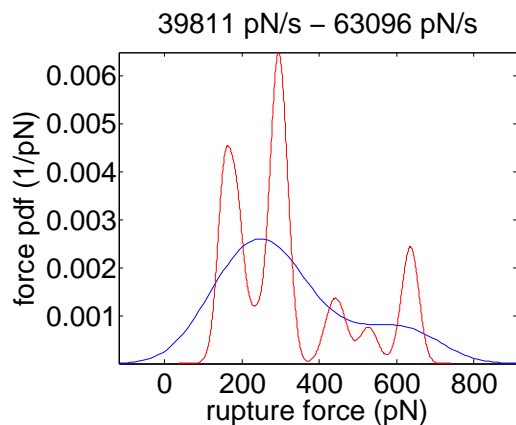


Figure B.7.: Force PDFs for 50 118.72 pN/s (22 datapoints)



## Appendix C.

### Bin-wise rupture force distributions for MSC and anti-RAGE

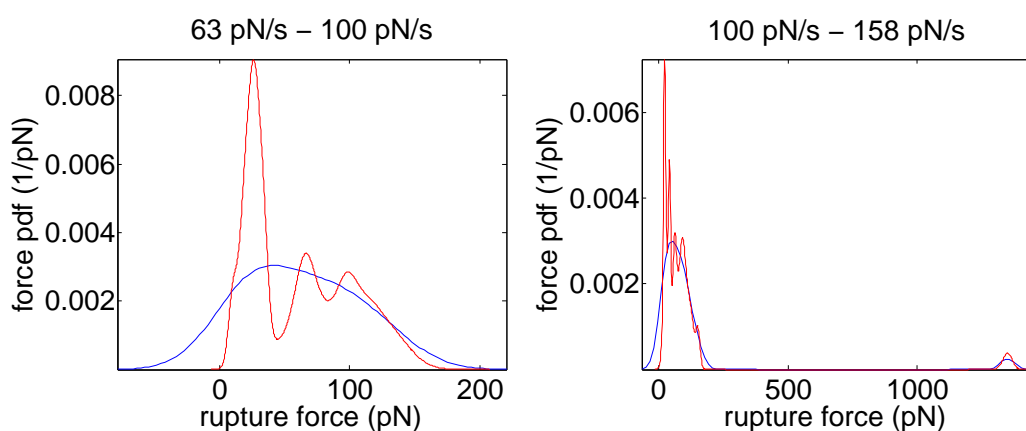


Figure C.1.: Force PDFs for 79.43 pN/s (22 datapoints) and 125.89 pN/s (23 datapoints)

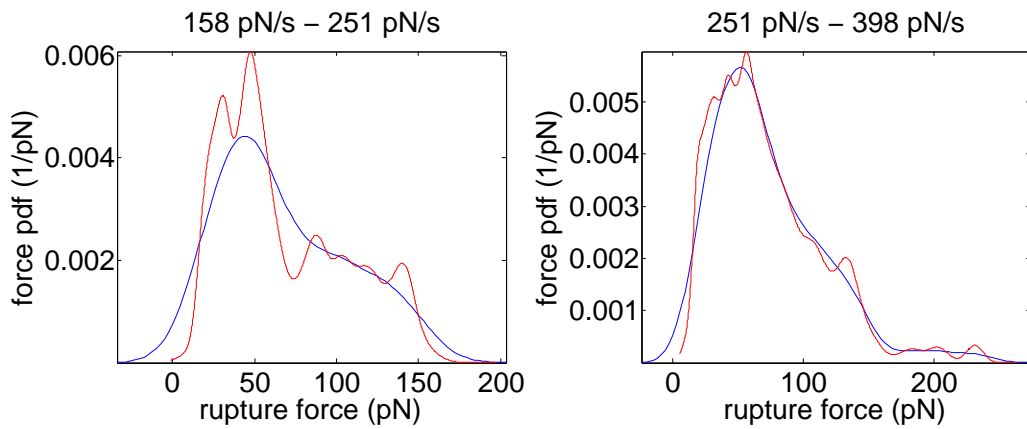


Figure C.2.: Force PDFs for 199.53 pN/s (56 datapoints) and 316.23 pN/s (94 datapoints)

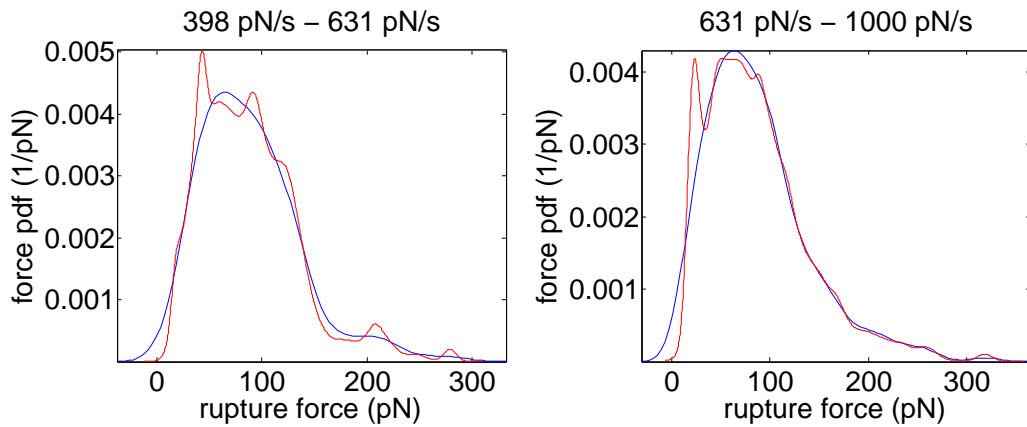


Figure C.3.: Force PDFs for 501.19 pN/s (165 datapoints) and 794.33 pN/s (251 datapoints)

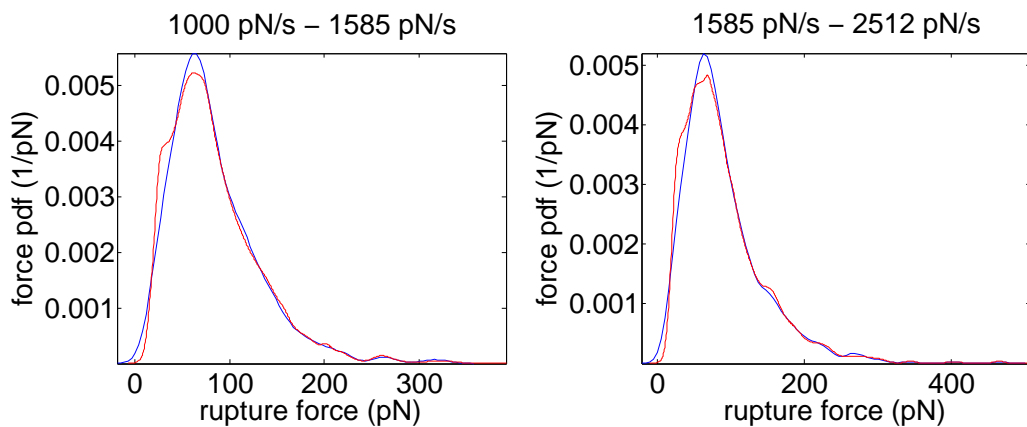


Figure C.4.: Force PDFs for 1258.93 pN/s (419 datapoints) and 1995.26 pN/s (633 datapoints)

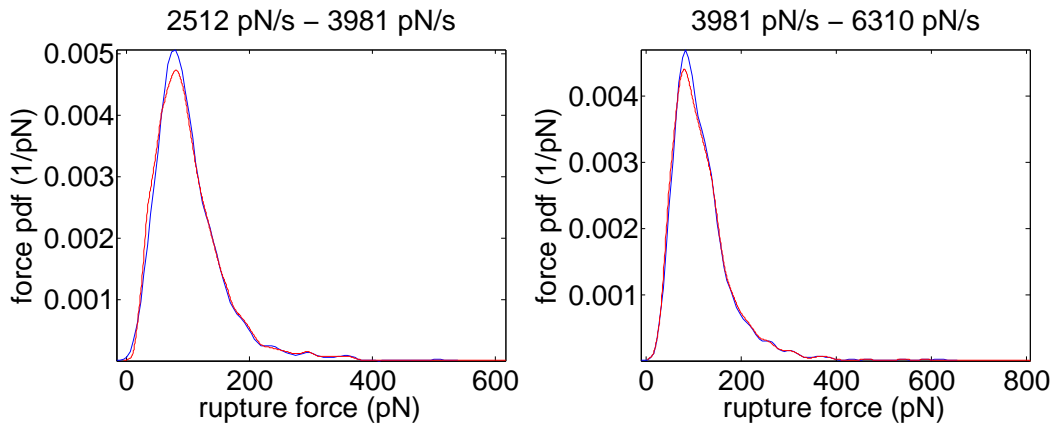


Figure C.5.: Force PDFs for 3162.28 pN/s (767 datapoints) and 5011.87 pN/s (865 datapoints)

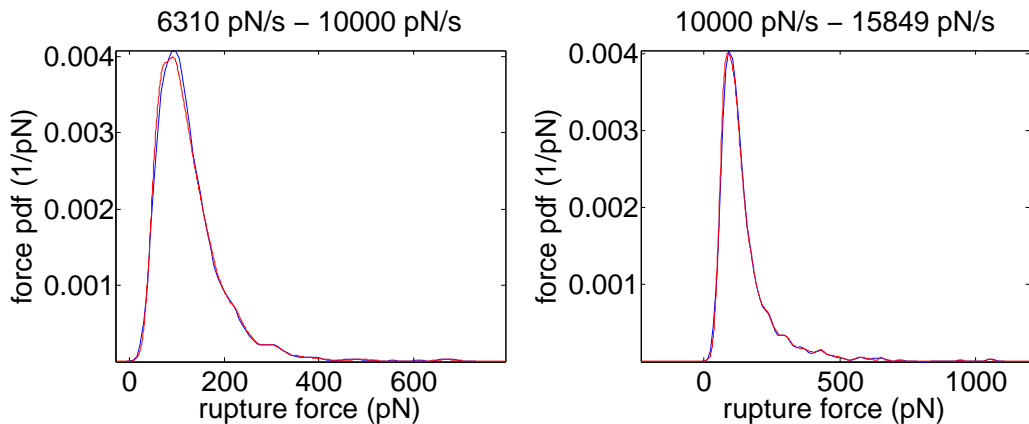


Figure C.6.: Force PDFs for 7943.28 pN/s (939 datapoints) and 12 589.25 pN/s (792 datapoints)

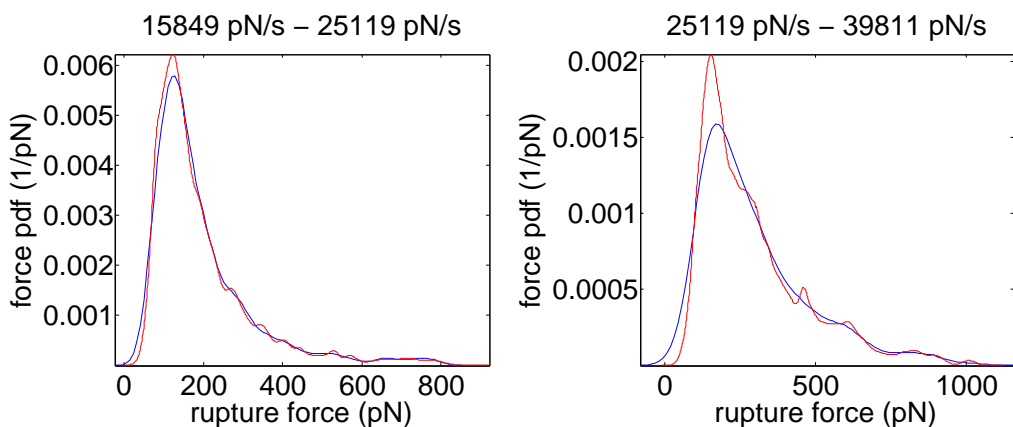


Figure C.7.: Force PDFs for 19 952.62 pN/s (398 datapoints) and 31 622.78 pN/s (279 datapoints)

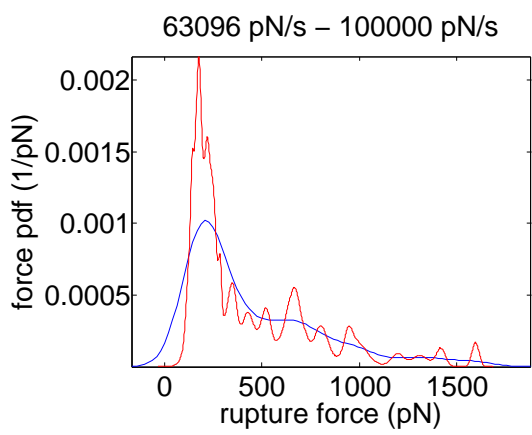


Figure C.8.: Force PDFs for 50 118.72 pN/s (185 datapoints) and 79 432.82 pN/s (65 datapoints)

## Appendix D.

### Gaussian functions fitted onto bin-wise force PDFs for MSC and anti-RAGE

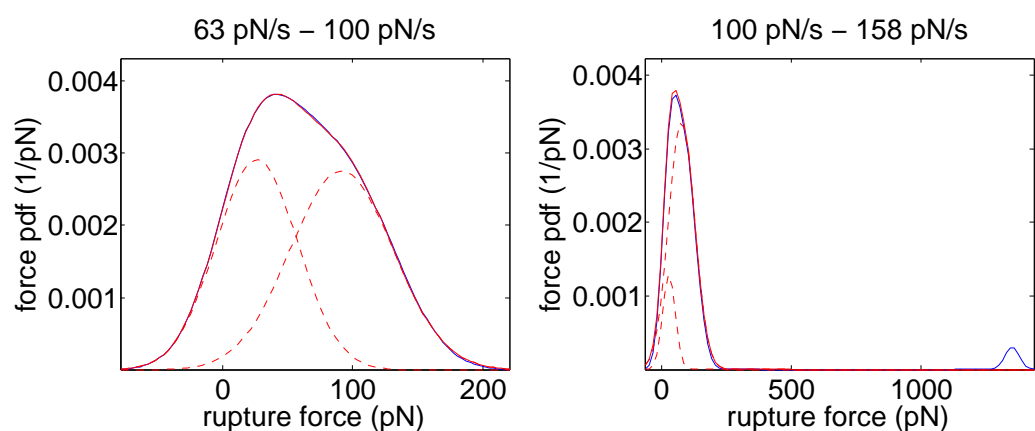


Figure D.1.: Force PDFs and fitted Gaussian functions for 79.43 pN/s (22 datapoints) and 125.89 pN/s (23 datapoints)

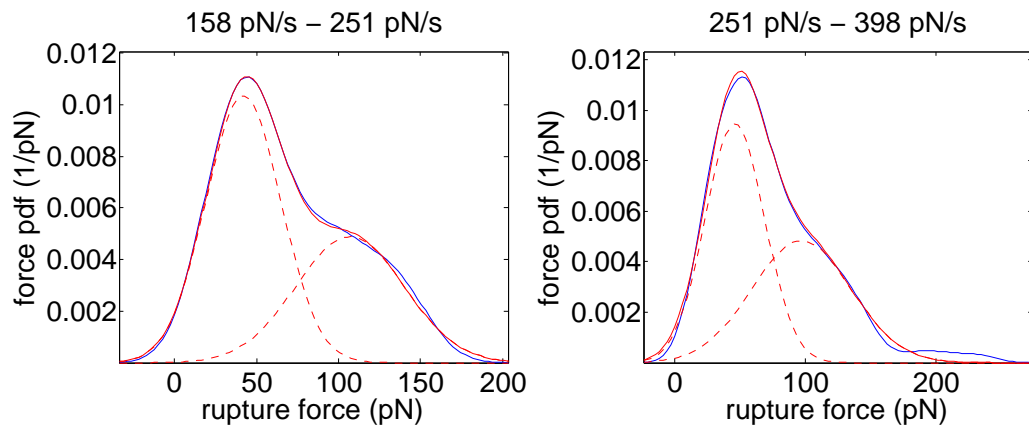


Figure D.2.: Force PDFs and fitted Gaussian functions for 199.53 pN/s (56 datapoints) and 316.23 pN/s (94 datapoints)

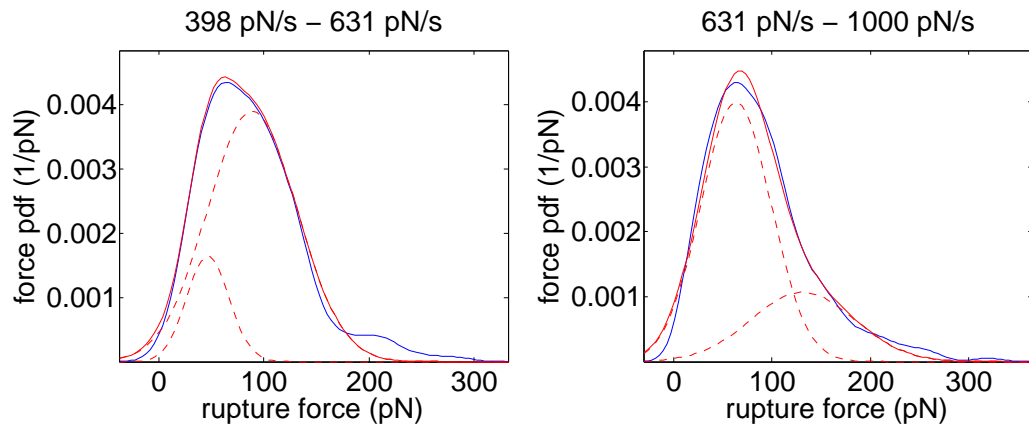


Figure D.3.: Force PDFs and fitted Gaussian functions for 501.19 pN/s (165 datapoints) and 794.33 pN/s (251 datapoints)

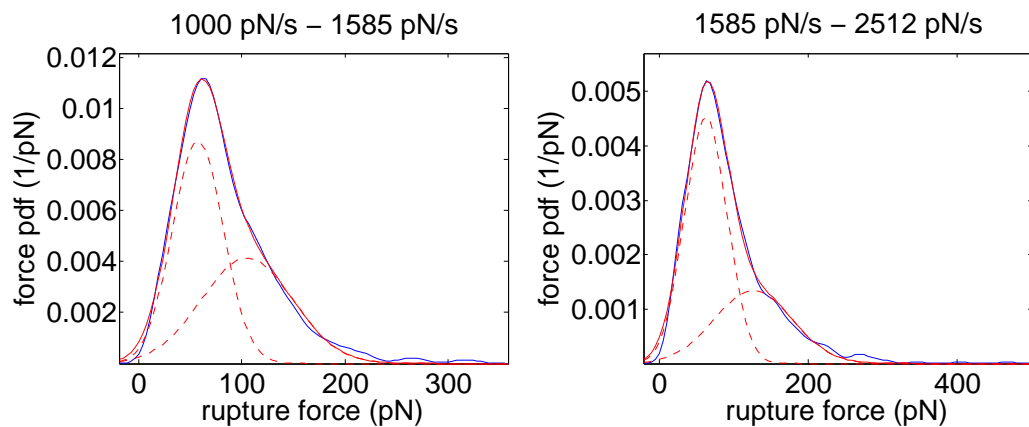


Figure D.4.: Force PDFs and fitted Gaussian functions for 1258.93 pN/s (419 datapoints) and 1995.26 pN/s (633 datapoints)

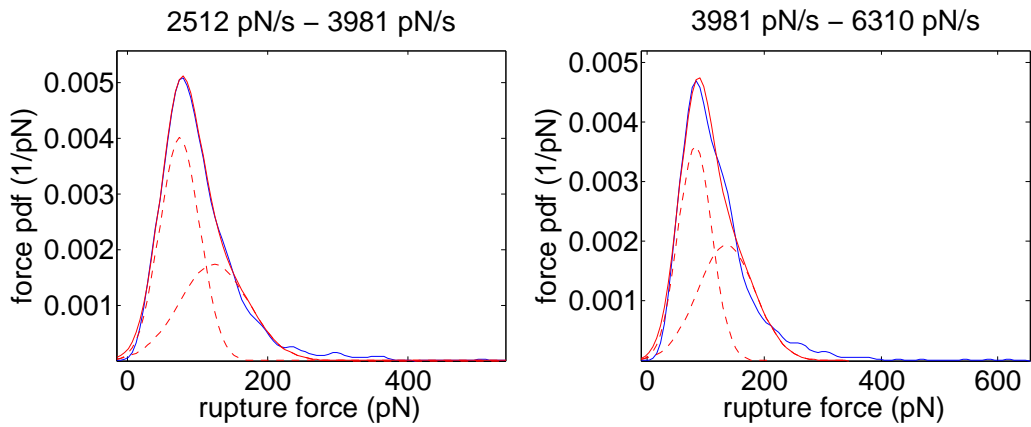


Figure D.5.: Force PDFs and fitted Gaussian functions for 3162.28 pN/s (767 datapoints) and 5011.87 pN/s (865 datapoints)

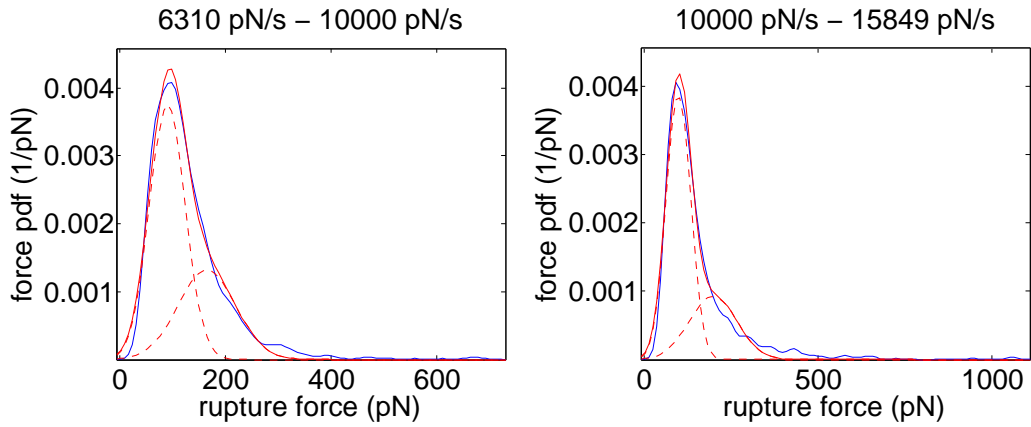


Figure D.6.: Force PDFs and fitted Gaussian functions for 7943.28 pN/s (939 datapoints) and 12 589.25 pN/s (792 datapoints)

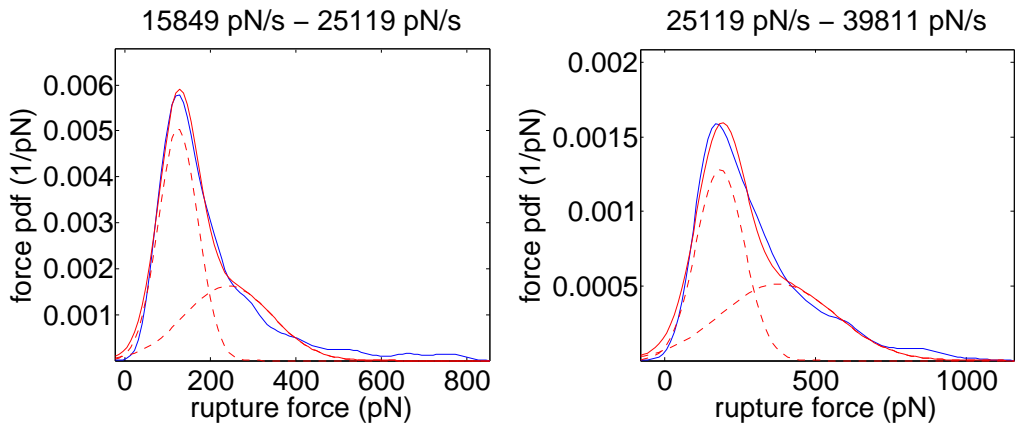


Figure D.7.: Force PDFs and fitted Gaussian functions for 19 952.62 pN/s (398 datapoints) and 31 622.78 pN/s (279 datapoints)

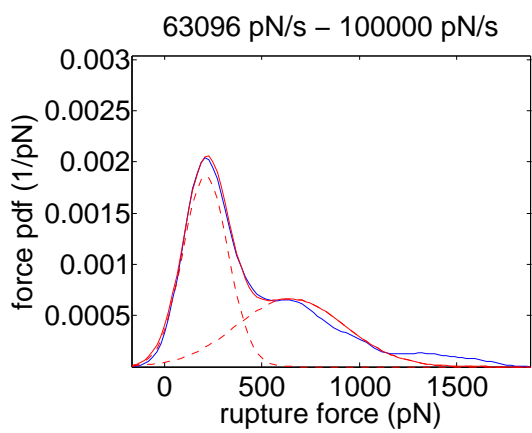


Figure D.8.: Force PDFs and fitted Gaussian functions for 50 118.72 pN/s (185 datapoints) and 79 432.82 pN/s (65 datapoints)

# Bibliography

- [1] G. Binnig, C. F. Quate, and Ch. Gerber. "Atomic Force Microscope." In: *Physical Review Letters* 56.9 (Mar. 3, 1986), pp. 930–933. ISSN: 0031-9007. DOI: 10.1103/PhysRevLett.56.930. URL: <https://link.aps.org/doi/10.1103/PhysRevLett.56.930> (visited on 06/11/2019) (cit. on pp. 2, 4).
- [2] Bharat Bhushan. *Springer handbook of nanotechnology*. 4th edition. Springer handbooks 15558. New York, NY: Springer Berlin Heidelberg, 2017. ISBN: 978-3-662-54355-9 (cit. on pp. 2–5, 8, 10, 13, 14, 16).
- [3] Peter Hinterdorfer and Antoine Van Oijen, eds. *Handbook of single-molecule biophysics*. OCLC: ocn496226600. Dordrecht ; New York: Springer, 2009. 626 pp. ISBN: 978-0-387-76496-2 978-0-387-76497-9 (cit. on pp. 3, 5, 8, 10, 12, 14, 15, 17).
- [4] Bert Voigtländer, ed. *Scanning probe microscopy*. New York, NY: Springer Berlin Heidelberg, 2015. ISBN: 978-3-662-45239-4 (cit. on pp. 4, 5, 12).
- [5] Andreas Ebner et al. "A New, Simple Method for Linking of Antibodies to Atomic Force Microscopy Tips." In: *Bioconjugate Chemistry* 18.4 (July 2007), pp. 1176–1184. ISSN: 1043-1802, 1520-4812. DOI: 10.1021/bc070030s. URL: <https://pubs.acs.org/doi/10.1021/bc070030s> (visited on 04/21/2019) (cit. on pp. 6, 7, 27).
- [6] Linda Wildling et al. "Linking of Sensor Molecules with Amino Groups to Amino-Functionalized AFM Tips." In: *Bioconjugate Chemistry* 22.6 (June 15, 2011), pp. 1239–1248. ISSN: 1043-1802, 1520-4812. DOI: 10.1021/bc200099t. URL: <https://pubs.acs.org/doi/10.1021/bc200099t> (visited on 04/21/2019) (cit. on pp. 6, 7, 26, 27).
- [7] Andreas Ebner, Peter Hinterdorfer, and Hermann J. Gruber. "Comparison of different amino-functionalization strategies for attachment of single antibodies to AFM cantilevers." In: *Ultramicroscopy* 107.10 (Oct. 2007), pp. 922–927. ISSN: 03043991. DOI: 10.1016/j.ultramic.2007.02.035. URL: <https://linkinghub.elsevier.com/retrieve/pii/S0304399107001040> (visited on 04/21/2019) (cit. on pp. 6, 7, 25).

- [8] Christian K. Riener et al. "Simple test system for single molecule recognition force microscopy." In: *Analytica Chimica Acta* 479.1 (Mar. 2003), pp. 59–75. ISSN: 00032670. DOI: 10.1016/S0003-2670(02)01373-9. URL: <https://linkinghub.elsevier.com/retrieve/pii/S0003267002013739> (visited on 04/21/2019) (cit. on pp. 6, 25).
- [9] C. Bouchiat et al. "Estimating the Persistence Length of a Worm-Like Chain Molecule from Force-Extension Measurements." In: *Biophysical Journal* 76.1 (Jan. 1999), pp. 409–413. ISSN: 00063495. DOI: 10.1016/S0006-3495(99)77207-3. URL: <https://linkinghub.elsevier.com/retrieve/pii/S0006349599772073> (visited on 06/27/2019) (cit. on p. 9).
- [10] W. Baumgartner, P. Hinterdorfer, and H. Schindler. "Data analysis of interaction forces measured with the atomic force microscope." In: *Ultramicroscopy* 82.1 (Feb. 2000), pp. 85–95. ISSN: 03043991. DOI: 10.1016/S0304-3991(99)00154-0. URL: <https://linkinghub.elsevier.com/retrieve/pii/S0304399199001540> (visited on 06/24/2019) (cit. on pp. 9, 10, 50).
- [11] Ferry Kienberger et al. "Molecular Recognition Imaging and Force Spectroscopy of Single Biomolecules." In: *Accounts of Chemical Research* 39.1 (Jan. 2006), pp. 29–36. ISSN: 0001-4842, 1520-4898. DOI: 10.1021/ar050084m. URL: <https://pubs.acs.org/doi/10.1021/ar050084m> (visited on 06/24/2019) (cit. on p. 13).
- [12] E. Evans and K. Ritchie. "Dynamic strength of molecular adhesion bonds." In: *Biophysical Journal* 72.4 (Apr. 1997), pp. 1541–1555. ISSN: 00063495. DOI: 10.1016/S0006-3495(97)78802-7. URL: <https://linkinghub.elsevier.com/retrieve/pii/S0006349597788027> (visited on 07/10/2019) (cit. on p. 14).
- [13] G. Bell. "Models for the specific adhesion of cells to cells." In: *Science* 200.4342 (May 12, 1978), pp. 618–627. ISSN: 0036-8075, 1095-9203. DOI: 10.1126/science.347575. URL: <http://www.sciencemag.org/cgi/doi/10.1126/science.347575> (visited on 07/10/2019) (cit. on p. 14).
- [14] Gerhard Hummer and Attila Szabo. "Kinetics from Nonequilibrium Single-Molecule Pulling Experiments." In: *Biophysical Journal* 85.1 (July 2003), pp. 5–15. ISSN: 00063495. DOI: 10.1016/S0006-3495(03)74449-X. URL: <https://linkinghub.elsevier.com/retrieve/pii/S000634950374449X> (visited on 07/16/2019) (cit. on p. 16).
- [15] Olga K Dudko, Gerhard Hummer, and Attila Szabo. "Intrinsic Rates and Activation Free Energies from Single-Molecule Pulling Experiments." In: *PHYSICAL REVIEW LETTERS* (2006), p. 4 (cit. on pp. 16, 17).

## Bibliography

---

- [16] R. W. Friddle, A. Noy, and J. J. De Yoreo. "Interpreting the widespread nonlinear force spectra of intermolecular bonds." In: *Proceedings of the National Academy of Sciences* 109.34 (Aug. 21, 2012), pp. 13573–13578. ISSN: 0027-8424, 1091-6490. DOI: 10.1073/pnas.1202946109. URL: <http://www.pnas.org/cgi/doi/10.1073/pnas.1202946109> (visited on 07/16/2019) (cit. on pp. 17–20).
- [17] Raymond W. Friddle et al. "Near-Equilibrium Chemical Force Microscopy." In: *The Journal of Physical Chemistry C* 112.13 (Apr. 2008), pp. 4986–4990. ISSN: 1932-7447, 1932-7455. DOI: 10.1021/jp7095967. URL: <https://pubs.acs.org/doi/10.1021/jp7095967> (visited on 08/06/2019) (cit. on p. 19).
- [18] Ashok Garai, Yaojun Zhang, and Olga K. Dudko. "Conformational dynamics through an intermediate." In: *The Journal of Chemical Physics* 140.13 (Apr. 7, 2014), p. 135101. ISSN: 0021-9606, 1089-7690. DOI: 10.1063/1.4869869. URL: <http://aip.scitation.org/doi/10.1063/1.4869869> (visited on 08/06/2019) (cit. on p. 20).
- [19] Olga K. Dudko. "Decoding the mechanical fingerprints of biomolecules." In: *Quarterly Reviews of Biophysics* 49 (2016), e3. ISSN: 0033-5835, 1469-8994. DOI: 10.1017/S0033583515000220. URL: [https://www.cambridge.org/core/product/identifier/S0033583515000220/type/journal\\_article](https://www.cambridge.org/core/product/identifier/S0033583515000220/type/journal_article) (visited on 08/06/2019) (cit. on p. 20).
- [20] Félix Rico and Vincent T. Moy. "Energy landscape roughness of the streptavidin–biotin interaction." In: *Journal of Molecular Recognition* 20.6 (Nov. 2007), pp. 495–501. ISSN: 09523499, 10991352. DOI: 10.1002/jmr.841. URL: <http://doi.wiley.com/10.1002/jmr.841> (visited on 07/24/2019) (cit. on pp. 21, 33).
- [21] F. T. Hane, S. J. Attwood, and Z. Leonenko. "Comparison of three competing dynamic force spectroscopy models to study binding forces of amyloid-beta (1–42)." In: *Soft Matter* 10.12 (2014), p. 1924. ISSN: 1744-683X, 1744-6848. DOI: 10.1039/c3sm52257a. URL: <http://xlink.rsc.org/?DOI=c3sm52257a> (visited on 07/24/2019) (cit. on pp. 21, 33).
- [22] Filomena A. Carvalho et al. "Atomic Force Microscopy-Based Molecular Recognition of a Fibrinogen Receptor on Human Erythrocytes." In: *ACS Nano* 4.8 (Aug. 24, 2010), pp. 4609–4620. ISSN: 1936-0851, 1936-086X. DOI: 10.1021/nn1009648. URL: <http://pubs.acs.org/doi/10.1021/nn1009648> (visited on 07/24/2019) (cit. on pp. 21, 33).
- [23] Mark B Pepys and Gideon M Hirschfield. "C-reactive protein: a critical update." In: *The Journal of Clinical Investigation* 111.12 (2003), p. 9 (cit. on pp. 21, 22).

- [24] Steven Black, Irving Kushner, and David Samols. "C-reactive Protein." In: *Journal of Biological Chemistry* 279.47 (Nov. 19, 2004), pp. 48487–48490. ISSN: 0021-9258, 1083-351X. DOI: 10.1074/jbc.R400025200. URL: <http://www.jbc.org/lookup/doi/10.1074/jbc.R400025200> (visited on 04/15/2019) (cit. on pp. 21–23).
- [25] Gregory Yourek, Mohammad A. Hussain, and Jeremy J. Mao. "Cytoskeletal Changes of Mesenchymal Stem Cells During Differentiation:" in: *ASAIO Journal* 53.2 (Mar. 2007), pp. 219–228. ISSN: 1058-2916. DOI: 10.1097/MAT.0b013e31802deb2d. URL: <https://insights.ovid.com/crossref?an=00002480-200703000-00018> (visited on 08/06/2019) (cit. on p. 23).
- [26] Shinichiro Kume et al. "Advanced Glycation End-Products Attenuate Human Mesenchymal Stem Cells and Prevent Cognate Differentiation Into Adipose Tissue, Cartilage, and Bone." In: *Journal of Bone and Mineral Research* 20.9 (May 23, 2005), pp. 1647–1658. ISSN: 08840431. DOI: 10.1359/JBMR.050514. URL: <http://doi.wiley.com/10.1359/JBMR.050514> (visited on 08/06/2019) (cit. on p. 23).
- [27] *Human CRP protein — Biorbyt*. URL: <https://www.biorbyt.com/human-crp-protein-orb391529.html> (visited on 07/16/2019) (cit. on p. 25).
- [28] *Phosphate-buffered saline (PBS)*. URL: <http://cshprotocols.cshlp.org/content/2006/1/pdb-rec8247> (visited on 08/14/2019) (cit. on p. 25).
- [29] David Nečas and Petr Klapetek. "Gwyddion: an open-source software for SPM data analysis." In: *Open Physics* 10.1 (Jan. 1, 2012). ISSN: 2391-5471. DOI: 10.2478/s11534-011-0096-2. URL: <http://www.degruyter.com/view/j/phys.2012.10.issue-1/s11534-011-0096-2/s11534-011-0096-2.xml> (visited on 06/24/2019) (cit. on p. 30).
- [30] Christian Rankl et al. "Accuracy Estimation in Force Spectroscopy Experiments." In: *Japanese Journal of Applied Physics* 46.8 (Aug. 23, 2007), pp. 5536–5539. ISSN: 0021-4922, 1347-4065. DOI: 10.1143/JJAP.46.5536. URL: <http://stacks.iop.org/1347-4065/46/5536> (visited on 08/19/2019) (cit. on p. 33).
- [31] *Least-Squares Fitting - MATLAB & Simulink - MathWorks Deutschland*. URL: <https://de.mathworks.com/help/curvefit/least-squares-fitting.html> (visited on 07/24/2019) (cit. on p. 37).
- [32] M Ledvij. "Curve fitting made easy." In: *Industrial Physicist* 9 (2003), pp. 24–27 (cit. on p. 37).
- [33] *Evaluating Goodness of Fit - MATLAB & Simulink*. URL: <https://www.mathworks.com/help/curvefit/evaluating-goodness-of-fit.html> (visited on 07/24/2019) (cit. on p. 37).
- [34] *Akaike or Bayesian information criteria - MATLAB aicbic*. URL: <https://www.mathworks.com/help/econ/aicbic.html> (visited on 08/05/2019) (cit. on p. 49).